Titre: Title:	Circulating fluidized beds : hydrodynamics and reactor modelling
Auteur: Author:	Gregory Scott Patience
Date:	1990
Type:	Mémoire ou thèse / Dissertation or Thesis
Référence: Citation:	Patience, G. S. (1990). Circulating fluidized beds : hydrodynamics and reactor modelling [Ph.D. thesis, École Polytechnique de Montréal]. PolyPublie. https://publications.polymtl.ca/36796/

URL de PolyPublie: PolyPublie URL:	https://publications.polymtl.ca/36796/
Directeurs de recherche: Advisors:	Jamal Chaouki
Programme: Program:	Unspecified

UNIVERSITE DE MONTREAL

CIRCULATING FLUIDIZED BEDS:
HYDRODYNAMICS AND REACTOR MODELLING

par

Gregory S. Patience
DEPARTMENT DE GENIE CHIMIQUE
ECOLE POLYTECHNIQUE

THESE PRESENTEE EN VUE DE L'OBTENTION DU
GRADE DE PHILOSOPHIAE DOCTOR (Ph.D.)
(GENIE CHIMIQUE)

septembre, 1990

National Library
of Canada

Bibliothèque nationale
du Canada

Canadian Theses Service

Service des thèses canadiennes

Ottawa, Canada
K1A 0N4

ISBN 0-315-64327-7

UNIVERSITE DE MONTREAL

ECOLE POLYTECHNIQUE

Cette thèse intitulée:

CIRCULATING FLUIDIZED BEDS:
HYDRODYNAMICS AND REACTOR MODELLING

présentée par: Gregory S. Patience

en vue de l'obtention du grade de: Ph.D.

a été dûment acceptée par le jury d'examen constitué de:

M. C. Chavarie, Ph.D., président

M. J. Chaouki, Ph.D.

M. J. R. Grace, Ph. D.

M. R. M. Contractor, Ph.D.

I dedicate this thesis to Nadine

ABSTRACT

The rediscovered technology of circulating particles at high superficial gas velocities has been given significant attention in the scientific literature recently. Despite this resurgence of academic popularity, an understanding of the riser hydrodynamics and general operation of circulating fluidized beds (CFB) is lacking. In this work, radioactive tracers are used to examine both the gas and solids comportments in the fast fluidization regime of a riser 5 m tall and 82.8 mm in diameter as well as the packed bed regime of a 3 m standpipe.

A core-annular model for both the gas phase and solids is used to characterize the hydrodynamics of the riser. The slip velocity in the core is equal to the single particle terminal velocity. Along the wall, the particles descend at velocities around 0.8 m/s. The core-annular mass transfer coefficient, k, is higher for the gas than for the solids. The core radius decreases with height as does k. At the base of the riser, k is typically three times the value in the lean phase. There is little gas dispersion. Solids dispersion is greatest in the dense phase and decreases with height. Typical values of the dispersion coefficient range between 0.1-0.5 m^2/s. The coefficient of dispersion increases with particle size.

The solids in the standpipe descend in plug flow. The gas in the standpipe flows either counter-current or co-current to the solids depending on the conditions in the riser. Particle wall velocity measurements made in a pyrex tube were approximately 50% of the solids bulk velocity.

Solids circulation rates were determined using a simple technique involving the measurement of the pressure drop between the cyclone and riser. The pressure drop in the acceleration region of this horizontal pipe was found to be sensitive to both the mass flux and gas velocity.

A computational study is detailed concerning the partial oxidation of butane to maleic anhydride. Predictions of a number of different hydrodynamic models are compared. Results from the simulation indicate the effect of the core radius is significant in terms of total butane conversion as is the assumed cross-flow coefficient between the core and annular zone.

SOMMAIRE

La redécouverte de la fluidisation rapide a donné un nouvel élan à la recherche scientifique actuelle dans le domaine de la fluidisation. Cependant, malgré tout ce renouveau, les connaissances relatives à l’hydrodynamique de cette technique ainsi que la conduite des opérations dans ces lits sont éparses et mêmes contradictoires. Le lit fluidisé circulant utilisé dans ce projet est en acier inoxydable de 5 m de haut et de 82.8 mm de diamètre. Le tuyau de retour a une forme en "L" et il est de 3 m de haut et de 82.8 mm de diamètre. Dans ce travail, des traceurs radioactifs sont utilisés pour examiner le comportement du gaz et du solide en régime de fluidisation rapide aussi bien dans le lit de 5 m de haut que dans le tuyau de retour. L’argon et des particules de sable sont utilisés comme traceurs radioactifs. Ils ont été irradiés dans le réacteur SLOWPOKE de l’Ecole Polytechnique de Montréal.

Dans ce travail, il est démontré qu’un modèle de dispersion axial est inadéquat pour caractériser l’hydrodynamique des Lits Fluidisés Circulants (LFC). Cependant, un modèle noyau-anneau pour le gaz et le solide est satisfaisant pour caractériser l’hydrodynamique de ces lits. A partir de ce modèle, les différents paramètres caractérisant l’écoulement du gaz et du solide ont été ajustés sur les données expérimentales. Ainsi, la vitesse de glissement dans le noyau est

égale à la vitesse terminale de la particule initiale. Le long de la paroi, les particules descendent à des vitesses voisines de 0.8 m/s. Le coefficient de transfert de matière, k, entre le noyau et l'anneau est plus élevé pour le gaz que pour le solide. A la base du lit, la valeur de k est typiquement trois fois celle obtenue en haut du lit. Il y a peu de dispersion du gaz. Par contre, la dispersion du solide est significative: elle est plus grande dans la phase dense et décroît avec la hauteur. Les valeurs typiques de ce coefficient de dispersion se situent entre 0.1 et 0.5 m^2/s. La valeur de celui-ci croît avec le diamètre des particules.

Les données expérimentales relatives à l'écoulement du gaz et du solide dans le tuyau de retour ont été obtenues par la méthode des Distributions de Temps de Séjour (DTS). Ainsi, le solide dans la ligne de retour descend en écoulement piston, alors que le gaz circule soit à contre-courant soit à co-courant du solide dépendemment des conditions utilisées dans le LFC. Les vitesses des particules à la paroi sont approximativement 50% plus faibles que celles des particules au centre du tube. L'équation modifiée de Ergun, écrite en termes de vitesse de glissement, peut être avantageusement employée pour prédir les pertes de charge dans le tuyau de retour:

$$-\frac{dP}{dz} = K_1 V_{s\ell} + K_2 V_{s\ell} |V_{s\ell}|$$

où,

$$K_1 = \frac{150\mu(1-\epsilon)^2}{(\psi_s d_p \epsilon)^2}$$

$$K_2 = \frac{1.75\rho(1-\epsilon)}{(\psi_s d_p \epsilon)}$$

$V_{sl} = V_s - V_g$ = vitesse de glissement

Le taux de recirculation du solide est déterminé par une technique simple qui consiste à mesurer la perte de charge du gaz entre la sortie du LFC et le cyclone. Dans cette zone d'accélération, la perte de charge est très sensible aussi bien au flux massique qu'à la vitesse du gaz. La relation établie est:

$$\Delta P = aG_{sh}L + 2\rho(L/D)bG_{sh}V_{gh}^2 + 2\rho f_g(L/D)V_{gh}^2$$

Les différents termes de cette équation peuvent être interprétés comme suit:

premier terme = accélération du solide

deuxième terme = friction du solide et du gaz

troisième terme = accélération du gaz

Une simulation concernant l'oxydation partielle du butane en anhydride maléique dans un LFC est présentée. Les équations obtenues par un bilan de masse sont:

NOYAU:

$$\frac{\partial}{\partial x}(V_g C_{i,c}) + \rho_p(1-\epsilon_c)\varphi\Sigma r_i + \frac{2k}{r_c}(C_{i,c}-C_{i,a}) = 0$$

ANNEAU:

$$\rho_p(1-\epsilon_a)(1-\varphi)\Sigma r_i - 2kr_c/(R^2-r_c{}^2)\ (C_{i,c}-C_{i,a}) = 0$$

Les prédictions obtenues à partir de différents modèles hydrodynamiques sont comparés. Celles-ci indiquent que les effets de la taille du noyau ainsi que la valeur du coefficient de transfert entre le noyau et l'anneau sont significatifs, mais que les effets du taux de recirculation du solide le sont encore plus.

ACKNOWLEDGEMENTS

First of all, I wish to thank Dr. Jamal Chaouki for his guidance, encouragement and friendship throughout this study. His suggestions and availability was very much appreciated.

My wife, Nadine, assisted in preparing the gaphs as well as typing. Her "patience" and support helped sustain my energy.

Without the resources of the Department de Genie Energetique the tracer experiments would have been difficult if not impossible to conduct. I am grateful to Dr. G. Kennedy for the many days he spent with me to perfect the method, calibrate the detectors, orient the lead brick housing etc. J. St-Pierre injected countless argon and sand samples into the SLOWPOKE reactor on my behalf.

Amar "Boogieman" Fetoui taught me French, so if I have an English-North African accent it is thanks to him. I would also like to acknowledge the friendship of Ihab Wassef, Marika Mouscardy, as well as the undergraduate and graduate students in Chemical Engineering at l'Ecole Polytechnique.

I am indebted to the technical expertise of Gerald Lafortune and Robert Delisle who helped develop the experimental apparatus simply and economically.

Finally, I would like to acknowledge the time and efforts of the examination committee, Drs. J.R. Grace, R. M. Contractor, and C. Chavarie, who agreed to appraise this work in such short notice despite other pressing demands on their time. In particular, I thank Dr. Chavarie whose enthusiasm and charisma attracted me to the Department of Génie Chimique at the Ecole Polytechnique.

This work was supported through generous scholarships from NSERC, FCAR and the Bourse d'Excellence de l'Ecole Polytechnique.

TABLE OF CONTENTS

LIST OF TABLES

LIST OF FIGURES

NOMENCLATURE

A	frequency factor in Arrhenius equation
A_p	projected particle surface area, m^2
Ar	Archimedes' Number, $d_p^3 \rho_f (\rho_p - \rho_f) g/\mu^2$
A_s	total surface area, m^2
a	fitted parameter in Equation 4.8 and 4.26
a_m	effective external surface area per unit mass, m^2/kg
a_r	total external surface area per unit mass, m^2/kg
b	fitted parameter in Equation 4.9
C	concentration, mol/ℓ
C_d	drag coefficient
C_o	inlet pulse concentration, mol/ℓ
C_p	heat capacity, kJ/kg-K
C_v	number of active vacant sites on the catalyst surface
C^T	Laplace transform of concentration
C_t	total number of active sites on catalyst
c	coefficient defined by Equation 4.32
D	diameter, m; longitudinal dispersion, m^2/s
D_{ab}	diffusivity, m^2/s
d_p	particle diameter, m
E	entrainment flux, kg/m^2s; E_z, flux at height z; E_o, flux at hypothetical bed surface; E_∞, elutriation rate, kg/m^2s
e	2.718282
F	force, N; F_b, buoyancy; F_d, drag; F_g, gravity

f	residual vector
$f(s)$	function defined by Equation 3.10
f_I	friction factor of phase I, I=g,s
G_s	solids mass flux, kg/m^2-s
$G(\theta)$	function defined by Equation 3.21
g	acceleration due to gravity, 9.81 m/s^2
$g(s)$	function defined in Equation 3.11
$H(\theta-\tau)$	function defined in Equation 3.21
ΔH	heat of reaction, kJ
h	heat transfer coefficient, J/m-s-K
J	Jacobian matrix
J_D	Colburn J-Factor
K_B	adsorption equilibrium constant for butane (ℓ/mol)
k	mass transfer coefficient, m/s
k_1	rate constant for MA formation, $mol^{1-\alpha}\ell^{\alpha}/gs$; break-up coefficient, m/s
k_2	rate constant for CO_2 formation, $mol^{1-\beta}\ell^{\beta}/gs$
k_3	rate constant for MA decomposition, $mol^{\delta-\gamma}\ell^{1-\delta+\gamma}/gs$
L	length, m
L_{eff}	effective length of detector window, m
M	molecular weight, gm/mol
N	moles
N_t	number of time steps
N_z	number of grid blocks

P	pressure, kPa
ΔP	pressure drop, kPa; ΔP_{KEg}, gas acceleration pressure drop; ΔP_{KEs}, solids acceleration pressure drop
Pe	Peclet number, uL/D; Pe_{ent}, entrance Peclet number
Q	volumetric flow rate, m^3/s
q	$\sqrt{(s/Pe + 1/4)}$
R	radius, m; universal gas constant, 0.082 ℓ.atm/mol.K
Re	Reynolds number, $\rho VD/\mu$; Re_p, particle Reynolds number $\rho V d_p/\mu$
r	radial distance, m
r_{CO2}	rate of CO_2 formation, mol/ℓ-s
r_{MA}	rate of maleic anhydride formation, mol/ℓ-s
r_{-MA}	rate of maleic anhydride decomposition, mol/ℓ-s
S	selectivity, active sites
s	parameter in Laplace transformation
T	temperature, K
t	time, (s)
U	superficial velocity, m/s
V	actual velocity, m/s; V_r, relative velocity,; V_{sl}, slip velocity; V_t, particle terminal velocity; volume, m^3
X	conversion
$\mathbf{X}$	solution vector
X_a	cross-sectional area, m^2
Z_i	height of void fraction inflection point in riser, m
z	axial distance, m

Greek Symbols

α	exponent defined by Equation 4.7; exponent in reaction rate expression, Equation 6.4
β	constant in Equation 4.17; exponent in reaction rate expression, Equation 6.5
γ	exponent in reaction rate expression, Equation 6.6
Δ	increment
δ	exponent in reaction rate expression, Equation 6.6
ϵ	void fraction; ϵ_{mf}, void fraction at minimum fluidization
θ	dimensionless time, tu/L
μ	first moment, mean; viscosity (kg/m-s)
ξ	dimensionless distance, z/L
π	3.1416
ρ	density, kg/m^3
σ^2	second moment, variance
τ	injection time, s; τ_{cap}, injection time equivalent of capsule; τ, shear stress, Pa
φ	$(r_c/R)^2$

Subscripts

a	annulus
B	bulk condition
b	butane

c	core
det	detector
f	fluid
g	gas
h	horizontal section
i	time increment
inj	injector
j	species
MAN	maleic anhydride
O	oxygen
o	inlet condition, orifice
p	particle
s	solids
susp	suspension
sys	system
T	total
v	vertical section
w	wall
1	entrance to the test section
2	exit of the test section

1. INTRODUCTION

The technology of fast fluidization dates back to the late 1930's at which time a number of petroleum companies formed a consortium to develop a catalytic cracking process. The Houdry process had been commercially available but due to excessive licensing fees ($50 million) developing an entirely new process was considered to be more economic. The first commercial up-flow catalytic cracker was put on stream in 1943 (Squires, 1986). However, due to operational difficulties, its subsequent commercial implementation was limited. It wasn't until the early 1950's, after having resolved the technical problems relating to solids flow control and developing an extremely active zeolite catalyst, that Shell reintroduced co-current gas-solids flow for catalytic cracking.

Despite the importance of catalytic cracking industrially, technical publications regarding the fluidization regime were few in number up until the late 1970's. Some notable exceptions include Zenz (1949) who incorporated a turbulent fluidization regime in his phase diagram for gas-particle systems, Lanneau (1960) and Kehoe and Davidson (1971). This lack of research may have inhibited its application to other processes and in part explains the lag of other industries behind the petroleum industry in using CFBs. Hence, the technology is not new but its application to different processes may be described as state-of-the-art.

Low gas velocities characteristic of conventional bubbling fluidized beds result in low processing capacities per unit cross-sectional area. Among the principle advantages of circulating fluidized bed systems are: high gas velocities, minimizing reactor volume, excellent heat and mass transfer, temperature uniformity and adjustable retention time of gas and solids. The behavior of CFB systems has been well qualified. However, its quantitative description is far from complete. Moreover, there is little agreement as to the meaning of fast fluidization or as to what constitutes a circulating bed.

As defined by Webster's dictionary (1966), the word circulation implies "movement or passage in a circuit or other curving or bending course typically with return to a starting point". In CFBs circulation refers to the movement of the solids phase. The solids enter the riser reactor at a tee junction and are entrained in the upward flowing gas. They exit through an elbow, are separated from the gas in a cyclone and fall into a storage vessel. The solids are then returned to the riser by various non-mechanical means such as L-valves, J-valves, etc. or mechanically by screw feeders.

Fluidization is defined as the process in which finely divided solids are suspended in a rapidly moving stream of gas that induces flowing movement of the whole (Webster, 1966). For the purposes of this study, therefore, a circulating fluidized bed system is defined as a process in which solids are entrained in a column by a high velocity gas stream and returned to the column by a re-circulation leg. It may be argued that this definition is too broad and that other systems such as spouted beds or even fluidized beds fit the definition. In fact, a spouted bed has many characteristics in common with a CFB. The geometry of the reactor is the principal difference between the two systems.

Having proposed a general definition for the CFB system, it remains to classify the principal components and quantify the behaviour. The region of industrial interest of a CFB system is the riser column in which high gas velocities entrain the solids. This region provides excellent gas-solids contacting and has been exploited for many combustion and other non-catalytic processes (Reh, 1986). Experimental studies indicate a marked segregation of particles over the cross-section (Yerushalmi et al., 1978; Youchou and Kwauk, 1980; and, Weinstein et al., 1984). Geldart and Rhodes (1986) propose that the riser consists of a dilute core region and a dense annular wall region. Kwauk et al. (1986) considered that the riser is made-up of dense agglomerated particles dispersed in a dilute continuum of discrete particles. Bolton and Davidson (1986) suggest that the lower region may be described as a slugging fluidized bed and the upper region as a lean phase.

The riser is certainly the most important region. However, it should not be considered in isolation of the other components making up the system. The design of the cyclone, downcomer or standpipe and L-valve are equally important to the process. The complexity of designing and optimizing a CFB becomes evident when considering all the factors that make-up the system. Hydrodynamically, there are many multi-phase flow regimes. For example, in the riser, there is co-current upflow. The solids exit the reactor into a horizontal pipe. Various flow regimes have been observed in the horizontal pipe connecting the riser to the cyclone varying from homogeneous to degenerate suspensions and dune flow (Patience et al., 1990). Into the cyclone the flow pattern changes to a helical motion in which particles are thrust to the outer periphery due to centrifugal forces. The particles subsequently drop onto a dense bed in the hopper, hence, counter-current or co-current downflow of solids. In the hopper and downcomer again various flow regimes may exist (Leung and Jones, 1978). In general, stand pipe flow may be characterized as sliding packed bed flow in which the particles are flowing vertically downward co-currently with the gas. Finally, the last flow regime is that in the L-valve which is described as slug flow.

In addition to the variety and complexity of the hydrodynamics, the parameters which affect the flow are numerous. Together with the geometry of the system, entrance and exit configurations, diameter and height, the physical properties of the gas and solids affect the flow phenomena. To consider all the possible experimental combinations and permutations of variables would be an imposing task. The objectives of this study were: (1) develop a simple means with which to monitor the solids circulation rate; (2) characterize the solids and gas flow in the standpipe; (3) characterize the longitudinal solids hold-up in the riser; (4) model the gas and solids hydrodynamics in the riser; (5) assess the hydrodynamic parameters by numerically simulating the partial oxidation of n-butane to maleic anhydride.

Details of the CFB unit are presented in Chapter 2. The most important experimental tools available to this study were the radioactive tracers produced by a SLOWPOKE nuclear reactor at l'Ecole Polytechnique de Montréal. Previous research on CFBs using tracer techniques are severely limited by the injection and detection methods. Generally, large volumes of tracer are required in order to facilitate its detection. Unfortunately, large volumes introduce large perturbations thus measurements are not representative of system characteristics. Moreover, the high velocities and short distances requires very short detection times. Visual techniques such as coloured dyes are impractical to study the riser hydrodynamics. The gas phase was analyzed with radioactive argon and the solids phase with Si-28. Tracer studies of this nature have not been exploited to a great extent in the literature.

In Chapter 3, the mathematical tools necessary to analyze the data are given. A general computer program to solve one-dimensional coupled partial differential equations is discussed. A simple problem is developed to demonstrate the finite difference method employed. In addition, the analytical methods used in RTD analysis are discussed. The injection and detection input functions are developed.

The standpipe hydrodynamics and measurement of the solids hold-up are detailed in Chapter 4. Solids mass fluxes based on particle wall velocities in the riser were measured to be approximately 50% of the value obtained from tracer studies. A simple correlation is developed to relate the pressure drop in the horizontal section between the riser and cyclone to solids circulation rate. In addition, results concerning the effect of riser conditions on standpipe operation are presented. Finally, the various hydrodynamic models proposed to characterize the longitudinal suspension density in the riser are discussed together with pressure drop measurements in the experimental unit.

The results of radioactive gas and solids tracer studies are summarized in Chapter 5. Considerable efforts were directed towards modelling the injectors to minimize systematic errors. Average injection times of the argon were 0.07 s. Solids injection times were between 0.3 and 0.45 s. Longitudinal variations in the gas and solids phase are detailed as well as the effect of particle diameter. A two zone model is used to describe the comportment of both the solids and gas phase. Mass transfer coefficients between the two zones is higher for the gas than for the solids. The gas phase is essentially in plug flow whereas considerable dispersion and downflow along the wall characterize the solids behaviour.

In Chapter 6, a computer program is developed to simulate the selective oxidation of butane to maleic anhydride. The program is used to quantify the importance of the various hydrodynamic parameters proposed to model the riser hydrodynamics. Various models are tested from a simple single phase model (Patience and Chaouki, 1990) to a two zone model with varying mass transfer coefficients longitudinally. Total butane conversion is found to be sensitive to both the core radius and the gas cross flow coefficient.

2. EXPERIMENTAL

2.1 APPARATUS

The CFB experimental system, illustrated in Figure 2.1, consists of two parallel columns 5 m high; a riser reactor and a re-circulation leg. Solids are introduced into the riser from an L-valve just above an orifice plate distributor, they are entrained in the upward flowing gas, exit through an abrupt reducing elbow into a tube and, finally, are separated from the gas phase in a cyclone. The particles are returned to the storage hopper and the gas exits through a manifold to a knock-out drum and is vented to atmosphere.

2.1.1 Riser reactor

The riser column is comprised of 4 flanged schedule 10 stainless steel pipes 1 m long and 82.8 mm in diameter. Partial visual observation of the flow is possible through a window port 35 mm in diameter mounted on one of the pipes. A windbox, distributor (an orifice plate 6.4 mm thick with 115 holes 3.2 mm in diameter distributed on a square pitch) and a tee make up the entry section of the air and solids. The gas exit an abrupt reducing elbow (82.8 mm to 41 mm) at the top. Male NPT fittings 6.4 mm in diameter are distributed along

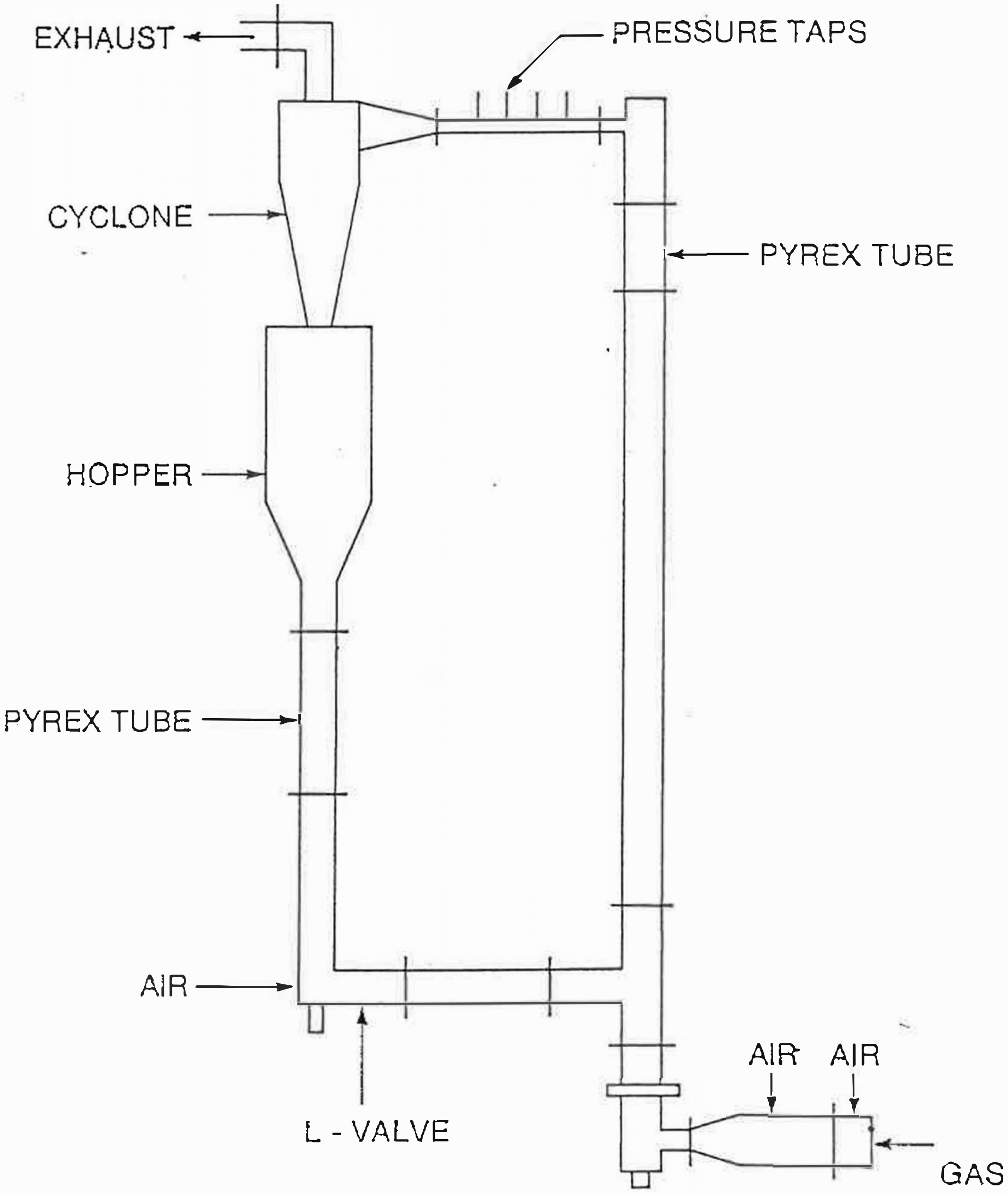

Figure 2.1: Circulating Fluidized Bed

the length of each section at intervals of 150 mm and serve as taps for pressure probes and thermocouples. A pyrex tee was used for visual study of the solids at the entrance and a pyrex tube, 300 mm long, permitted visual observation at the exit.

2.1.2 Re-circulation leg

A maximum of 60 kg of 60 mesh sand can be stored in the storage hopper and standpipe. The hopper, illustrated in Figure 2.2, is 229 mm in diameter 890 mm long. Solids separated from the gas in the primary cyclone spiral downward into the hopper. A blanked off port is mounted on the side to permit the installation of a second cyclone. In addition, a threaded pipe with an easily removed cap is used to charge the system with solids and for solids make-up.

The L-valve downcomer assembly consists of three flanged schedule 10 stainless steel pipes one metre long and 82.8 mm in diameter. As in the riser, taps for pressure and temperature measurements are distributed along the length of the re-circulation leg. The horizontal section of the L-valve, between the downcomer and riser, is also 82.8 mm in diameter.

A one metre pyrex tube, 76.4 mm in diameter, is used for visual observation of the flow regime as well as for solids circulation rate studies. The technique used to determine the mass flux, called the

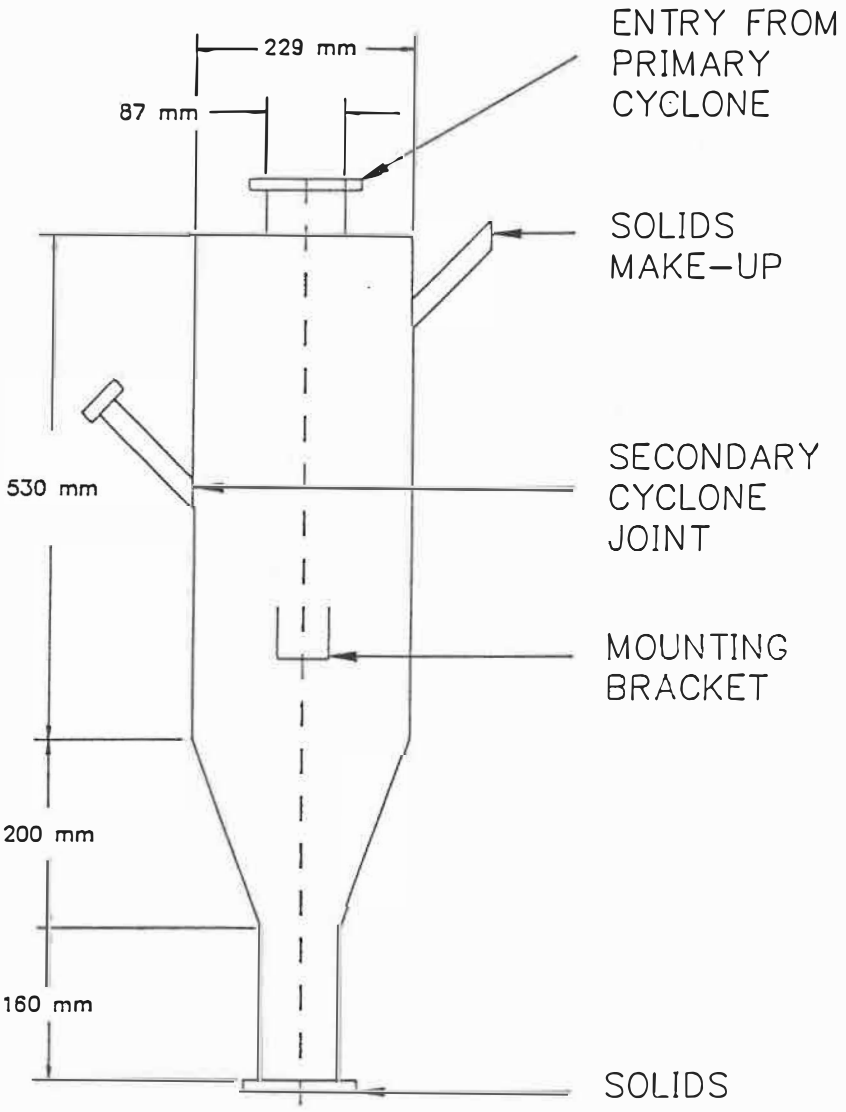

Figure 2.2: Solids Hopper

time-of-descent method (Burkell et al., 1988), entails measuring the time it takes for a discrete particle to traverse a known distance. The calculated velocity multiplied by the bed density gives the mass flux in the pyrex. To obtain the mass flux in the column, the calculated value in the pyrex tube must be multiplied by the ratio of cross sectional area of the pyrex by the cross sectional area of the column. An additional correction factor is required that accounts for the fact that the observed wall velocity does not correspond to the actual solids bulk velocity. Further detail is given in Section 4.2.

Metered building air, introduced at the elbow, is used to control the solids circulation rate. Various locations of air injection were tested. Greatest ease of circulation was obtained with aeration in the standpipe 210 mm from the bottom. Optimization of the location and geometry of the air injector was attempted. However, little improvement in circulation rate was realized. Higher circulation rates were obtained when the length of the horizontal section of the L-valve was reduced from 300 mm to 600 mm. The solids flow in the standpipe was much smoother. Aeration requirements were significantly reduced at higher temperatures.

The last element of the CFB system is the exhaust-separation assembly at the top of the unit. The gas-solids mixture exits the reactor through an abrupt reducing elbow into a 41 mm flexible tube that leads to a cyclone. The cyclone, shown in Figure 2.3, is 790 mm long and 190 mm in diameter at the top then tapers down at the exit to 90 mm. The exhaust tube is 95 mm in diameter. Stainless steel is used throughout. A steel plate 150 mm long, 80 mm wide and 10 mm thick is welded to the solids entrance point to minimize replacement downtime. Significant abrasion occurs in this region.

2.1.3 Air metering

Building air is metered through a calibrated orifice, passes through a Norgen Compressed Air Filter (model F17-600-MIDA), a Norgen Compressed Air Regulator (model R17-600-RNLA) and is separated into three streams. The flow rate of primary air is measured by a Hedland rotameter (model 570-050, maximum rating 1.4 m^3/min) and is fed into a natural gas burner. Secondary air, metered by a second Hedland rotameter (model 771-200, maximum rating 6.3 m^3/min) contacts the hot gases from combustion chamber in the diffuser. The temperature in the reactor is effectively controlled by adjusting the ratio of secondary air to primary air. The third air stream passes through one of two rotameters that measures the air flow rate to the L-valve. Esko LH-6FFV and Esko LH-5CD rotameters with maximum ratings of 4.8 m^3/hr and 1.8 m^3/hr were used to meter the air. The upstream pressure to the rotameters was maintained at 446 kPa. Initially, a much higher pressure was used but operation difficulties were experienced due to the pressure fluctuations of the building air. Fluctu-

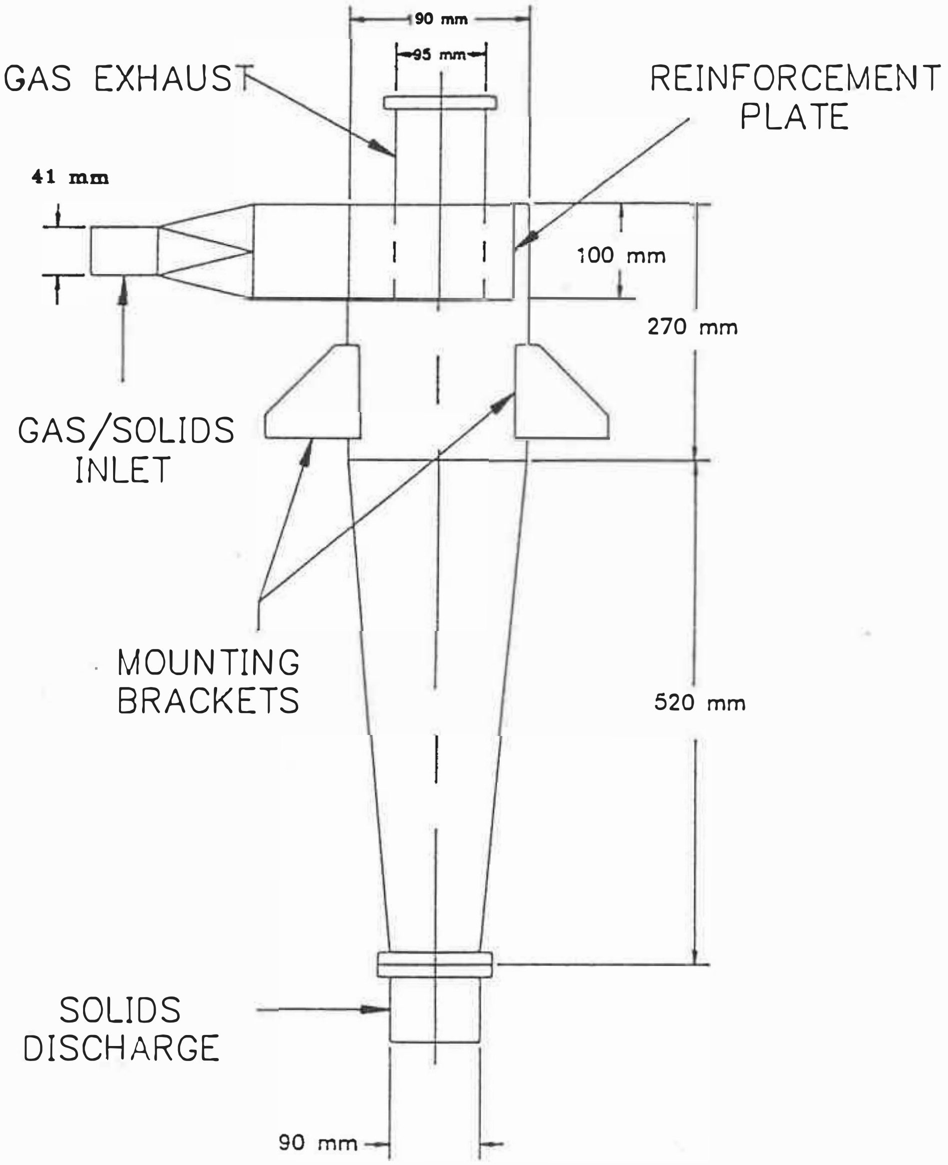

Figure 2.3: Cyclone

ations in pressure of over 400 kPa are not uncommon. These fluctuations had little to no effect on the operation when the upstream pressure to the rotameters was 446 kPa. A schematic diagram of the air system is given as Figure 2.4

2.2 RADIOACTIVE TRACERS

Both the behaviour of the gas phase and particulate phase are studied using radioactive tracers. Radioactive argon was used for the gas phase and Al-28 was used for the solids phase. Two NaI scintillators, adequately shielded with lead bricks, are used to detect the gamma rays emitted. A Canberra Series 35A analyzer, counting in the multi-scaling mode, records the pulses of radioactivity. The multi-scaling mode counts all pulses regardless of amplitude. This mode is particularly useful for recording time dependent phenomena since the signals are stored in separate channels allocated sequentially. The sampling time, known as the dwell time, is set by the operator and varies according to the dynamics of the system. A dwell time of 0.02 s is used for both the gas phase and solids phase experiments.

2.2.1 Solids phase

A 10 gram sample of sand is irradiated in the fast neutron flux of a SLOWPOKE nuclear reactor. Si-28 is converted to Al-28 which has

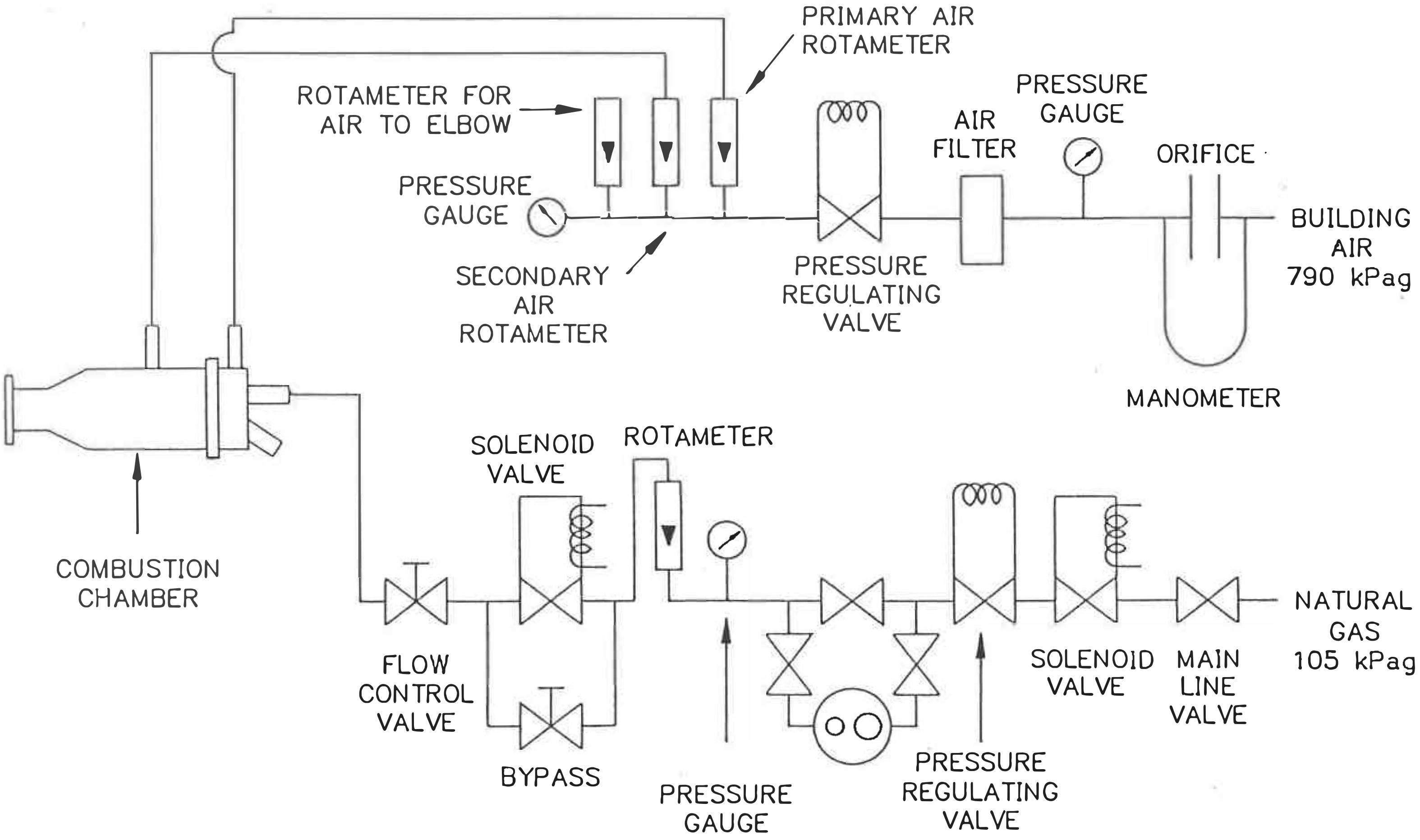

Figure 2.4: Natural Gas and Air Lines

a half life of 2.24 minutes and emits high energy gamma rays. The RTD of three sand diameters, 109 μm, 275 μm, 525 μm were studied. The radioactive sand is injected into the reactor by compressed air.

The injection system is illustrated in Figure 2.5. V1 and V2 are ball valves and V3 is a male Swagelok quick connect (normally open). In order to minimize the volume of the injector, and thus the perturbation when introducing the tracer, 6.25 mm stainless steel pipe was used throughout. Further detail of the injector pulse is given in Section 5.2.

The injection procedure is as follows: With V3 closed and V2 disconnected (therefore, the system is open to the atmosphere but isolated from the reactor) V1 is opened and the injector is loaded with sand via a funnel. V1 is closed and V2 is connected to a female quick connect exposed to some pressure. V3 is quickly opened and closed. By monitoring the system pressure the time taken to close and open V3 was determined to be on the order of 0.5 seconds. The sand passes in front of the photo-diode and triggers the radioactive counter establishing time zero.

Initially building air at 790 kPa was used. However, this high pressure perturbed the system significantly as demonstrated in Figure 2.6. The pressure drop was monitored at the injection point and in the horizontal section between the riser and the cyclone. When V3 is

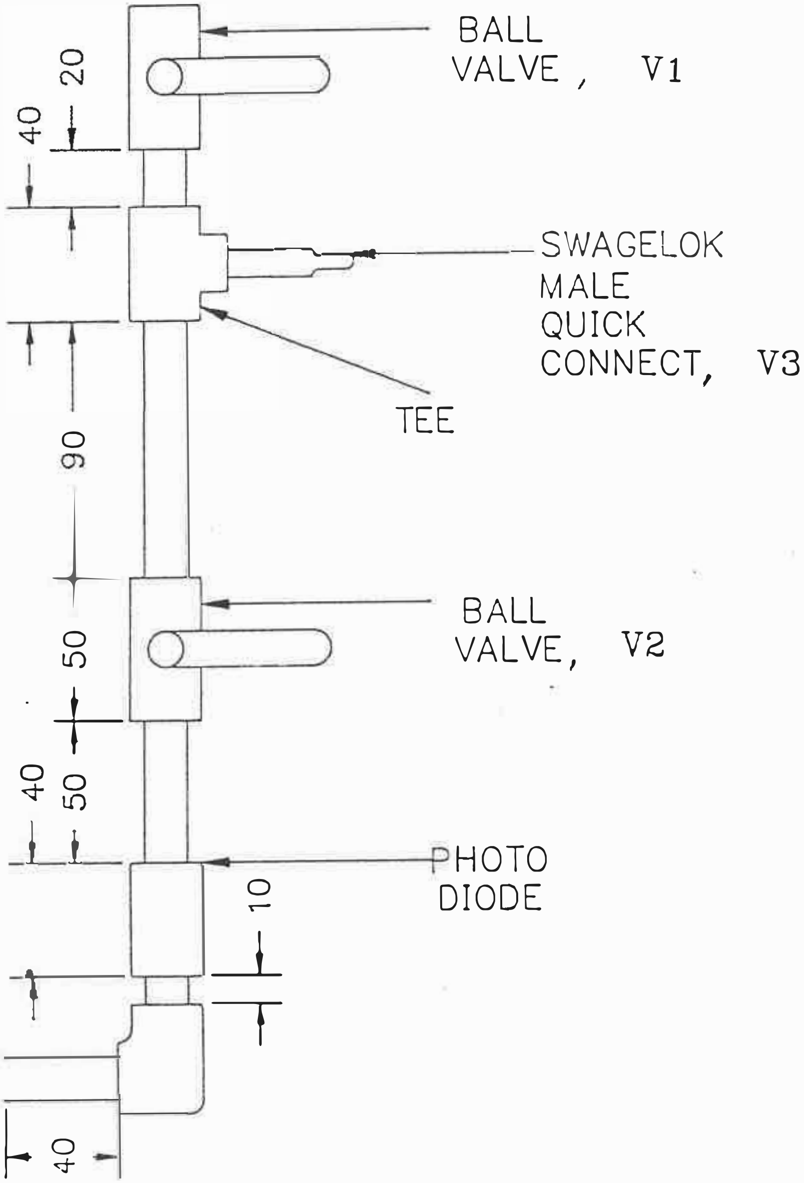

Figure 2.5: Solids Tracer Injector

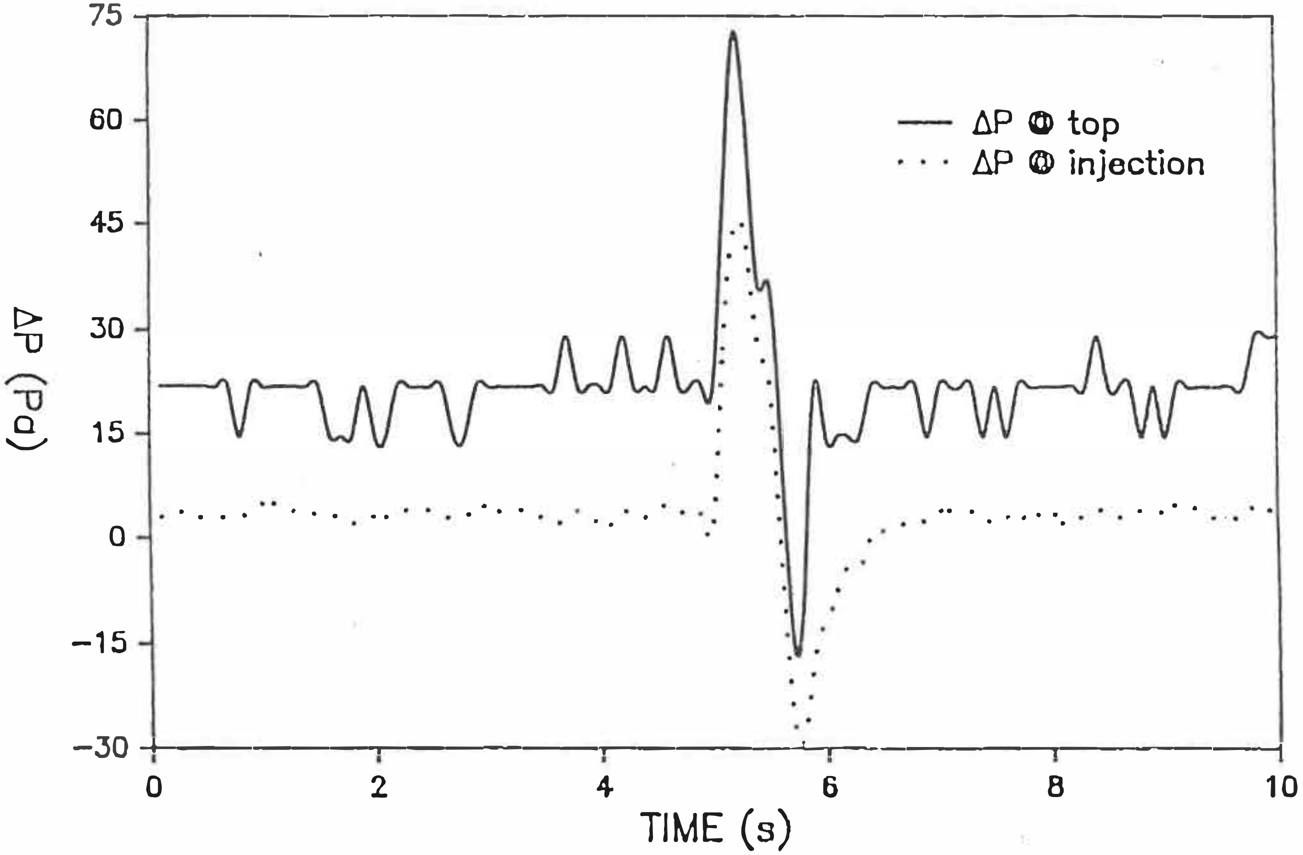

Figure 2.6: Pressure Perturbation of Solids Tracer Injector
P = 790 kPa

opened, the pressure drop increases significantly, corresponding to the increased flux of air flowing past the first pressure tap. It quickly drops back to a steady value. When V3 is closed, the inverse occurs, i.e. the pressure drop becomes negative and then regains the steady value. Clearly the distortion introduced by injecting sand at 790 kPa of air is unacceptable. Lower pressure air is required to minimize the perturbation and for this reason air at 446 kPa was tested. Unfortunately, there was little improvement. Finally, a side stream of air bled off from the air line downstream of the secondary rotameter was used. Opening and closing V2 had no measurable effect on the pressure drop neither in the vicinity of the injector nor at the top of the column. As a brief note, it should be emphasized that the valve must be closed quickly otherwise the results of the RTD become skewed. Particles initially stuck in the injector break loose and eventually enter the reactor. Best results were obtained when the valve was opened and closed as rapidly as possible.

2.2.2 Gas phase

The gas phase is studied using radioactive argon. Argon is particularly suited as a gas tracer because it is inert and its molecular weight is near that of air thus minimizing any difference in molecular diffusivity. All measurements are made using a nine milligram sample. Argon (Ar 40) is irradiated forty minutes in the neutron flux of a SLOWPOKE nuclear reactor and is converted to Ar-41 which emits beta and gamma rays and has a half life of 1.8 hours. This long half life would prohibit the facility of making many measurements per day in the solids phase. However, it is ideal for gas phase measurements because the gas is not re-circulated as the solids are.

A novel and quite simple injection technique was developed for the gas tracer. Since the residence time of the gas can be much less than one second, the injection time must be extremely short to render the data analysis simple. However, the shorter the injection time the greater the perturbation introduced is a general axiom regarding injection analysis. Therefore, the tracer must be injected in the shortest time possible without perturbing the system. Furthermore, as will be discussed in Chapter 3, the actual injection time is required to calculate the first and second moments.

These criteria were met using two syringes, a one way valve (used in chromatography), two micro switches, a data acquisition system and a computer. The system is illustrated in Figure 2.7. The one way valve consisted of a 6.35 mm male NPT fitting welded on to a 11 mm male pipe thread, a rubber disc 12 mm in diameter and 3 mm thick and a threaded cap with a 2 mm hole at the top. The injector consisted of a 5 ml syringe that is charged with argon and an identical blank syringe on which one micro switch was mounted and a support. A plastic strip, glued to the plunger of the blank syringe, was used to

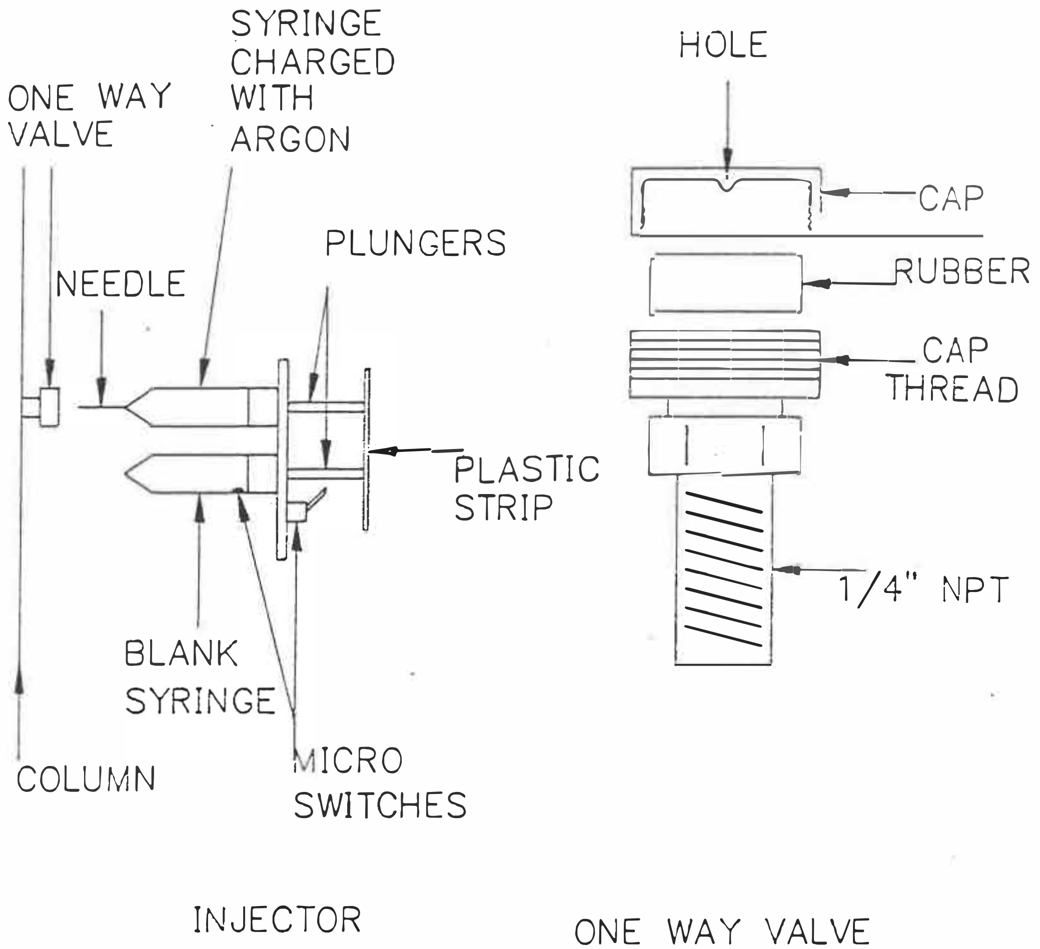

Figure 2.7: Gas Tracer Injector

push the plunger of the syringe full of argon. The plunger of the blank syringe passes over the first micro switch activating the counter in the computer. At the bottom of the stroke the plastic strip pushes the lever of a second micro switch and thus stops the counter. The elapsed time is displayed on the computer screen. On average, the gas sample is injected in 0.07 seconds. The velocity of tracer at the tip of the needle was calculated to be over 100 m/s for injection time less than 0.07 s. Considering the high injection velocities, the intense solids mixing at the entrance and the relatively narrow column, the argon is assumed to be distributed uniformly across the radius of the reactor.

2.3 DATA ACQUISITION AND MEASUREMENTS

2.3.1 Pressure

Two Viatran 219 pressure transducers measure the pressure fluctuations in the column. The time constant of the transducers is 0.5 ms for a 90 % full scale reading. The sampling time was 0.3 ms. Two diaphragms with maximum pressures of 2000 Pa and 10000 Pa are used. Swagelok 0.7μ on-line filters, mounted on the reactor, prevent particles from migrating into the pressure lines. Building air at 790 kPa is used to flush or backwash the filter when blocked. All pressure taps are mounted flush to the pipe wall. Eleven taps are distributed over the length of the column to determine the pressure drop and hence local solids hold-up. Swagelok quick connects connect the pressure lines to a four way valve. Great lengths were taken to protect the transducer and diaphragm from excessive pressures. The four way valve in the closed position isolates the transducer from any pressure lines. In the open position each side of the transducer is exposed to the corresponding pressure line. The procedure to connect the transducers was as follows:

(1) Close the four way valve.

(2) Connect the female quick connect (normally closed) to the male quick connect (normally closed) which is attached to the 7 μ filter at the column.

(3) Open the four way valve.

(4) Initiate program to take readings and average results over a 30 s interval.

Pressure taps are also placed in the vertical section between the riser and cyclone. The pressure drop in this region has been found to be linearly related to the mass flow rate (Patience et al., 1989). The solids mass flow rate measuring technique is discussed in greater detail in Chapter 4.

The pressure transducers are interfaced with an Omega data acquisition system. A program, written in Turbo-Pascal, provides an efficient and fast means of data retrieval. This is particularly important for systems such as CFBs for which the frequency of the pressure fluctuation is on the order of milliseconds.

2.3.2 Radioactivity calibration

A number of correction factors are required to standardize the data. For example, since the half life of the Al-28 is so short (2.24 min) a decay time correction factor is required so that the results correspond to the same reference time. In general, the sand was irradiated 4 minutes and injected 3 minutes after coming out of the nuclear reactor. The activity of the sand passing in front of the detector at 4 minutes is 73 % lower than at 3 minutes. The following correction was introduced to correct for the decay:

$$I_{c1} = I_R \, e^{+.005157t} \tag{2.1}$$

This correction is unnecessary for the argon since the half life is on the order of 1.8 hours and the average residence time is on the order of seconds.

The second correction factor required is that due to dead time or pile up. All of the gamma rays are not counted at high intensities because of pulse interference (Kennedy, 1989). Therefore, the following equation is used to correct for this:

$$I_{c2} = I_R/(1 - 0.0000033 I_R) \tag{2.2}$$

2.3.3 Reactor shielding

Background radiation is a result of the existence of natural radioactivity in the environment and the cosmic radiation that continuously bombards the earth's atmosphere. The magnitude of the background radiation determines the minimum detectable radiation level and therefore shielding is necessary in order to enhance the quality of the signal. Since the second moment is dependent on the square of time, significant errors are introduced by inadequate shielding in which long tail sections are evident. Moreover, the irradiated sand accumulates in the hopper region and could adversely affect the results if detected. Therefore, large quantities of lead are used to shield the detector. Lead is a high density material with a large atomic number that is frequently used for reducing background radiation. In addition, sufficient quantities of sand were maintained in the hopper so that recirculated irradiated sand was not detected twice in the same experimental run.

The first detector, located near the bottom of the reactor, is encased in lead bricks. The effective window is 65 mm long (measurable vertically) by 120 mm wide. There is 90 mm of lead on top of the detector and the base is 145 mm thick. The detector is not flush with the bricks of the face but 53 mm into the bricks as illustrated in Figure 2.8. Initially, the lead encasing was flush to the pipe

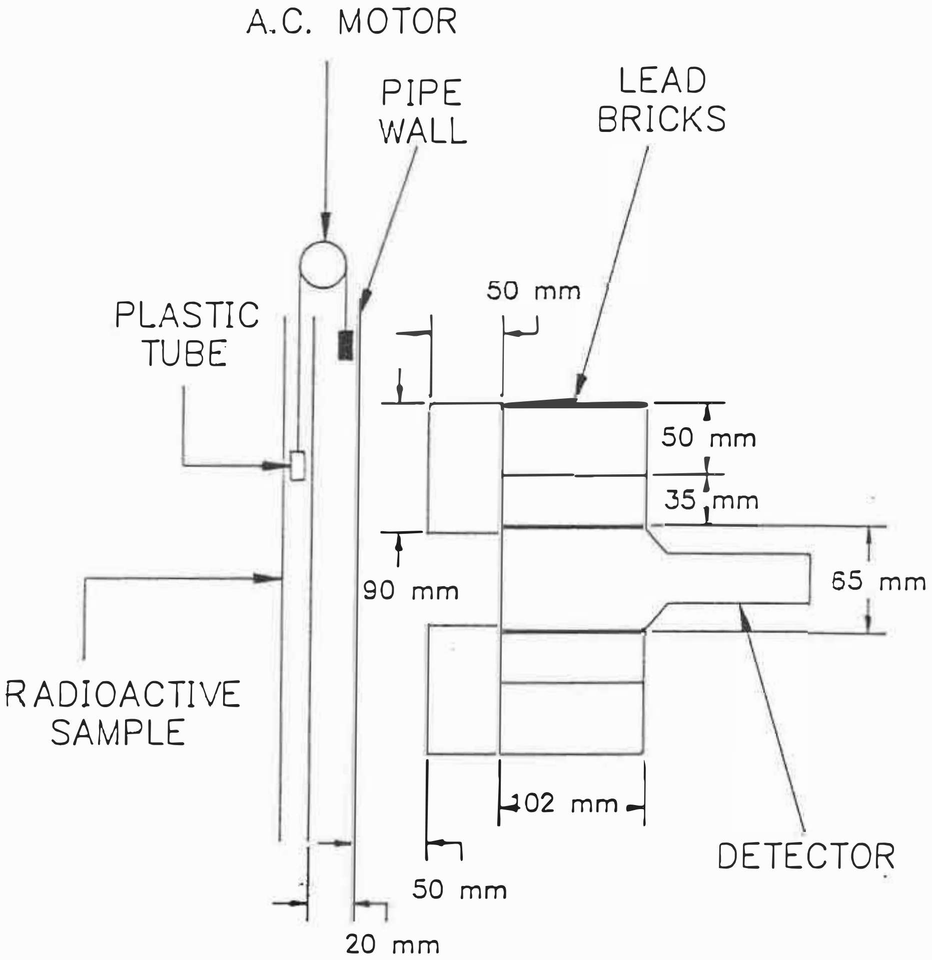

Figure 2.8: Detector Calibration Assembly

wall but was later moved back 25 mm because of heating as a result of the experiments at high temperatures. Moving the detector further away from the reactor effectively decreases the "window", the effective area in which the detector sees the radioactivity. In order to calculate the active window, a point source of radioactivity is dragged in front of the detector at a known velocity. The first and second moments are then calculated from the output signal. The results of the tests are presented in Section 3.2.

2.4 PARTICLE PROPERTIES

The physical properties of the sand used throughout the experiment are summarized in Table 2.1. The results of a sieve analysis, from which the Sauter mean diameter is calculated, is given in Table 2.2. The density of the sand was determined by measuring the volume of water displaced by a known mass of sand. The minimum fluidization velocity was determined experimentally.

Table 2.1: Sand Physical Properties

Property	
Sauter mean diameter, d_p (μm)	277
Density, ρ_p (kg/m^3)	2630
Bulk density, ρ_b, (kg/m^3)	1630
Density at minimum fluidization, ρ_{mf}, (kg/m^3)	1550
Voidage at minimum fluidization, ϵ_{mf}	0.41
Loose packed voidage, ϵ_{lp}	0.40
Vibrated bed voidage, ϵ_{vb}	0.34
Minimum fluidization velocity, u_{mf} (m/s)	0.052
Particle terminal velocity, u_t (m/s)	1.9
Sphericity (estimate)	0.87
Archimedes' Number	2000

Table 2.2: Sieve Analysis

Mesh	d_p (μm)	Weight %
40^+	500	12.9
40^- 45^+	390	23.9
45^- 50^+	328	23.1
50^- 60^+	275	20.5
60^- 80^+	215	9.7
80^- 100^+	165	2.3
100^- 120^+	138	2.3
120^-	100	5.3

3. MATHEMATICAL ANALYSIS

The hydrodynamics of reactors, heat exchange equipment and process vessels may be analyzed using simple methods including the measurement of the residence time distribution (RTD). The flow behaviour is often modelled as either mixed flow or plug flow as a first approximation. Parameters are then introduced to characterize non-ideal behaviour such as diffusion, dead zones, and by-passing. The axial dispersion model, longitudinal dispersion superimposed on plug flow, has been the subject of many studies in the scientific literature among which the earliest, most notable contributions, are those of Taylor (1953, 1954a,b) Danckwerts (1953), and Lapidus and Amundson (1952). More recently, an experimental technique, dubbed "flow injection analysis" (f.i.a.), has emerged in which the phenomenon of diffusion is the mechanism used to differentiate various chemical species. Ruzicaka and Hansen (1986) report that from 1975 to 1986 at least 804 papers have been published concerning the theory and applications of f.i.a. In view of the exponential increase in the number of publications concerning axial dispersion applied to analytical chemistry, the number of studies in the field of chemical engineering may seem some what meager. One of the principal difficulties is characterizing complex multi-phase systems, such as circulating fluidized bed reactors (CFB), with simple experimental and analytical techniques. Furthermore, the axial dispersion model, although conceptually straightforward, is complicated by the assumed boundary conditions, injection pulse and method of detection.

Among the first contributions to determine the mean residence time and the dispersion coefficient experimentally and analytically was that by Levenspiel and Smith (1957). A doubly infinite system was assumed with an ideal Dirac δ-function input of tracer. Van der Laan extended this work to include the various boundary conditions given by Wehner and Wilhelm (1956). Aris (1959), corrected by Bischoff (1960), maintained that the Dirac δ-function input, although convenient mathematically, was an impossible experimental task. Therefore, he suggested that it would be more appropriate to measure the concentration at two points within the system. The difference between the first moments and second moments were shown to be directly related to the mean residence time and axial dispersion respectively. Bischoff and Levenspiel (1962) extended this study to include various injection positions and boundary conditions.

Whereas the mathematical analysis of chemical engineering systems is generally limited to ideal input functions such as the Dirac δ-pulse, step and sinusoidal, a number of input functions have been considered in the field of gas chromatography. Sternberg (1966) determined the first and second moments of various time dependent pulses including a plug (also known as a bolus, slug, square wave or block function), Gaussian, exponential, and reverse ramp injection to name a few. The mathematical treatment of non-ideal pulses is considered by Michelsen and Ostergaard (1970). Westerterp et al. (1984) give a brief summary of the methods used to estimate the model parameters given the experimental data. Injection analysis is further complicated due to the fact that the moments depend on the input distribution of tracer across the radius (Levenspiel et al., 1970). In f.i.a. special manifolds are used to distribute the tracer across the radius. Brereton (1987) injected tracer in the wind box upstream of the circulating fluidized bed reactor (CFB) to ensure an even distribution at the inlet.

Hsu and Dranoff (1986) discuss, in some detail, the initial conditions and compare a number of exact solutions given in the literature for both the δ-pulse and step input. The only exact solution for a bolus injection is that of Lapidus and Amundson (1952) who considered packed bed flow particular to gas chromatography. Together with these analytical expressions a number of numerical techniques have been applied to the axial dispersion problem (Ananthakrshnan et al., 1965; Bate et al., 1973; Vanderslice et al., 1981; Kolev and Pungor, 1987). Whereas analytical treatments have been restricted to idealized input functions, no such limitations exist for numerical approaches. Moreover, numerical methods are not limited to plug flow approximations of the inlet flow distribution. However, one of the shortcomings of numerical solutions and in particular finite difference methods, is that a large number of grid blocks and time steps are required to minimize the effects of numerical dispersion introduced by the discretization of the partial differential equations.

In the following section, the solution to the axial dispersion problem, as originally proposed by Lapidus and Amundson (1952) is discussed. A synthesis of a number of important contributions concerning the implications of the assumed boundary conditions and input function is given. Expressions for the mean and variance are derived using the Laplace transform method and shown to be in agreement with the results of Sternberg (1966) and consistent with convolution analysis. Expressions for the second moment contribution to the variance introduced by the detector and housing geometry are derived. In addition, the numerical method used together with a brief sensitivity analysis is detailed.

3.1 ANALYTICAL APPROACH

For turbulent flow in pipes it is reasonable to assume that the radial variation of concentration and velocity are small and therefore approximate the system as one-dimensional. This one dimensional approach is often valid for packed bed flow as well. The convection dispersion model describing this system is given as

$$\frac{\partial C}{\partial t} + u \frac{\partial C}{\partial z} = D \frac{\partial^2 C}{\partial z^2} \tag{3.1}$$

and in non-dimensional form as

$$\frac{\partial C}{\partial \theta} + \frac{\partial C}{\partial \xi} = \frac{1}{Pe}\frac{\partial^2 C}{\partial \xi^2} \tag{3.2}$$

where, the Peclet number, Pe, is a measure of the extent of axial dispersion.

3.1.1 Boundary Conditions

Danckwerts (1953), originally proposed a mass continuity boundary condition at the entrance and a zero concentration gradient at the exit:

$$C(0^-,\theta) = C(0^+,\theta) - \frac{1}{Pe}\frac{dC}{d\xi}(0^+,\theta) \tag{3.3}$$

$$\frac{dC}{d\xi}(1,\theta) = 0 \tag{3.4}$$

These conditions correspond to what is commonly referred to as a closed-closed system. Many boundary conditions have been proposed that take into account the various flow scenarios at the boundaries (van der Laan, 1958;, Bischoff and Levenspiel, 1962). The boundary and initial conditions considered by Lapidus and Amundson (1952) are given by:

$$f(\theta) = C(0,\theta)/C_o = \begin{cases} 1 & 0 < \theta < \tau, \quad \xi = 0 \quad (3.5) \\ 0 & \theta > \tau, \quad \xi = 0 \quad (3.6) \end{cases}$$

$$\frac{\partial C}{\partial \xi}(\infty,\theta) = 0 \qquad 0 < \theta, \quad \xi = \infty \qquad (3.7)$$

$$C(\xi,0) = 0 \qquad (3.8)$$

Neither the assumptions nor the limitations regarding these boundary conditions were discussed. Equation (3.7) is well known as an open boundary condition. However, it may be shown that Equations (3.5-7) are reasonable approximations to the Danckwerts boundary conditions at a high Peclet number. The error is equal to the inverse of the Peclet number. For Pe=100 the error is 1%.

3.1.2 Laplace Transform

The transport equation has been solved in the past using the method of Laplace transforms. The reader is referred to the work of van der Laan (1958) for greater detail. Briefly, the Laplace transform of Equation (3.2) leads to an ordinary differential equation for which the general solution is of the following form:

$$C^T(\xi,s) = C_1\, e^{(q+1/2)Pe\xi} + C_2\, e^{-(q-1/2)Pe\xi} \qquad (3.9)$$

The Laplace transform of the boundary condition 3.5-6 is:

$$f(s) = \int_0^\infty e^{-s\theta}\, f(\theta)\, d\theta \;=\; \frac{1 - e^{-\tau s}}{s} \qquad (3.10)$$

Solving for the constants C_1 and C_2 in Equation 3.9 results in the general solution:

$$C^T(\xi,s) = f(s)\,g(s) = \left[\frac{1-e^{-\tau s}}{s}\right]\left[e^{-(q-1/2)Pe\xi}\right] \tag{3.11}$$

As indicated by van der Laan (1958), the first and second moments may be calculated in the 's' domain without having to perform the back transformation. It is a simple matter of differentiating the general solution with respect to 's' and taking the limit as 's' approaches zero. Michelsen and Ostergaard (1970) have derived the moments for a double infinite system. More general expressions with which to determine the first and second moments are given as Equations (3.12-14).

$$\mu_{s\to 0} = \frac{C'(\xi,s)}{C(\xi,s)} = -\frac{f'(s)}{f(s)} - \frac{g'(\xi,s)}{g(\xi,s)} \tag{3.12}$$

$$\sigma^2_{s\to 0} = \frac{C''(\xi,s)}{C(\xi,s)} - \left[\frac{C'(\xi,s)}{C(\xi,s)}\right]^2 \tag{3.13}$$

$$= \frac{f''(s)}{f(s)} - \left[\frac{f'(s)}{f(s)}\right]^2 + \frac{g''(\xi,s)}{g(\xi,s)} - \left[\frac{g'(\xi,s)}{g(\xi,s)}\right]^2 \tag{3.14}$$

The expressions involving g(ξ,s) have already been determined for a number of boundary conditions (van der Laan, 1958; Bischoff and Levenspiel, 1961). The first and second derivatives with respect to 's' are for the input pulse are:

$$f'(s) = -C_o\left[\frac{1-e^{-\tau s}}{s^2} - \tau\frac{e^{-\tau s}}{s}\right] \tag{3.15}$$

$$f''(s) = C_o \left[\frac{2(1 - e^{-\tau s})}{s^3} - 2\tau \frac{e^{-\tau s}}{s^2} - \tau^2 \frac{e^{-\tau s}}{s} \right] \qquad (3.16)$$

Taking the limit a 's' goes to zero and applying l'Hôpital's rule results in the following expressions for the bolus injection:

$$\frac{f'(s)}{f(s)} = \frac{\tau}{2} \qquad (3.17)$$

$$\frac{f''(s)}{f(s)} - \left[\frac{f'(s)}{f(s)}\right]^2 = \frac{\tau^2}{12} \qquad (3.18)$$

Equations (3.17) and (3.18) correspond to the first and second moments derived by Sternberg (1966) by integration in the time domain for a bolus injection. Included in his analysis are expressions for the mean and variance for other input functions common to gas chromatography such as a gaussian, exponential, ramp, etc.

The mean and variance of the system, $g(\xi,s)$, are calculated in the same manner as that for the input pulse. The resulting mean and variance of Equation (3.2) subject to the boundary and initial conditions given as Equations (3.5-8) are:

$$\mu = \frac{\tau}{2} + 1 \qquad (3.19)$$

$$\sigma^2 = \frac{\tau^2}{12} + \frac{2}{Pe} \qquad (3.20)$$

Finally, the inverse Laplace transform of Equation (3.14), as derived by Lapidus and Amundson (1952), is,

$$G(\theta) = \frac{1}{2}\left[\operatorname{erfc}\left[\frac{\sqrt{Pe}}{2}\,\frac{\xi-\theta}{\sqrt{\theta}}\right] + e^{Pe\,\xi}\operatorname{erfc}\left[\frac{\sqrt{Pe}}{2}\,\frac{\xi+\theta}{\sqrt{\theta}}\right]\right] \qquad (3.21)$$

$$\frac{C(\xi,t)}{C_o} = G(\theta) - H(\theta-\tau)\,G(\theta-\tau) \qquad (3.22)$$

3.1.3 Significance of Assumed Input Function

Most analytical treatments regarding RTD assume a δ-pulse as the input function. Mathematically, it is more convenient to work with a δ-pulse as opposed to a finite pulse function. This assumption has been verified under laminar flow conditions at high Peclet numbers experimentally and analytically (Vanderslice et al., 1981). Similar studies have not been made for the more simple case of plug flow. Figure 3.1 illustrates the effect of the injection time of a bolus on the calculated response curve at a Peclet number of 100. In regarding the curves it seems evident that the δ-pulse input is a reasonable approximation for injection times up to 10% of the mean residence time. There is very little difference between the two curves whose injection time is 5% and 10% respectively of the mean residence time. As the injection time is increased the height of the maximum concentration decreases and the concentration curve spreads out. These results may be misleading if regarded in isolation without consider-

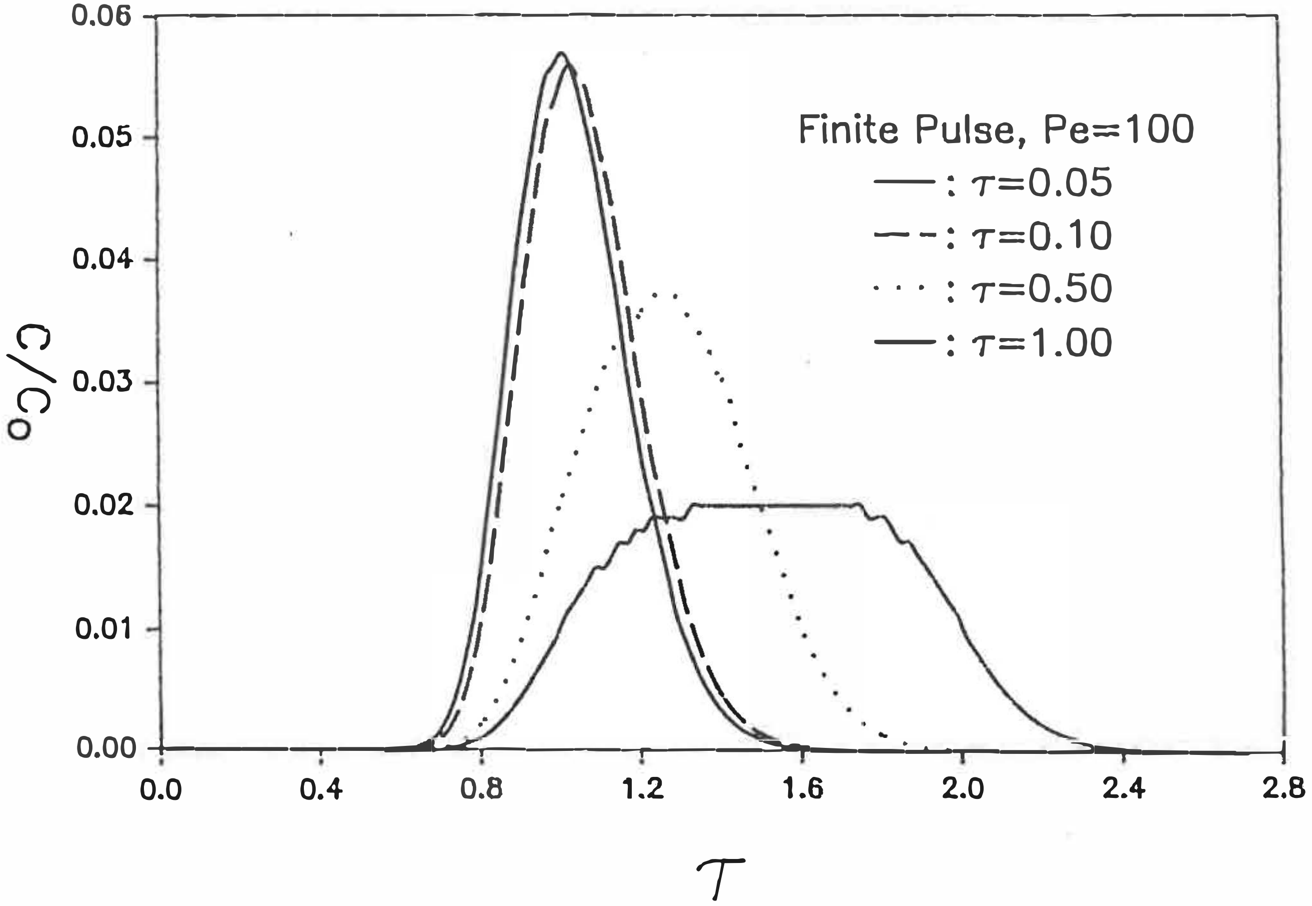

Figure 3.1: Concentration Variation with Input Pulse

ing the boundary conditions on which the model is based. Furthermore, the mean and variance may be calculated from Equations (3.19) and (3.20). The error in assuming a δ-pulse is only 2.5% for a system in which the injection time is 5% of the mean residence time. The error of the variance depends on both the injection time and the Peclet number. At Pe=100, the error in assuming a δ-pulse is only 1% for an injection time 5% of the mean residence time.

RTD measurements were made for both the gas and solids phase in the riser and in the standpipe. Injection times of 0.07s are characteristic of the gas injector. A δ-pulse is a good approximation when the mean residence time is greater then 0.7 s and is assumed for gas and solids phase measurements phase measurements in the standpipe. In the riser mean residence time much less than 0.7 s are measured, particularly for short distances between the injector and detector, therefore, a δ-pulse is a poor assumption and the actual input function must be determined. The dispersion contribution of the solids injector is much greater than the gas injector. The input function, determined by measuring the variation of pressure drop with time in the injector, is more like an isosceles triangle than a bolus. In addition, there is a delay of about 0.05s from the time the analyzer commences detecting and the solids first enter into the reactor. Both injectors are calibrated by measuring the RTD in an empty column then comparing with published data. A complete analysis is presented in Section 5.1 and 5.2. Briefly, the gas injection pulse is not square as first assumed but more like a skewed gaussian and has been approximated by a bolus with a delay.

3.1.4 Detector Variance

The total apparent dispersion, as recorded by the analyzer, is a result of the dispersion in the system, the input function and detection method and is expressed by,

$$\sigma_T^2 = \sigma_{inj}^2 + \sigma_{sys}^2 + \sigma_{det}^2 \tag{3.23}$$

The second moment contribution of the injector is small when the injection time is much less then the system mean residence time as discussed in Section 3.1.3. It remains to determine the peak broadening introduced by the detector. Since the detector requires a finite sample to analyze, the output signal cannot be considered as an instantaneous measure across a plane. The detection efficiency is a function of distance between the radioactive source and the face of the detector, the exposed surface area, and the thickness of lead. The efficiency is 100% only when the sample is at the center, perpendicular to the detector. Sternberg (1966) discusses the second moment contributions due to various detector configurations and expresses the behaviour of the detector as an input function. The second moment contribution is given by Equation (3.24) where 'c' is a constant that characterizes the pseudo-flow behaviour or detection efficiency,

$$\sigma^2_{det} = \frac{\tau^2}{c} = \frac{1}{c}\left[\frac{L_{eff}}{V}\right]^2 \tag{3.24}$$

L_{eff}, is the exposed portion of the detector. The value of 'c' for plug flow is 12, 'c' takes a value of 36 for a Gaussian.

In order to calibrate the detector variance it is necessary to determine the effective length and the value of 'c'. This is accomplished by dragging a pseudo-point source of radioactivity in front of the housing at a known velocity. The experimental set-up is illustrated in Figure 2.9. An additional contribution to the variance is introduced by the radioactive source because it is contained in a capsule of finite length (53 mm). This contribution is included in the same way as for the finite injection time and so the mean and total calibration variance are,

$$\mu = \frac{\tau_{cap}}{2} + \frac{L_{eff}}{2V} \tag{3.25}$$

$$\sigma^2 = \frac{\tau^2_{cap}}{12} + \frac{\tau^2_{eff}}{12} = \frac{1}{12}\left[\frac{L_{cap}}{V}\right]^2 + \frac{1}{c}\left[\frac{L_{eff}}{V}\right]^2 \tag{3.26}$$

where,

$$\tau_{cap} = \frac{L_{cap}}{V} \tag{3.27}$$

The first and second moments are calculated from the experimental results using Equation (3.28) and (3.29) respectively,

$$\mu = \left[\frac{\Sigma Ct}{\Sigma C}\right] \qquad (3.28)$$

$$\sigma^2 = \left[\frac{\Sigma Ct^2}{\Sigma C}\right] - \left[\frac{\Sigma Ct}{\Sigma C}\right]^2 \qquad (3.29)$$

The effective length may be calculated from Equation (3.26) having determined the experimental mean from Equation (3.28). The effective length together with the experimental variance, evaluated according to Equation (3.29) are substituted into Equation (3.26) and thus the value of 'c' may be determined.

Measurements were made at three locations to determine the riser RTD: (1) at the base of the riser (Z=0.96 m), (2) at a height of 4.0 m, and (3) in the horizontal section between the riser and cyclone. To maximize the recorded signal but minimize the detector contribution to the variance, the geometry at each of the three locations was different. The signal recorded is proportional to the amount of time the radioactivity spends in front of the detector. In the horizontal section between the riser and cyclone, the gas velocity is four times that at the riser. Hence, longer residence times are preferred and the detector was positioned flush to the wall of the tube. The geometry was somewhat different for the experiments with detectors along the riser. The detector contribution to the variance would be excessive if the detectors were placed flush to the riser wall. Therefore, along the riser, the detectors were pulled back from the wall. The window length was further reduced by encasing the detector in bricks (Figure 2.9). The window length of the shielding positioned at Z=0.96 m was 65 mm and 105 mm at Z=4.0 m.

Figure 3.2 illustrates the response of the pseudo-point source of radioactivity when dragged at a constant velocity in front of the detector housing assembly at Z=0.96 m. The experimental results are compared with the predictions assuming a normal distribution calculated according to Equation (3.30) where μ and σ^2 are the experimental first and second moments.

$$\frac{C}{C_o} = \frac{1}{\sqrt{2\pi\sigma^2}} \exp\left[-(t-\mu)^2/2\sigma^2\right] \tag{3.30}$$

The agreement between the experimental concentration profile and predicted values is quite good confirming that the calibration may be modelled as a Gaussian. In Table 3.1, the first and second moments of housing positioned 0.96 m above the distributor are given together with the calculated window lengths and values for 'c'. Three different capsule velocities were tested to verify the proposed relationship given as Equation (3.24).

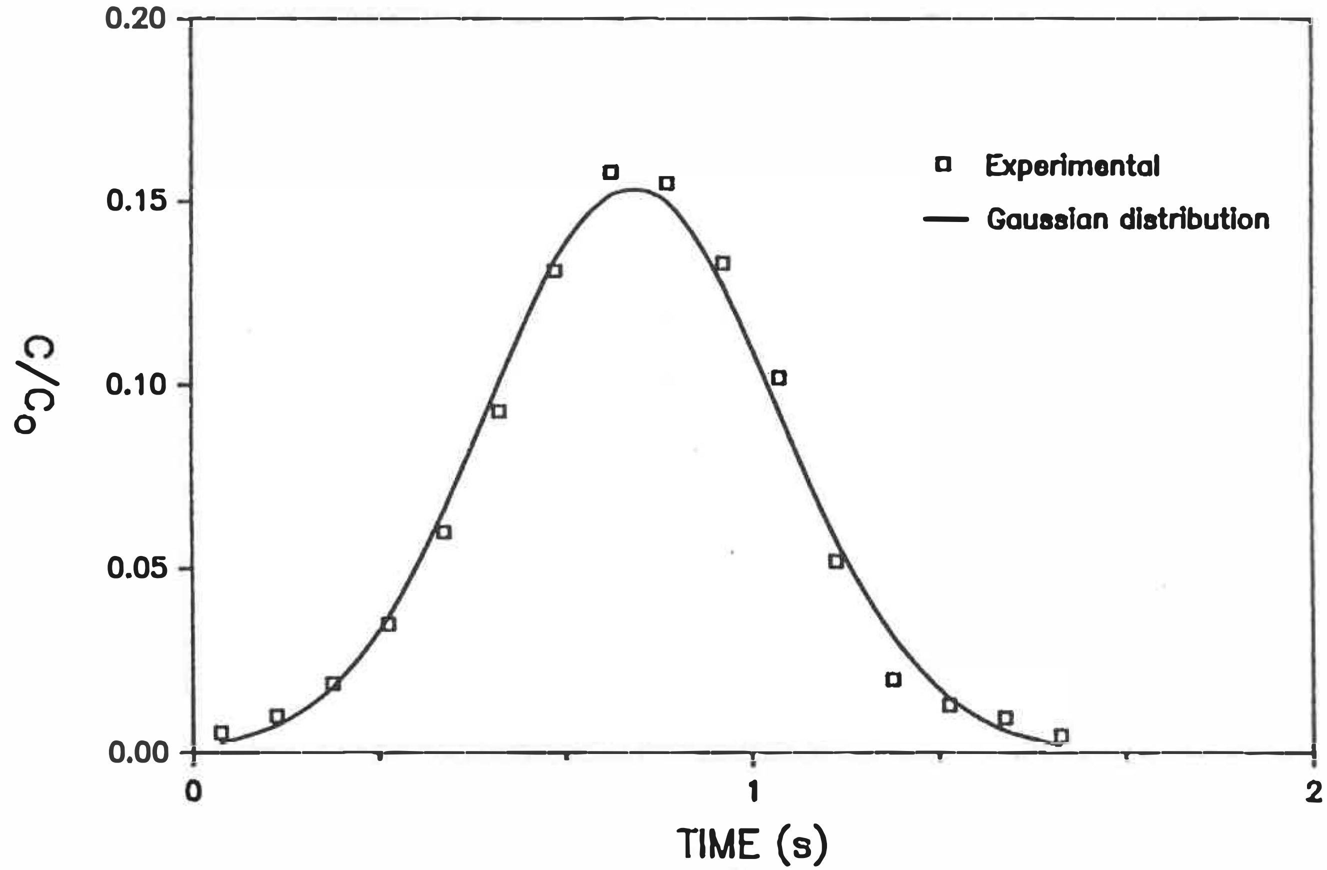

Figure 3.2: Detector Calibration Curve, Z=0.96 m

Table 3.1: Housing I: Variance Contribution Calibration, Z=0.96m

u (mm/s)	μ (s)	σ^2 (s^2)	L_{eff} (mm)	c
52.0	3.22	1.25	281	25
74.4	2.34	0.70	295	24
201.	0.788	0.067	263	28

The detector dispersion is a function of the housing geometry and the distance between the reactor and the detector. The geometry of the detector positioned at a height of 3.99 m is similar but not exactly the same as at the lower housing. The distance between the riser and the face of the detector is approximately the same in the two cases. The lead distribution on top and underneath the detectors is also very similar. The biggest difference between the two detectors is the exposed face which changes the variance considerably. The exposed face of the housing at the top is 40 mm wider than at the bottom. The radioactive sample is 53 mm long and the window is 105 mm wide meaning that the whole sample is exposed to the face over a 52 mm which is much longer than that of the lower detector. The response curve of the detector housing assembly at 3.99 m is compared with a Gaussian distribution, calculated from Equation (3.30) in Figure 3.3. The Gaussian peak is much higher than the

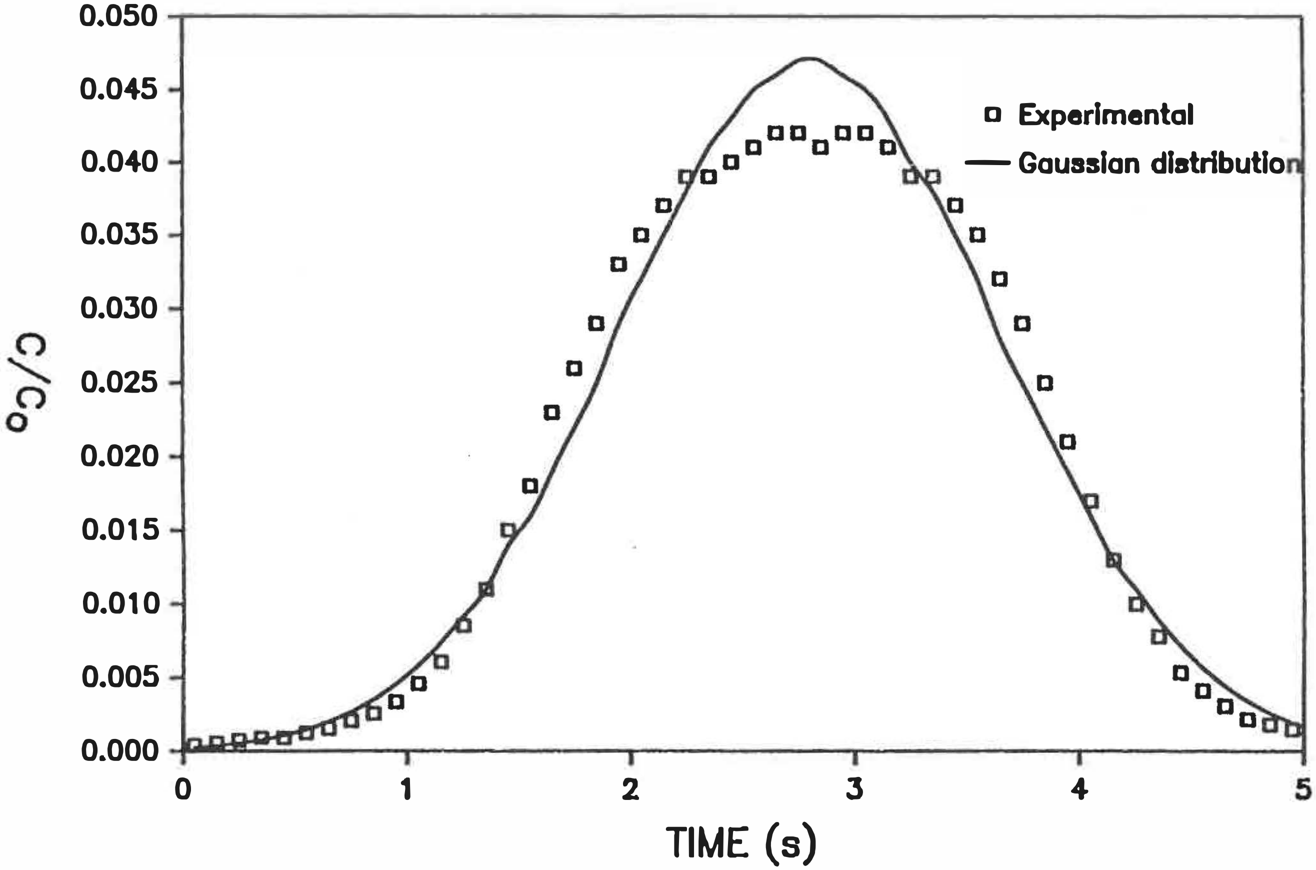

Figure 3.3: Detector Calibration Curve, Z=3.99 m

experimental results; moreover, a plateau is evident at the maximum. This plateau region interpreted as the long exposure time of the whole radioactive sample. To account for this contribution mathematically, Equation (3.26) is modified to read,

$$\sigma^2 = \frac{1}{12}\left[\frac{L_{cap}}{V}\right]^2 + \frac{1}{c}\left[\frac{\Delta L}{V}\right]^2 + \frac{1}{12}\left[\frac{L_p}{V}\right]^2 \qquad (3.31)$$

where, L_p is the plateau length, 51 mm and ΔL is the effective window length minus the plateau length. In Table 3.2, results are presented for the housing dispersion at Z=4.0 m. There is some scatter in the data; however, the magnitude of the variance does not vary appreciably. The average effective window length is 315 mm and 'c' equals 27.5. The lower detector effective window length is assumed to be 280 mm and 25.7 is assumed for the value of 'c'.

Finally, the detector housing in the horizontal section between the riser and cyclone was analyzed. The geometry is somewhat different than that of the detector shielding configuration along the vertical. Equation 3.26 adequately modelled the dispersion characteristics with c=19 and L_{eff}=212 mm.

As indicated in Equation (3.26) the variance decreases with the square of the velocity. Typical gas and solids velocities in the riser are on the order of 4 m/s. Therefore, the detector contribu-

Table 3.2: Housing II: Variance Contribution Calibration, Z=3.99m

u (mm/s)	μ (s)	σ^2 (s^2)	$L_{eff}+L_p$ (mm)	c
74.4	2.79	0.762	362	26
74.4	2.94	0.865	387	26
74.4	2.85	0.733	371	28
74.4	2.67	0.600	344	30

tion to the total variance is small but not negligible. In fact, the detailed study of the detector variance was a result of inconsistencies in turbulent flow dispersion measurements. The contribution to the dispersion is very significant for the standpipe flow measurements in which maximum solids and gas velocities were about 0.1 m/s.

3.2 NUMERICAL APPROACH

The preceding discussion detailed an analytical method to examine the dispersion convection problem. Laplace transforms have been useful in the analysis of flow in packed columns, single phase flow and chromatography. This technique is ideally suited for the study of packed bed flow regime in the standpipe of CFBs over short distances in which neither the gas velocity nor the density change significantly. However, in the riser, both the superficial gas velocity and actual gas velocity vary along the length. At the tee, the solids concentration is greatest as is the pressure. Consequently, the actual gas velocity is a maximum and decreases vertically, whereas the inverse is true for the superficial velocity. At high solids circulation rates and gas velocities, the pressure at the base of the riser greater than at the top; hence, the superficial velocity is not constant. This effect is insignificant in short units. However, it may be considerable in units over 10 m high.

Numerical methods facilitate the analysis of physical systems described by non-linear partial differential equations. The method of Laplace transforms is useful for one-dimensional systems to indicate the behaviour. However, for a detailed study of fluid phases that vary in the spatial and temporal domain inverting the transform to the time domain is very difficult and therefore numerical techniques are employed. The analysis of the solids phase is as complicated as that of the gas phase. The solids are neither distributed uniformly over the cross-section nor over the length. Hence, the velocity is not uniform and the Laplace transformation method to solve the differential equations is not directly applicable.

In this study, a finite difference technique is developed to examine the hydrodynamics of the solids and gas phase and to determine the potential of CFBs as catalytic reactors. The partial oxidation of butane to maleic anhydride is modelled based on published kinetic expressions and the hydrodynamics of the CFB unit. Further detail is given in Chapter 6 concerning the model. To demonstrate the numerical approach, the one-dimensional combined convection-dispersion problem, as given by Equation (3.1), is considered.

Equation (3.1) is discretized in an integral form, similar to the fragmented control volume. The volume element is a cylinder of radius R and length Δz. The discretized form of Equation 3.1 is:

$$R = V\Delta_t C + uX_a\Delta_z C - DX_a\Delta_z(\Delta_z C) = 0 \qquad (3.32)$$

where,

$$V = \pi R^2 \Delta z \qquad (3.33)$$

$$X_a = \pi R^2 \qquad (3.34)$$

$$\Delta_t C = (C_{i+1}^{k+1} - C_i^{k})/\Delta t \qquad (3.35)$$

$$\Delta_z C = (C_i^{k+1} - C_{i-1}^{k})/\Delta z \qquad (3.36)$$

$$\Delta_z(\Delta_z C) = (C_{i+1}^{k+1} + C_{i-1}^{k+1} - 2C_i^{k+1})/\ \Delta z^2 \qquad (3.37)$$

A Newton-Raphson iteration scheme is used to solve the system of equations simultaneously.

$$\Delta X = -J^{-1}R \qquad (3.38)$$

where,

X - Solution vector (3.39)

R - Residual vector $= f_i(C_i) = 0$ (3.40)

J - Jacobian matrix (3.41)

$$= \frac{\partial f_i}{\partial C} = \frac{f_i\ (C_j+\Delta C) - f_i(C_i)}{\Delta C} \tag{3.42}$$

For one dimensional problems, the Jacobian is a tri-diagonal sparse matrix and a penta-diagonal matrix for two dimensional problems. The matrix is inverted using a standard Gaussian elimination technique as given by Aziz and Settari (1976).

The solution procedure is as follows: Time is advanced one step and the residual vector, Equation (3.32), is calculated. The solution vector is computed by multiplying the inverted Jacobian matrix by the residual vector. Finally, the primary variable, C_i, is updated according to:

$$C_i^{l+1} = C_i^{l} + \Delta X_i \tag{3.43}$$

where, l is the iteration increment. This procedure is repeated until the following convergence criteria is met:

$$\Delta x_j < 10^{-6} \tag{3.44}$$

One of the major limitations of finite difference techniques is the error introduced by numerical dispersion, also known as false diffusion. Patankar (1980) discusses at length false diffusion and suggests that it is a multidimensional phenomenon and that it is not evident in steady one-dimensional situations. However, he does admit the existence of numerical dispersion for unsteady one-dimensional problems. Results from the numerical simulation are compared with the exact solution in Figures 3.4 and 3.5, for Peclet numbers of 20 and 200. At low Peclet numbers many grid blocks are not required to optimize the numerical solution. With only 40 grid blocks and 1000 time steps the results of the simulation approximate the analytical solution reasonably well. However, at higher Pe numbers a large number of grid blocks and time steps are required. The accuracy of the numerical solution is dependent upon the number of time steps and grid blocks employed. Since the measured Pe number was always less than 200 about 400 grid blocks and 1000 time steps were used for most calculations.

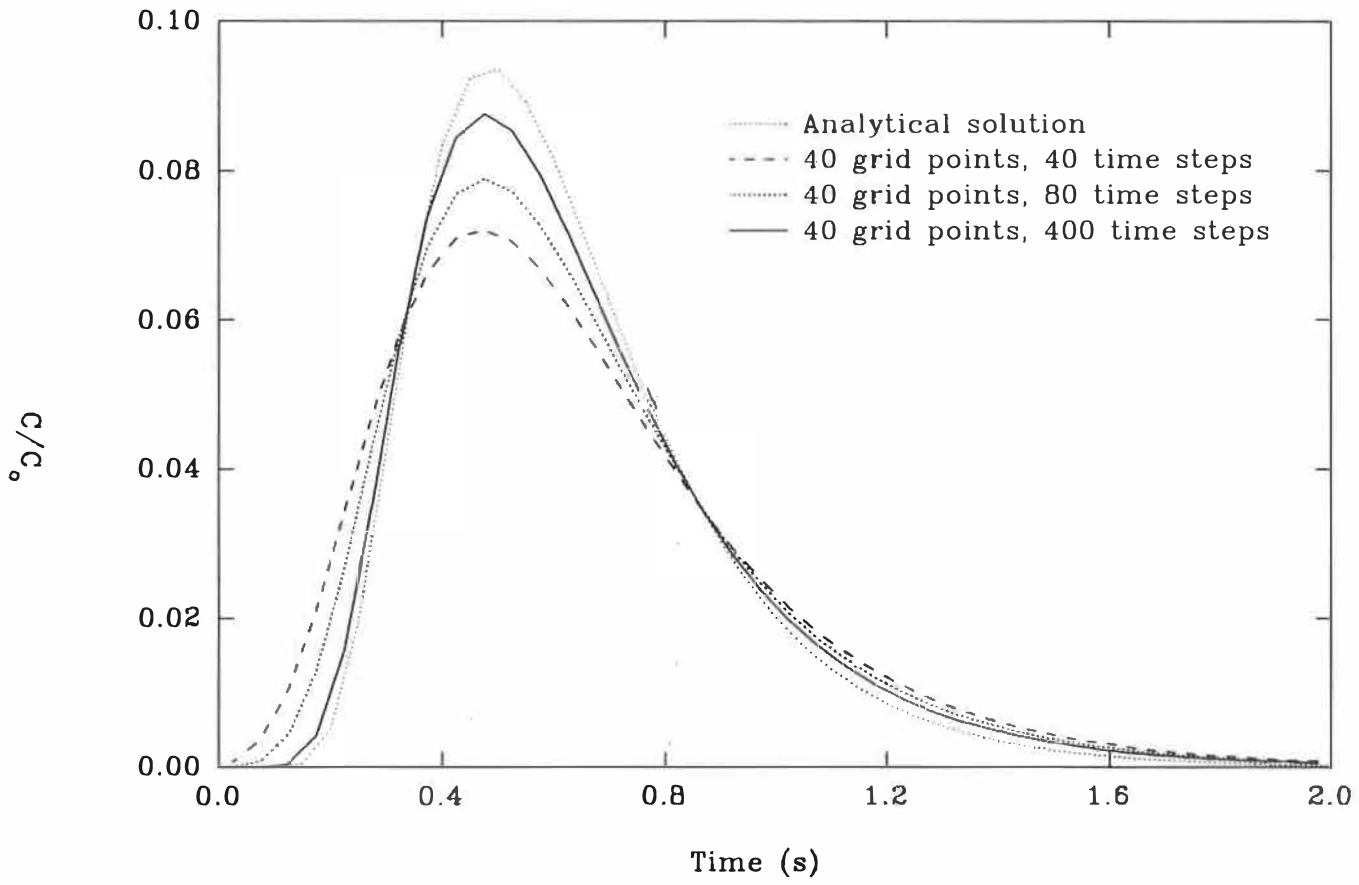

Figure 3.4: Analytical RTD compared with numerical RTD, Pe=20

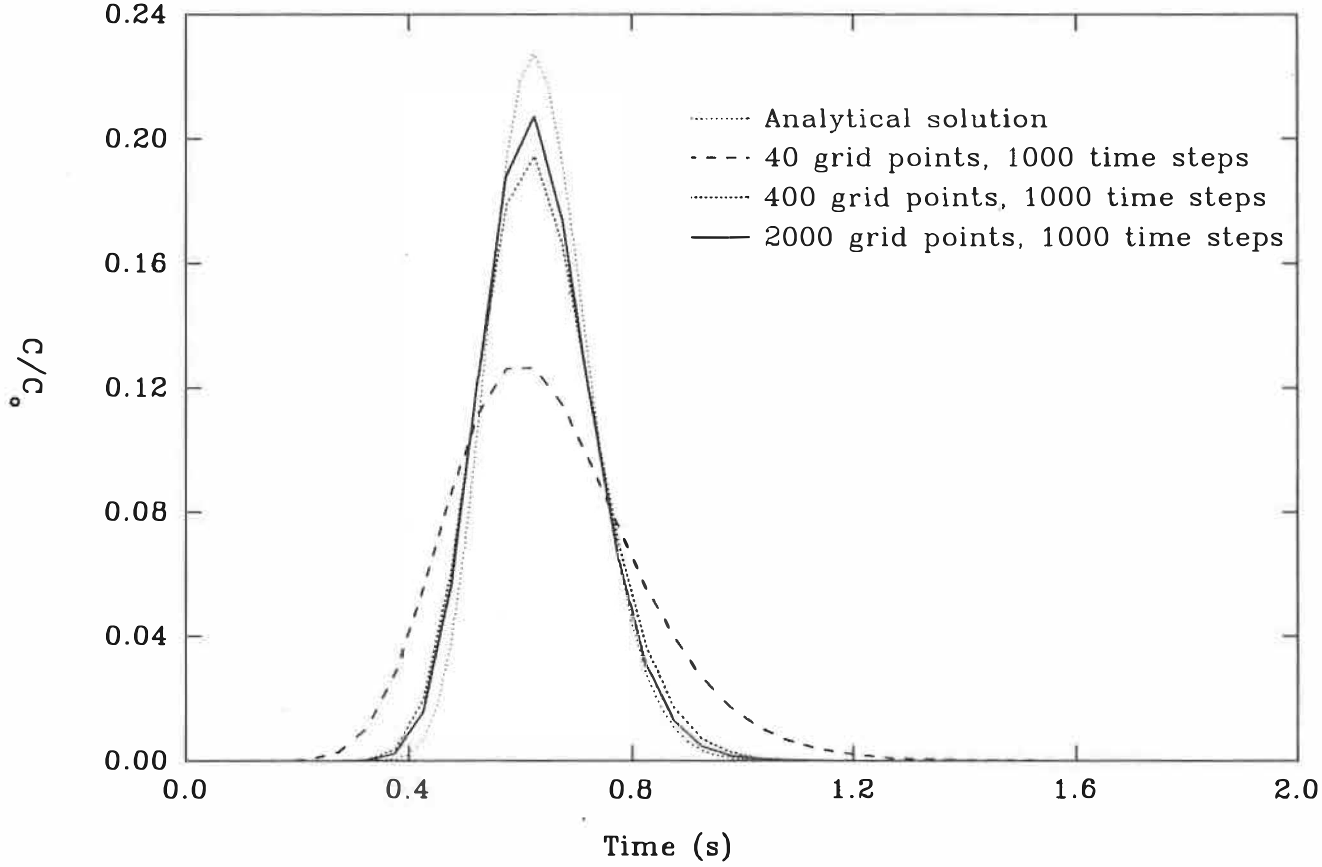

Figure 3.5: Analytical RTD compared with numerical RTD, Pe=200

4. GENERAL OPERATION AND SOLIDS HOLD-UP

4.1 VISUAL OBSERVATIONS

Transparent pyrex tubes are installed to permit visual observation of the flow patterns in the CFB system. Five regions were studied including: the tee, solids entry point just above the distributor; the riser, just below the elbow at the exit of the riser; the horizontal section between the riser and cyclone; the standpipe, 1.5 m below the bottom of the hopper; and the L-valve, the horizontal section between the standpipe and riser. The observations were qualitative in nature except in the standpipe where particle velocity measurements were made to determine the solids circulation rate.

4.1.1 Tee region

The solids entry point at the tee and the lower part of the riser are described as regions of considerable turbulence. At high solids circulation rates it is uncertain as to the nature of the true flow regime. The flow pattern is difficult to ascertain visually because the solids concentration is so high that quantitative observations are impossible. Experimental studies (Brereton, 1987; Rhodes and Geldart, 1986), using various types of intrusive probes, indicate a radial concentration gradient towards the wall. This gradient has been characterized using a core annular model, with a lean solids region at the core and a dense annular ring, and a cluster model in which solids are concentrated in packets or streamers which are distributed throughout the cross-section. (Yerushalmi et al., 1978; Youchou and Kwauk, 1980; Weinstein et al., 1984).

The solids flow pattern at a riser velocity of 4.5 m/s is illustrated in Figure 4.1 for a number of mass fluxes. At low circulation rates, the particles accelerate as soon as they enter the tee section. As the solids rate is increased, the particles promenade across the radius. That is, for each increase in the solids rate the penetration of solids towards the center increases before eventually accelerating in the vertical direction. An "inverted pseudo bridge" extends across the radius at a mass flux of 6.5 kg/m^{2}s and secondary flow patterns, in which particles descend along the wall, occur at higher circulation rates. Finally, at mass fluxes characteristic of normal operating conditions the solids phase is so dense that flow patterns are indistinguishable. Strong fluctuations, resembling slugs, are apparent and at times the region is completely emptied of solids by the gas. The empty space is quickly filled by solids from the L-valve.

4.1.2 Riser

In the vertical tube just below the exit of the riser, two flow patterns predominate. At low circulation rates, the solids are

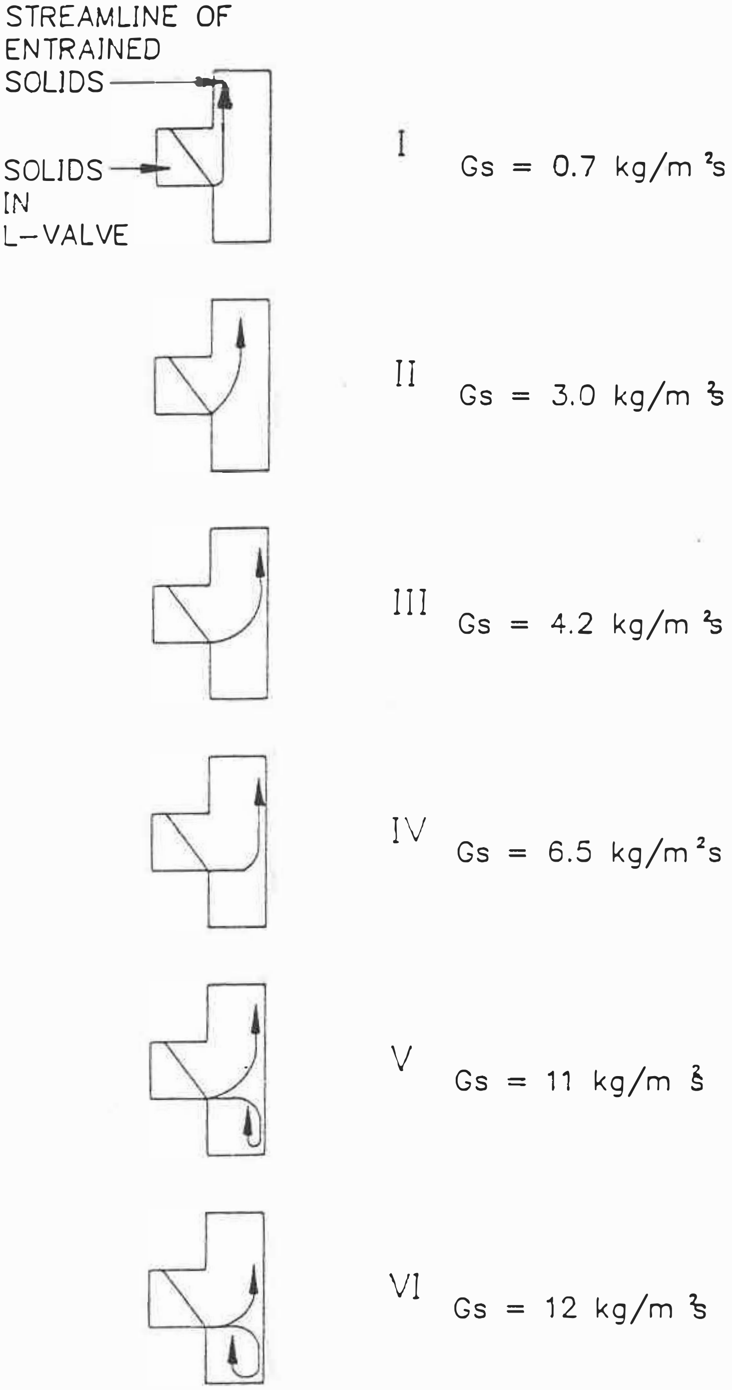

Figure 4.1: Solids Flow Pattern in the Tee Section, U_g= 4.5 m/s

homogeneously distributed throughout the pipe cross-section, i.e. a fully suspended homogeneous flow regime. Neither are there discernable clusters of particles nor is there a dense annular region at the pipe wall. At higher solids circulation rates a dense wall region is apparent. However, this annulus of solids does not form a continuous ring; it is more like a cluster. Furthermore, these clusters do not uniquely flow in the downward direction. The behavior is sporadic; at times the clusters are suspended against the wall for up to a second before dispersing and falling down along the wall or moving up with the gas.

4.1.3 Horizontal pipe between riser and cyclone

As in the vertical section, a homogeneously fully suspended flow pattern is observed in the horizontal section between the riser and the cyclone at low circulation rates. Various flow patterns are identifiable at higher solids fluxes; a degenerate homogeneous suspension, as described by Wen and Simmons (1959), is apparent 250 mm downstream of the elbow. Concentrated packets or strands of solids slide along the bottom of the tube. At the same operating conditions, however, the flow at the front of the tube is neither homogeneously suspended nor are the particles uniquely concentrated near the bottom in strands. This flow pattern designated as a "degenerate suspension" by Patience et al. (1990) is characterized by elongated clusters that deflect off the top and sides of the tube as well as sliding along the bottom.

4.1.4 Standpipe

The standpipe is generally operated in the packed bed and the transitional packed bed flow regime (Leung and Jones, 1978). At low circulation rates (G_s<20 kg/m^2s) the solids flow smoothly down the pipe. At higher rates, the particle velocity is irregular. The "slip-stick" flow pattern develops in which periodic interruption of the solids movement is followed by high particle velocities. The term "slip-stick" is misleading because the solids do not stick to the pipe wall then slip. In fact, the oscillatory nature of the velocity of the bed originates in the riser. When the tee is packed with solids, the force developed in the standpipe is not great enough to push the particles into the riser, the solids stop moving and thus appear to stick. The pressure builds up at the elbow until a sufficient amount of solids is entrained in the riser creating space at the tee. At sufficiently high aeration rates pseudo bridges develop in the standpipe as described by Ginestra et al. (1980).

4.1.5 L-valve

The flow pattern in the L-valve is known as slug flow in which the gas flows in pockets along the top of the pipe, something like a moving bed with ripples. Govier and Aziz (1977) more eloquently describe this flow pattern as a, "stationary bed with saltation and asymmetric suspension". The solids are transported by the air at the top of the pipe. At very low rates the lowermost particles are stationary. As the aeration rate is increased these particles begin to move. Their velocity is always less than that of the uppermost solids. The frequency of the slugs increases at higher aeration rates as does the bed velocity.

4.2 SOLIDS METERING

The solids circulation rate is an important operating parameter of CFB systems. It is the basis of most correlations and is critical to hydrodynamic modelling of both the riser and standpipe. However, the techniques used to measure the mass flux are inadequate. Burkell et al. (1988) tested a number of methods and rated their characteristics including the sensitivity, versatility and whether or not they were amenable to large scale systems operating at elevated temperatures. They concluded that none of the techniques reviewed was completely satisfactory. Therefore, in the present investigation a method was developed to measure the solids circulation rate that satisfied the criteria as set out by Burkell et al. (1988).

Previous techniques are limited to measurements in the recirculation leg, either in the standpipe or in the storage hopper. Unfortunately, the hydrodynamics in these regions are difficult to characterize. For example, in the standpipe the gas flow may be either co-current or counter-current to the solids flow. At high aeration rates pseudo-bridges may form creating an unstable flow regime. Other methods used to date include: diverting the flow and measuring the trapped solids and measuring the accumulated solids on a butterfly valve just below the cyclone. These methods have a number of basic limitations as discussed by Burkell et al. (1988). Closing the valves perturbs the system and will affect the operation of the equipment, the methods are not continuous and the use of butterfly valves at high temperature is doubtful.

4.2.1 Time-of-Descent Method

The simplest solids flux measurement technique is timing the descent of particles along a transparent tube in the standpipe. The measured velocity is multiplied by the bulk density to give the mass flux. The problem with this technique is that the particle velocity at the wall may not represent the mean velocity. Phenomena such as curtaining (Judd and Rowe, 1976) can mask the actual velocity. Furthermore, it is necessary to assume plug flow of the solids phase and a value for the void fraction. Burkell et al. (1988) use ρ_{mf} for the bulk density. Knowlton and Hirsan (1978) propose a linear variation of the porosity with the slip velocity. Zhang et al. (1989) present data suggesting that the porosity at minimum fluidization is appropriate for high slip velocities but their results are limited to standpipes restricted by an orifice at the bottom.

It is necessary to examine the bulk solids movement to evaluate the applicability of particle wall velocities as a mass flux measuring technique. Four different experiments were used to establish the relationship between the bulk velocity and wall velocity. The first series of tests involved flow through an orifice at the bottom of the standpipe. The mass flow is determined by opening a gate valve mounted on a pipe 38.1 mm in diameter threaded into the center of the 82.8 mm standpipe and weighing the solids collected in a receiving bin. Particle velocity measurements are made in the pyrex tube simultaneously, by timing their descent along the wall. Small samples of sand are collected periodically to determine the change in solids flux with time. The mass flux, G_s, remained constant at 60.6 ±2.8 kg/m^2s from the time the valve is opened until the solids are completely drained. The sand velocity, U_p, was 0.0253 ±0.0011 m/s. Dividing G_s by U_p gives a bulk density of 2395 kg/m^3 compared with a particle density of 2630 kg/m^3! Clearly, the particle velocity at the wall is not representative of the mean velocity for this experiment.

When the total inventory of solids is allowed to drain, the sand-air interface is observable in the pyrex tube. The solids interfacial velocity was measured to be 0.0367 m/s which gives a bulk density of 1651 kg/m^3 and a void fraction of 0.372. The interface was not flat as expected for plug flow but was concave indicating the existence of a velocity gradient or at least that curtaining was present.

The flow pattern in a standpipe restricted by an orifice is different than that with an L-valve. Therefore, in the second series of experiments, instead of allowing the solids to drain at the bottom of the standpipe, aeration air, introduced at the elbow, forces the solids through the L-valve. The solids flow from the distributor into the windbox and are collected and weighed at the base of the riser. Measurements were limited to low mass rates because at high rates the solids plug up in the tee-section. The particle wall velocity was 0.0217 ±0.0010 m/s compared with an interfacial velocity of 0.0299 ±0.0021 m/s. In addition, the solids flux based on the weighed sand was greater than that calculated based on the wall velocity. The true solids mean velocity is greater than that predicted by measuring the wall velocity, implying a velocity gradient and/or curtaining.

The solids movement in the standpipe was examined under normal operating conditions in the third set of experiments. The results described above suggest a non-uniform particle velocity distribution but the data are only qualitative in nature and does not apply to typical circulating fluidized bed operating conditions. The third set of tests involved charging the CFB with a known amount of sand then injecting a radioactive tracer into the reactor and measuring the re-circulation time. Tracer is introduced at the bottom of the column and detected at the top. The circulation time is calculated based on the difference of the first moments of the normalized density function.

The drawback of this method is that dead zones exist and bypassing is possible,. particularly in the hopper. Mass rates are based on dividing the total mass of catalyst in the CFB by the measured time it takes to circulate through the reactor once. Dead zones and bypassing result in inflated circulation rates since the true mass of catalyst circulated is less than the total. To minimize this effect, the solids inventory was kept at a minimum. The level of the sand was maintained just below the cone section of the hopper to eliminate the potential for bypassing in this region. The dead zones in the L-valve and at the elbow remains. The magnitude of the dead zone increases with a decreasing aeration rate; therefore, the error is greatest at low solids fluxes. The maximum error could be as high as 20 %.

Predictions of the solids circulation rate based on the time-of-descent method and the radioactive tracer measurements are presented in Table 4.1. Figure 4.2 illustrates a typical normalized density function. The first peak is narrow and high and is a result of the riser dispersion. The successive peaks broaden with time because of the additional dispersion in the standpipe and L-valve.

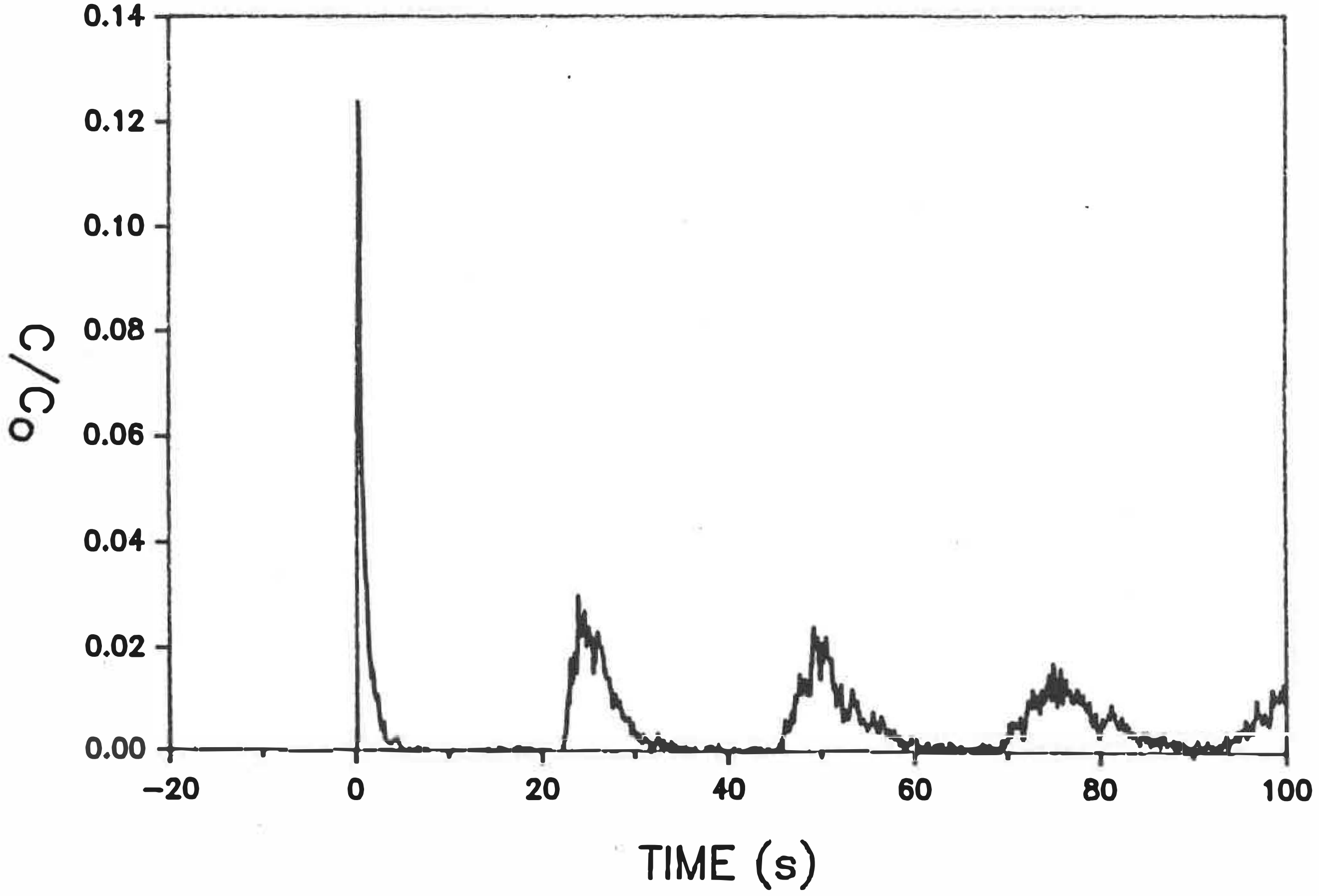

Figure 4.2: Solids Circulation Rate Calibration

Table 4.1: Comparison of Mass Flux Predictions

V_p (m/s)	$G_{s,2}$ (kg/m^{2}s)	$G_{s,1}$ (kg/m^{2}s)
0.0628 ±0.0034	88.3	180
0.0448 ±0.0016	63.0	123
0.0298 ±0.0008	41.9	85.8

The mass flux, based on the tracer study, is calculated from Equation 4.1,

$$G_{s,1} = \frac{M}{(\mu_2 - \mu_1)X_a} \qquad (4.1)$$

where, X_a is the cross-sectional area of the riser, μ_1 and μ_2 refer to the means of the first and second peaks of the RTD curve and M is 24 kg. The mass flux using the particle velocity measurements is

$$G_{s,2} = V_p \rho_p (1-\epsilon) X_{a,pyrex}/X_a \qquad (4.2)$$

A constant void fraction of 0.38 is assumed for calculation purposes. This value is an average between the minimum fluidization void fraction (ϵ_{mf}=0.41) and a vibrated bed (ϵ_{vb}=0.34). Since the diameter of the pyrex tube is not equal to the riser diameter, G_s must be multiplied by the ratio of the areas to correct for the difference. The pyrex tube is 0.0764 m in diameter and the stainless steel is 0.0828 m in diameter.

Clearly, the solids circulation rate predicted from the radioactive tracer analysis is significantly greater than that of the time-of-descent method. The difference may not be accounted for by the dead mass of sand in the L-valve which is at maximum 3 kg (based on the volume of the L-valve). The difference between the mass flux predictions would even be greater if the minimum fluidization void fraction is used as suggested by Burkell et al. (1988).

To quantify the velocity profile a fourth set of experiments was undertaken in which radioactive sand is injected into the hopper and detected at two points downstream in the standpipe. The difference between the first moments of the normalized density function gives the transit time between the two points and thus velocity. Particle wall velocities are measured at the same time and compared with the tracer velocity.

A typical RTD curve is illustrated in Figure 4.3. The first peak corresponds to the response of the detector 2.66 m above the bottom of the standpipe. The second peak is the response of the detector 1.78 m underneath the first. The geometry of the lead shielding is not identical. Therefore, the peak widths may not be directly compared without including the contribution to the dispersion of the housing. However, quantitatively it is evident that the dispersion along the 1.78 m length is minimal indicating that the solids velo-

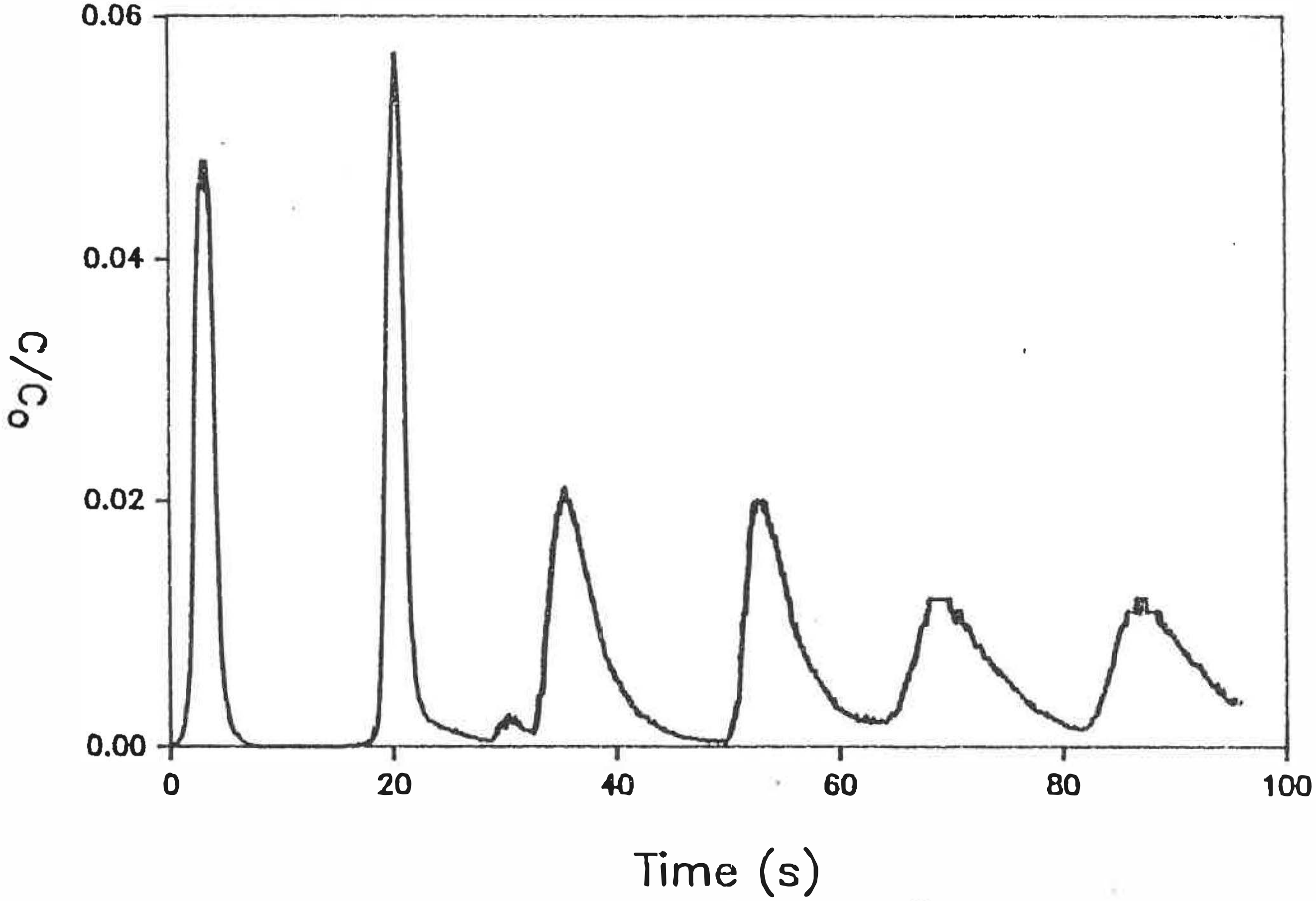

Figure 4.3: Concentration Variation of Solids Tracer in the Standpipe

city profile is flat. A tail is apparent after the second peak which may be interpreted as a result of a velocity gradient, i.e. curtaining at the wall. The bump after the tailing is a result of the radioactive sand entrained by the gas in the riser. The detector was inadequately shielded at the back.

The bulk solids velocity calculated based on the radioactive tracer study is compared with particle wall velocity measurements in Figure 4.4. The time-of-descent method clearly underestimates the bulk velocity, hence, mass flux.

The experimental mass flux, G_s, varies linearly with the particle wall velocity as shown in Figure 4.5. The data have been correlated by the following equation assuming an ϵ value of 0.38:

$$G_s = 2900 V_p \tag{4.3}$$

The time-of-descent method is a simple method to determine the mass flux in small experimental units at ambient conditions once the particle wall velocity has been calibrated. This method is not practical for large scale equipment operating at elevated temperatures and pressures. Therefore, a second, more versatile, method was developed and entails the measurement of the pressure drop in the horizontal section between the riser and cyclone. The pressure drop in this region is sensitive to both the gas flow rate and the solids mass flux. A number of different geometries were tested, including a

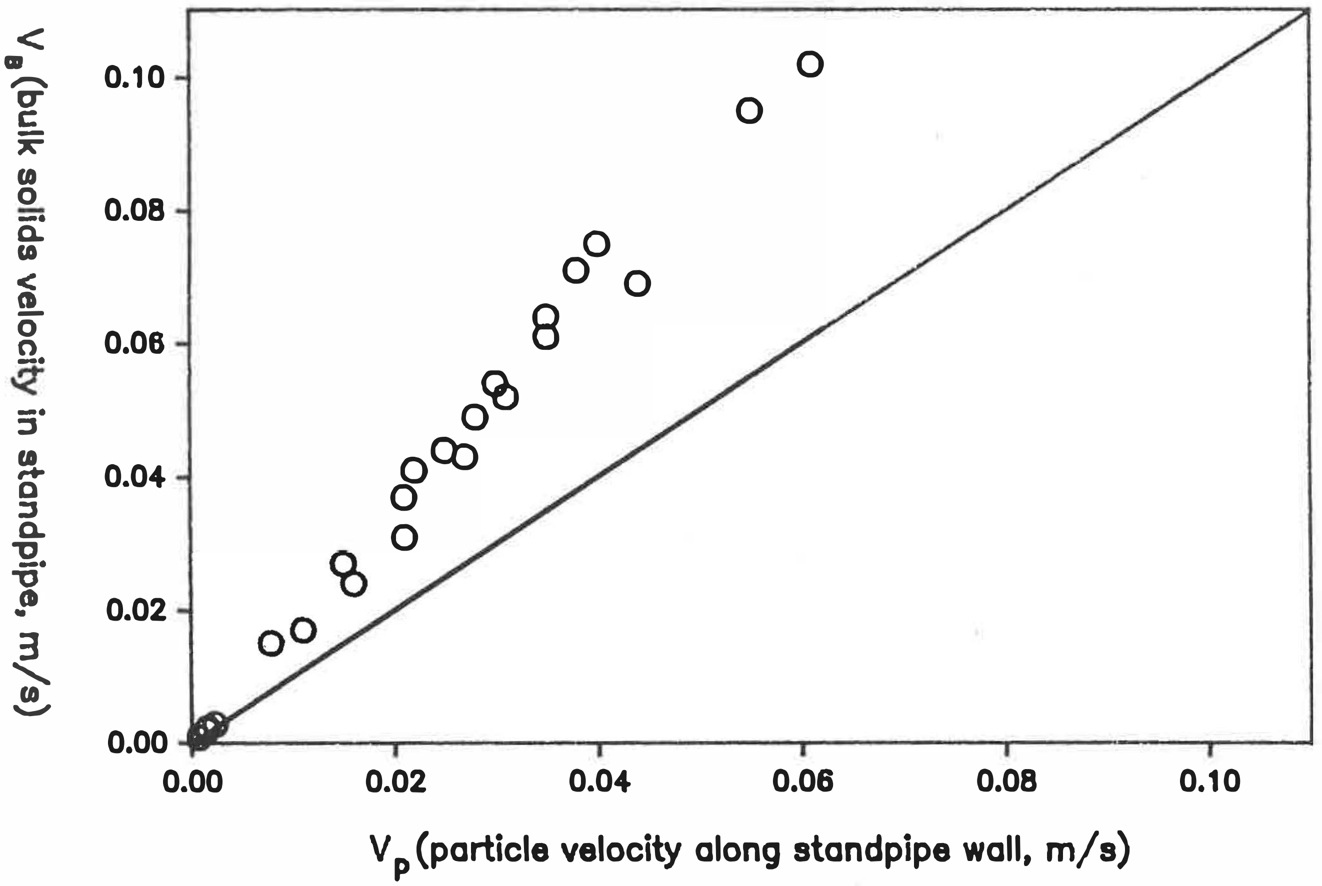

Figure 4.4: Standpipe bulk solids velocity compared with wall velocity

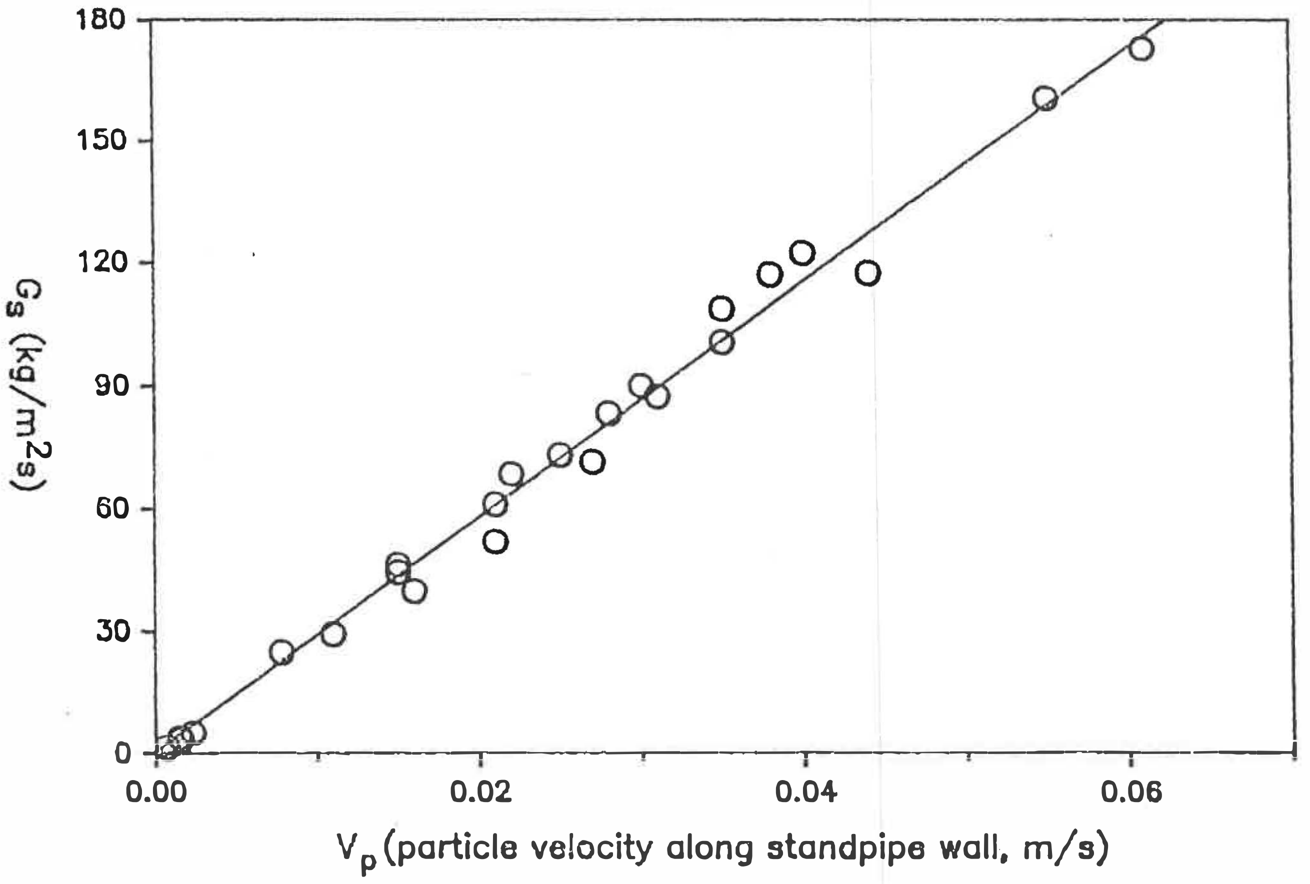

Figure 4.5: Mass flux compared with wall velocity, ϵ assumed equal to 0.38

smooth pyrex tube 38 mm in diameter, a stainless steel tube 41 mm in diameter and a flexible metal hose with an internal helical corrugation 41 mm in diameter. Pressure taps were mounted flush to the pipe wall. The first pressure tap was positioned 100 mm from the exit of the elbow and the second 150 mm further downstream. Particle velocity measurements in the standpipe were made at the same time as the pressure readings and Equation 4.3 was used to calculate the mass flux.

The following range of gas velocities and solid circulation fluxes in the test section were studied:

$$14 < V_{gh} < 32 \text{ m/s} \qquad 0 < G_{sh} < 500 \text{ kg/m}^2\text{s} \tag{4.4}$$

The corresponding conditions in the riser were :

$$3.5 < V_{gv} < 8 \text{ m/s} \qquad 0 < G_{sv} < 125 \text{ kg/m}^2\text{s} \tag{4.5}$$

Figure 4.6 illustrates the variation of the pressure drop in the pyrex tube as a function of the solids flow rate at different superficial gas velocities. The relationship between the pressure drop and solids flow rate is linear.

For fully suspended flow in a horizontal pipe the pressure drop has been expressed as the sum of the frictional pressure drop due to the gas and solids and an acceleration pressure drop of the gas and solids (Govier and Aziz, 1977).

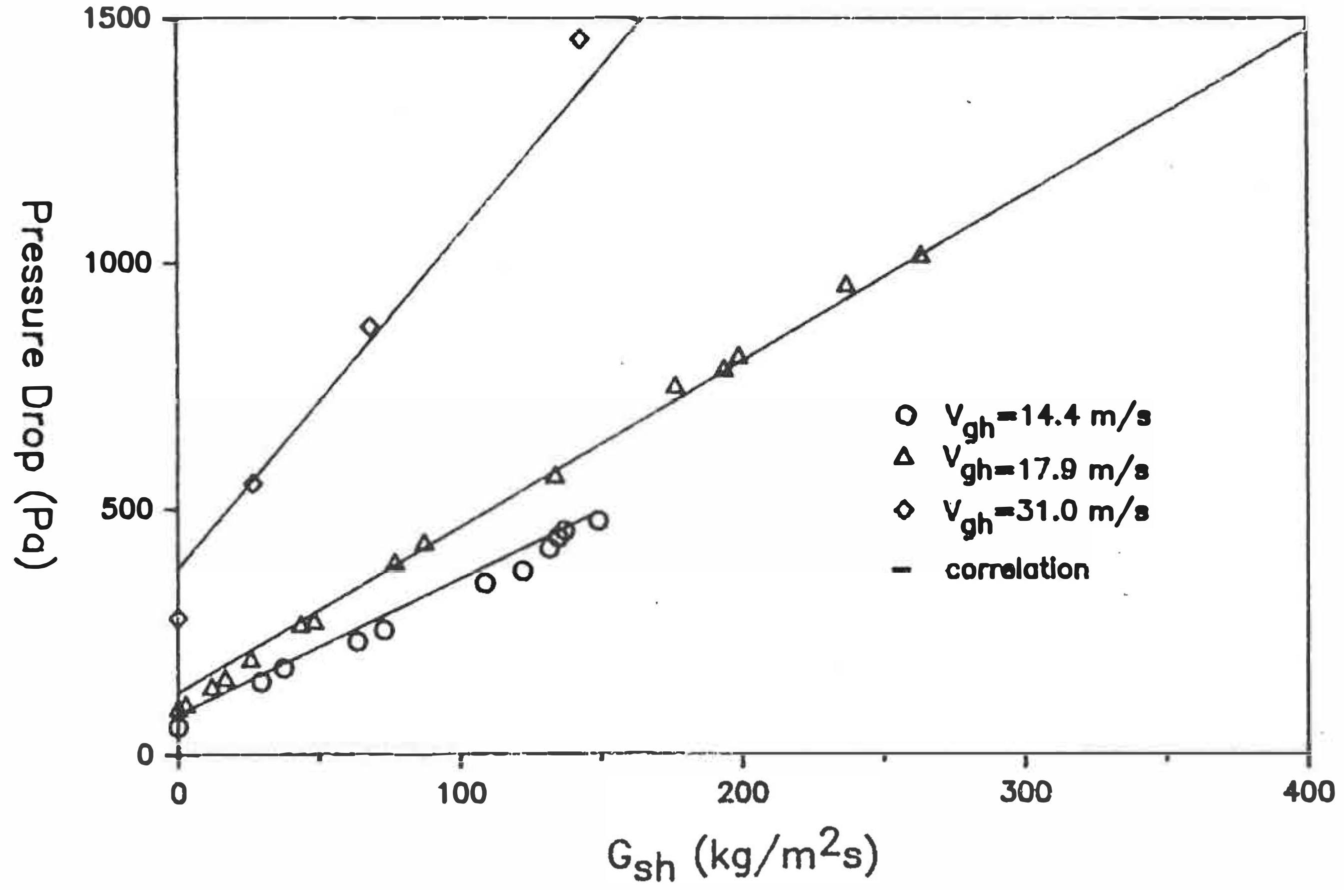

Figure 4.6: Pressure drop compared with mass flux

$$\Delta P = 2\rho_g(f_g+f_s)(L/D)V_g^2 + \Delta P_{KEs} + \Delta P_{KEg} \qquad (4.6)$$

Acceleration pressure drop accounts for kinetic energy effects and can be expressed by:

$$\Delta P_{KEi} = G_i(V_{i,2}-V_{i,1}) \quad \text{with } i = s \text{ or } g \qquad (4.7)$$

The initial sections of horizontal conveying pipes in which acceleration effects are significant have not been studied extensively. Kmiec and Leschonski (1987) discussed a number of investigations of vertical pipes. Rose and Duckworth (1969) proposed an expression to describe the additional pressure drop due to acceleration in horizontal systems. Unfortunately, this expression is uniquely applicable to the total developing region. In the present study, the pressure drop is measured over one percent of the developing length. Moreover, the test section is extremely close to the entrance in comparison to the 13 m developing length necessary to fully accelerate the particles. Therefore, it is assumed that the particle velocity at the second pressure tap is small in comparison to the fully developed particle velocity and that the difference $(V_{s,2}-V_{s,1})$ is constant. The resulting expression for the acceleration pressure drop of the solid phase is:

$$\Delta P_{KEs} = aG_{sh}L \qquad (4.8)$$

This linear variation is in agreement with that proposed previously by Rose and Duckworth (1969). Acceleration effects of the gas were assumed to be negligible. In order to account for the observed linear variation of the pressure drop with mass flux and to be consistent with the previous theoretical analysis, a relation of the following form is suggested:

$$\Delta P = aG_{sh}L + 2\rho(L/D)bG_{sh}V_{gh}^2 + 2\rho f_g(L/D)V_{gh}^2 \tag{4.9}$$

where the coefficients may be interpreted as:

$$aL = (V_{s,2}-V_{s,1}) \tag{4.10}$$

$$b\,G_{sh} = f_s \tag{4.11}$$

In Table 4.2, a summary of the parameters obtained from a least squares non-linear regression analysis (Marquardt method, Press et al., 1986) of the experimental data for the different geometries is presented. The agreement between the calculated pressure drop and the experimental data is excellent, as illustrated in Figures 4.6 and 4.7. The values of the coefficient "a" correspond to the acceleration of a particle from 0 to about 3 m/s. This value is reasonable in comparison with the fully developed particle velocity calculated to vary from 12 to 24 m/s (Klinzing, 1981).

The value of f_s is seen to increase as the mass flux increases as reported in previous investigations (Jones et al., 1967; Dogin and Lebdev, 1962; Soo, 1982). Jones et al. (1967) suggest that the solids friction factor term, f_s, depends on the ratio of the mass flow rate of solids to gas as well as the geometry of the particles.

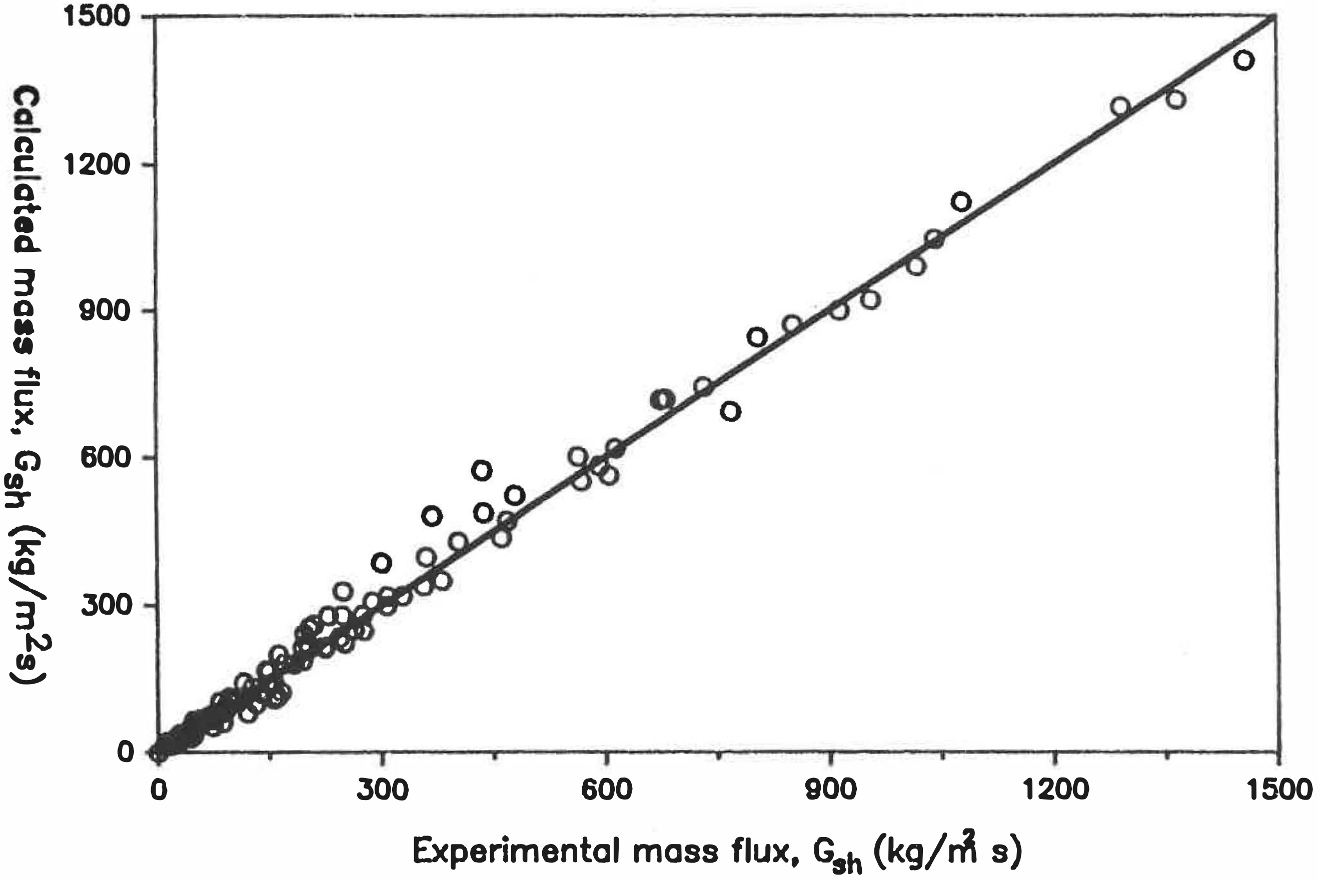

Figure 4.7: Experimental mass flux compared with calculated mass flux

Table 4.2: Fitted Parameters for the Pressure Drop Correlation

Tube	L (mm)	a (s^{-1})	b ($m^2 s/kg$)
s.s., D=41 mm f_g=.0055	52	8.4	0.00040
s.s., D=41 mm f_g=.0055	168	7.6	0.00042
pyrex, D=38 mm f_g=.0055	72	5.5	0.00034
pyrex, D=38 mm f_g=.0055	153	7.6	0.00046
hose, D=41 mm f_g=.039	173	9.7	0.00054

Dogin and Lebedev (1962) considered a larger number of parameters to correlate the solids friction factor and proposed a linear variation of f_s with the G_{sh}, as obtained in the present study. For a solid mass flux, G_{sh}, of 180 kg/m^{2}s the value of f_s, calculated with Equation (4.11), is equal to 0.07 which is an order of magnitude less than the modified correlation of Dogin and Lebedev (Soo, 1982) but an order of magnitude greater than that predicted by either Rose and Duckworth (1969) or Jones et al. (1967). The calculated f_g for the corrugated section was determined to be four times greater than that of a rough tube and increases with temperature.

The solids mass flux can be determined from Equations (4.13-15) given the pressure drop and gas velocity. A comparison of the calculated and experimental solids mass flux is illustrated in Figure 4.7 for the case of a pyrex tube. The agreement between predicted and experimental results is quite good.

The correlations presented are limited to the geometry studied and therefore are not suitable for scale-up purposes. However, this technique may be applied to industrial equipment if adequately calibrated.

4.3 L-VALVE AND STANDPIPE ANALYSIS

Solids downflow in moving beds is common practice in the metallurgical, chemical and petroleum industries and is critical for the smooth operation of CFB systems. Non-mechanical valves are often used to control the particulate flow rate. L-valves belong to the general class of non-mechanical valves that include J-valves, V-valves etc. The L-valve standpipe assembly consists of a vertical pipe, in which the solids are conveyed in the downward direction against a pressure gradient and a horizontal section at the base of the standpipe. Aeration gas in the downcomer controls the solids rate. Despite their successful application to such processes as SASOL, hydrocarbon catalytic cracking, coal gasification and liquefaction, L-valve design is largely based upon rules of thumb and operating experience (Leung and Jones, 1978; Workshop on standpipe systems, Fluidization VI, Banff, 1989). Moreover, in most experimental studies, standpipes are generally considered in isolation without consideration to the process downstream. Stability analysis, theoretical and experimental (Leung and Jones, 1978; Chen et al., 1984) have been limited to standpipes with an orifice at the base. Little published work is available concerning L-valves, and no studies have determined the effect of CFB operating conditions on the L-valve and stability.

L-valve operation in CFB systems is complicated because aeration air, introduced at the elbow, may either go up the standpipe counter current to the solids or it may go down. In the downward direction, the gas may have a velocity greater than or less than the solids. The gas and solids are assumed to be in plug flow and wall friction is neglected. Slip velocities are generally not measured but calculated based on the pressure drop and an assumed voidage profile (Knowlton and Hirsan, 1978). In situ void fraction and gas velocity measurements are difficult to make. The analysis is further complicated due to the compressibility of the gas. For long standpipes the pressure at the bottom may be significantly greater than at the top. Consequently, the gas density is greater at the L-valve. Therefore, to satisfy gas continuity constraints, the gas velocity at the top must be greater than that at the bottom.

The flow phenomena around the bend and in the L-valve has not been treated in the open literature. Most work concerns modelling standpipe flow with a constriction, such as an orifice, at the base. Data concerning the horizontal flow of gas-solid mixtures is generally limited to suspensions (Govier and Aziz, 1977). Moreover, Govier and Aziz (1977) suggest that the lack of proven methods to estimate flow rates in stationary and moving beds is not serious from a practical point of view. They assert that this mode of transport is rarely employed. In this study, both the flow of the gas-solid mixture in the vertical standpipe and horizontal L-valve are examined. In particular, the effects of two parameters are considered, the gas velocity in the riser, and the solids circulation rate and hence solids hold-up in the tee. The following measurements are made: (1) the pressure drop in the standpipe 2.15 m from the bottom; (2) the pressure drop in the L-valve; (3) the gas velocity using radioactive argon as a tracer; (4) the particle velocity using radioactive tracers.

4.3.1 Standpipe Operation

Knowlton and Hirsan (1978) studied various parameters that affect L-valve operation, including: changing the aeration tap location, standpipe diameter, horizontal length and diameter, and particle density. However, further study is required concerning the stability of the standpipe flow, effects of aeration, particle size distribution, temperature and pressure, as suggested in the Workshop on standpipes at the International Conference on Fluidization in Banff (1989).

Knowlton (1989) discusses the basic operating principles of non-mechanical valves and recycle devices. He suggests that the pressure drop in the standpipe adjusts to balance the pressure drop developed in the L-valve, riser and piping. The minimum standpipe length is determined by dividing the pressure drop of the independent part of the loop and dividing by $\rho_{mf}g$ with a safety factor of 1.5-2 times L_{min}. In addition, a minimum L-valve length 1.5-2 times the length to which the solids due their angle of repose is proposed.

The pressure drop in the standpipe and L-valve were measured to determine the effect of changing the gas riser velocity. Three riser gas velocities were studied: 4 m/s, 6 m/s and 8 m/s. In Figure 4.8, the variation of the aeration rate at the elbow is plotted as a function of the mass flux. It is evident that the riser gas velocity does not affect the aeration requirements for a given solids mass flux. However, at 4 m/s the maximum circulation rate attained is significantly less than that at 6 m/s or 8 m/s. This observation is confirmed in Figure 4.9 in which the developed pressure drop in the standpipe is plotted against the solids circulation rate. A maximum pressure drop of approximately 6 kPa/m is realized before the fluctuations in the standpipe become excessive (i.e. unstable). Before reaching a gradient of 6 kPa/m the pressure fluctuations are minor in

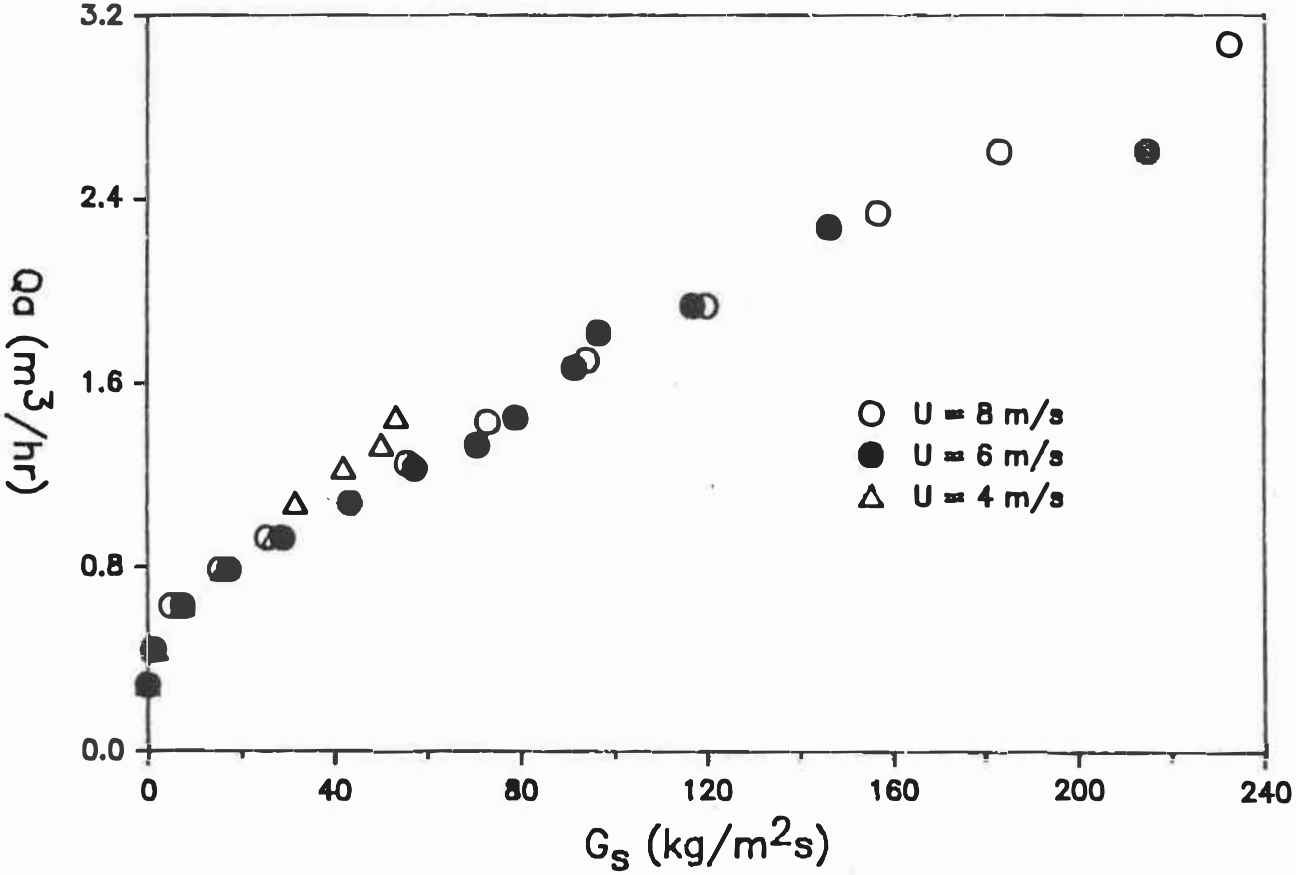

Figure 4.8: Aeration requirements at different riser gas velocities

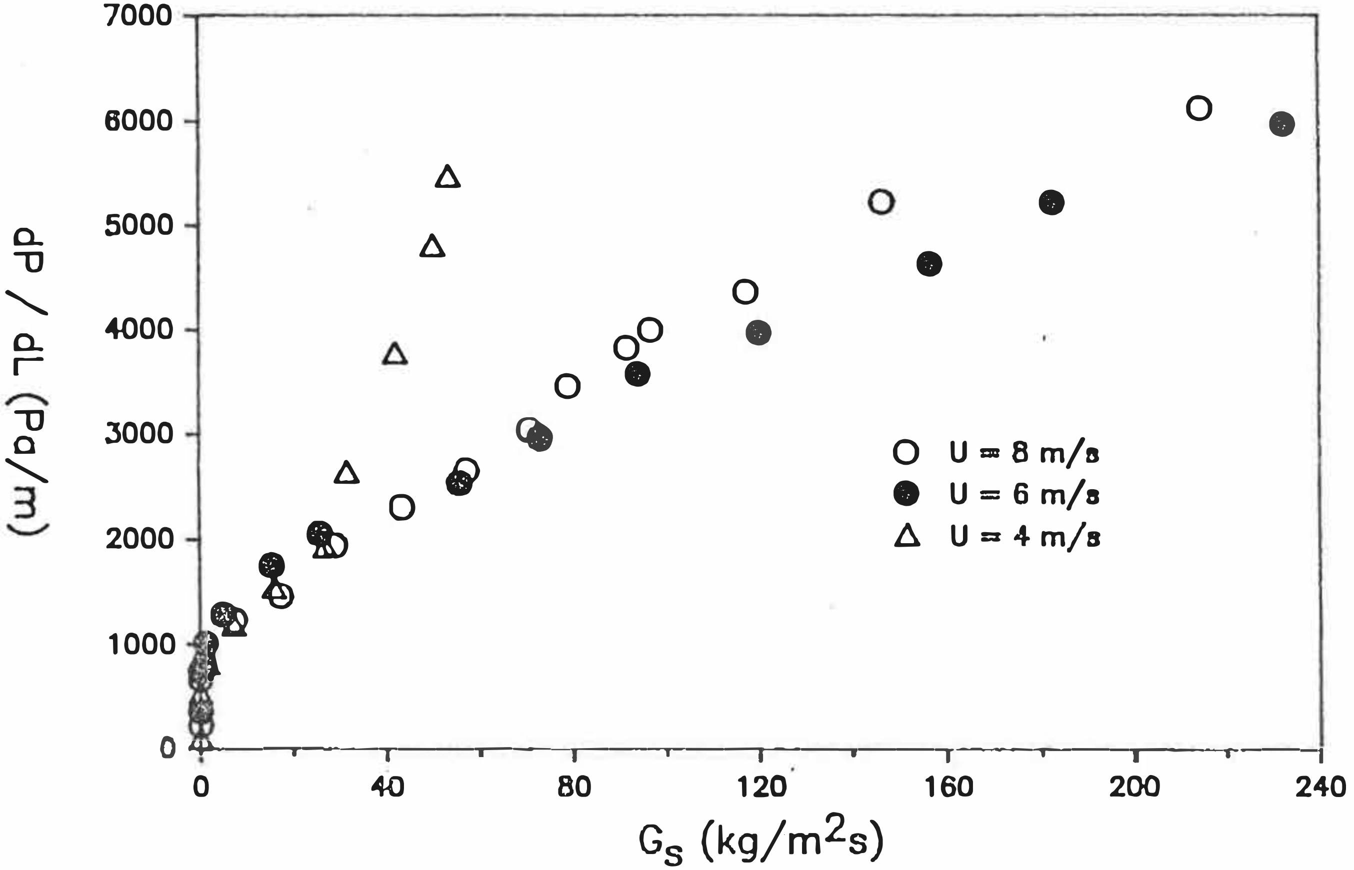

Figure 4.9: Standpipe pressure gain at different riser gas velocities

nature. Figure 4.10 illustrates the variation of the pressure drop in the L-valve with the aeration rate. No difference is evident between the three riser gas velocities.

4.3.2 Gas flow and void fraction

Unfortunately, there is little published research concerning the gas phase in standpipe flow. Previous to Yoon and Kunii (1970), gas phase studies were limited to measuring the flow rate at the top of the bed. Yoon and Kunii (1970), using helium as a tracer, were the first to directly measure the gas velocity. They showed that the modified Ergun equation, written in terms of slip velocity, could account for the large pressure gain developed in the standpipe:

$$\frac{-dP}{dz} = K_1 V_{sl} + K_2 V_{sl} |V_{sl}| \tag{4.12}$$

where,

$$K_1 = \frac{150\mu(1-\epsilon)^2}{(\psi_s d_p \epsilon)^2} \tag{4.13}$$

$$K_2 = \frac{1.75\rho(1-\epsilon)}{(\psi_s d_p \epsilon)} \tag{4.14}$$

The gas and solids flow is defined as positive downward, whereas the slip velocity is taken to be positive upward.

$$V_{sl} = V_s - V_g \tag{4.15}$$

Positive slip results for solids velocity greater than the gas

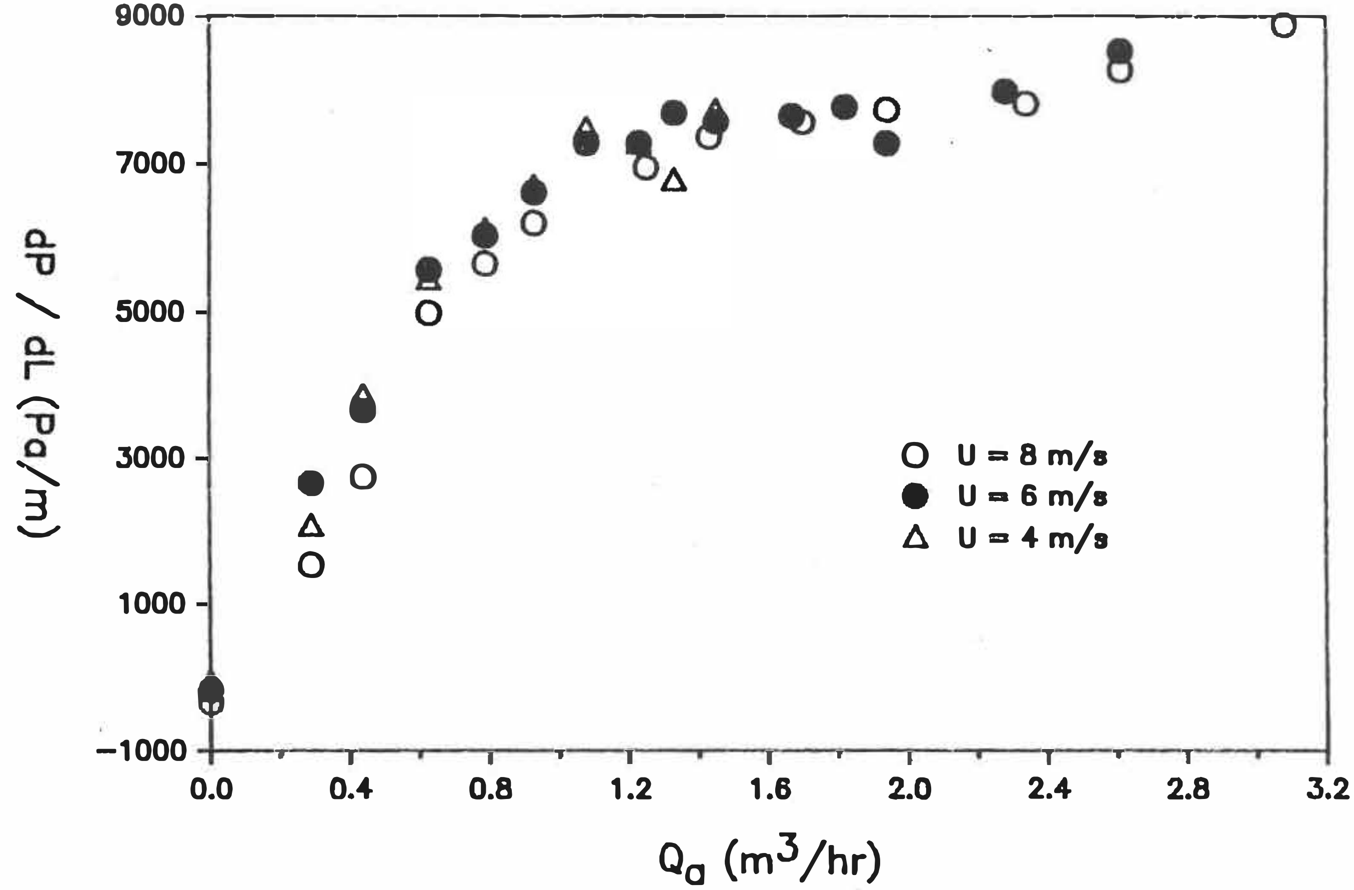

Figure 4.10: L-Valve pressure drop at different riser gas velocities

velocity in the downward direction and for upflow of gas. A negative slip is evident when the gas velocity is greater than the solids velocity in the downward direction.

Kojabashian (1958) identified two distinct flow regimes for non-fluidized downflow of solids and designated these regimes packed bed flow (PACFLO - Leung and Jones, 1978) and transitional packed bed flow (TRANPACFLO - Leung and Jones, 1978). Packed bed flow is defined as co-current particulate/gas flow with a negative slip (gas velocity greater than solids velocity in the downward direction) and a positive pressure gradient, i.e. pressure is greater higher up the column. The void fraction is constant and equal to the vibrated bed voidage. The demarcation and limits of the two flow regimes are:

$$V_{sl} < 0, \qquad \text{packed bed flow} \qquad (4.16)$$

$$0 < V_{sl} < U_{mf}/\epsilon_{mf}, \qquad \text{transitional packed bed flow} \qquad (4.17)$$

The flow can either be co-current or counter-current in TRANPACFLO as demonstrated by Equation 4.17. As long as the particulate velocity is greater than the gas velocity in the downward direction a positive slip velocity is calculated.

Knowlton and Hirsan (1978a,b) assumed that the void fraction increased linearly with the slip velocity to fit their data. However, the gas velocity was not measured. Zhang et al. (1989) suggested that the void fraction is constant and equal to the minimum fluidization void fraction in most cases and included a flow map for non-fluidized flow in standpipes restricted at the bottom by an orifice. Metered gas was introduced at the bottom hopper below the orifice and a second flow meter at the same level was used to measure the gas velocity.

In this study, both the solids and gas velocities were determined using radioactive tracers. Gas measurements entailed injecting a 3 ml sample of radioactive argon 300 mm above the first detector at a height of 2.96 m from the base of the standpipe. The transit time is the difference between the first moments of the two detectors separated by a distance of 1.78 m. The diameter of the pyrex tube is 76.4 mm, whereas the diameter of the stainless steel pipe is 82.8 mm. All measurements are made based on a 82.8 mm diameter. Therefore, the effective distance between the two detectors 1.63 m.

A typical RTD curve for the gas is illustrated in Figure 4.11. The first peak is quite narrow, whereas the second peak is much broader. This peak broadening may be attributed to either dispersion or a velocity gradient and decreases with an increasing solids mass flux. The solids dispersion is much lower than the gas dispersion.

Gas and solids velocities together with the measured pressure drop and the predicted void fractions are given in Table 4.3. The

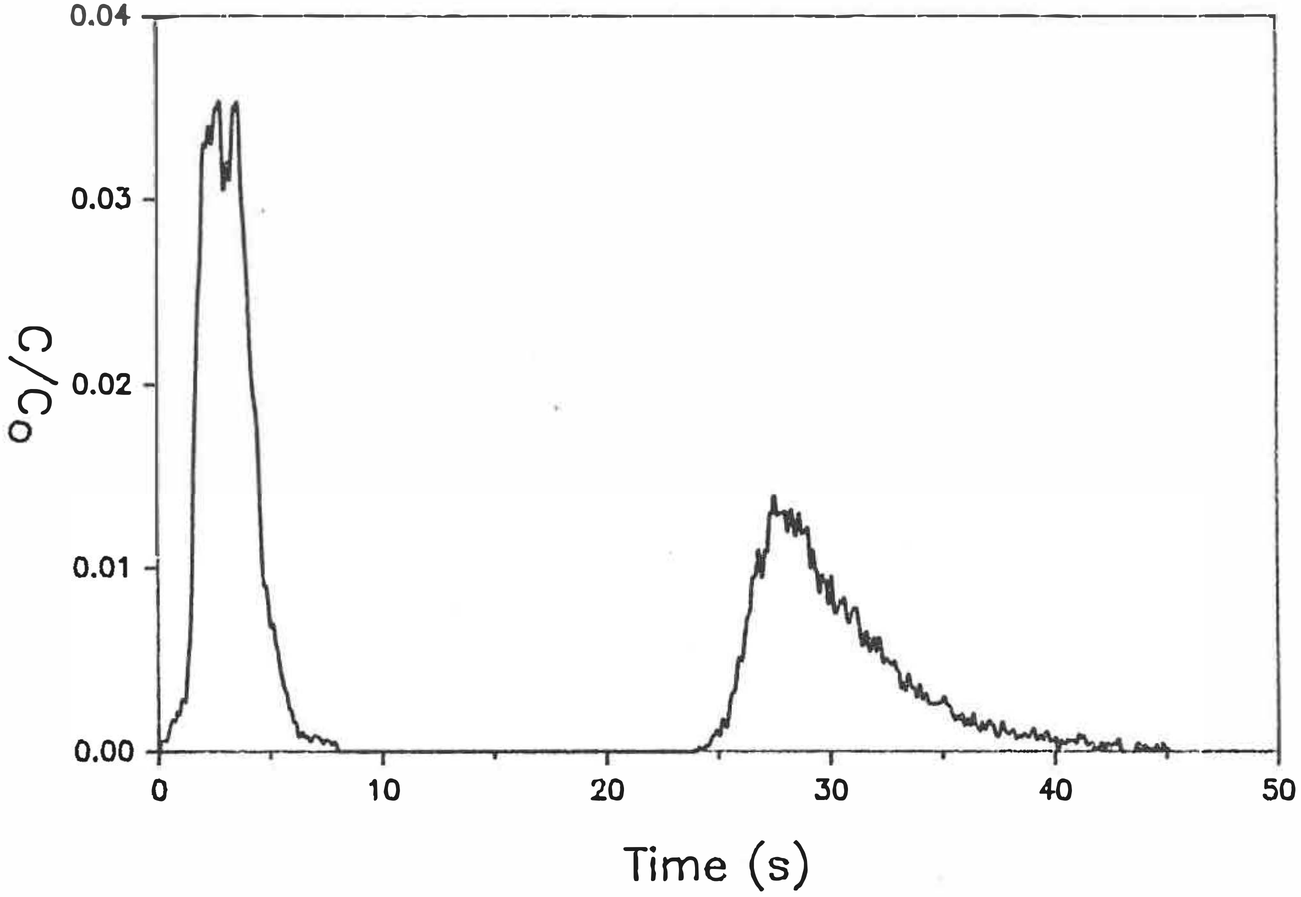

Figure 4.11: Response of two detectors in the standpipe

void fraction, calculated from Equation 4.12, is very sensitive to the assumed particle sphericity, ψ_s. McCabe and Smith (1976) suggest that the sphericity of round sand is on the order of 0.83. However, Geldart (1990) proposes that the sphericity of sand is equal to 0.87. In consideration of the abrasive nature of the riser, sand grains will become rounder with time; hence, a higher value for the sphericity is appropriate.

The gas and solids velocities could not measured simultaneously using radioactive tracers. Instead, particle wall velocities were measured after introducing the radioactive argon. The mean particle velocity was then calculated from Figure 4.4. The results, presented in Table 4.3 show some scatter around the void fraction at minimum fluidization (ϵ_{mf}=0.41) and the loose packed density ($\epsilon_{lp=0.4}$). Assuming the minimum fluidization void fraction, as suggested by Burkell et al. (1988) and Zhang et al. (1989), is not unreasonable.

Table 4.3: Standpipe Void Fraction Variation with Slip Velocity
$U_{g,riser}$ = 8 m/s

Q_a (m^3/hr)	V_g (mm/s)	V_s (mm/s)	V_{sl} (mm/s)	dP/dL (Pa/m)	ϵ
2.61	61.7	105	43.3	4850	0.391
1.94	38.2	78	39.8	3870	0.408
1.33	12.4	40	27.6	2600	0.412
1.08	-	23	23	2080	0.417

Figure 4.12 illustrates the variation of the pressure gradient with slip velocity. Included in the figure is the calculated pressure drop assuming a constant void fraction, ϵ=0.4. The void fraction seems to descrease with an increase in circulation rate as if the bed was experiencing a vacuum. Since the uncertainty in the solids velocity measurements increase with velocity, this trend is uncertain. Radioactive tracer studies are required in which the solids are injected immediately after the gas to determine the slip velocity.

4.4 RISER HYDRODYNAMICS

The true nature of the fluid phase in the riser is debatable. The complexity of the flow phenomena, the spatial and temporal variation of the solids phase, renders its analysis and characterization difficult. The flow pattern depends on the system geometry, column diameter, inlet and exit configuration, particle properties and gas characteristics. The longitudinal distribution of the particulate phase has been modelled assuming large agglomerates or clusters as well as a dense annular phase of solids at the wall. In gas-liquid systems these models correspond to wispy annular flow and annular flow respectively. Considering the longitudinal variation of solids holdup it is reasonable to believe that the flow phenomena are comprised of many flow regimes. For example at the tee, slug or plug

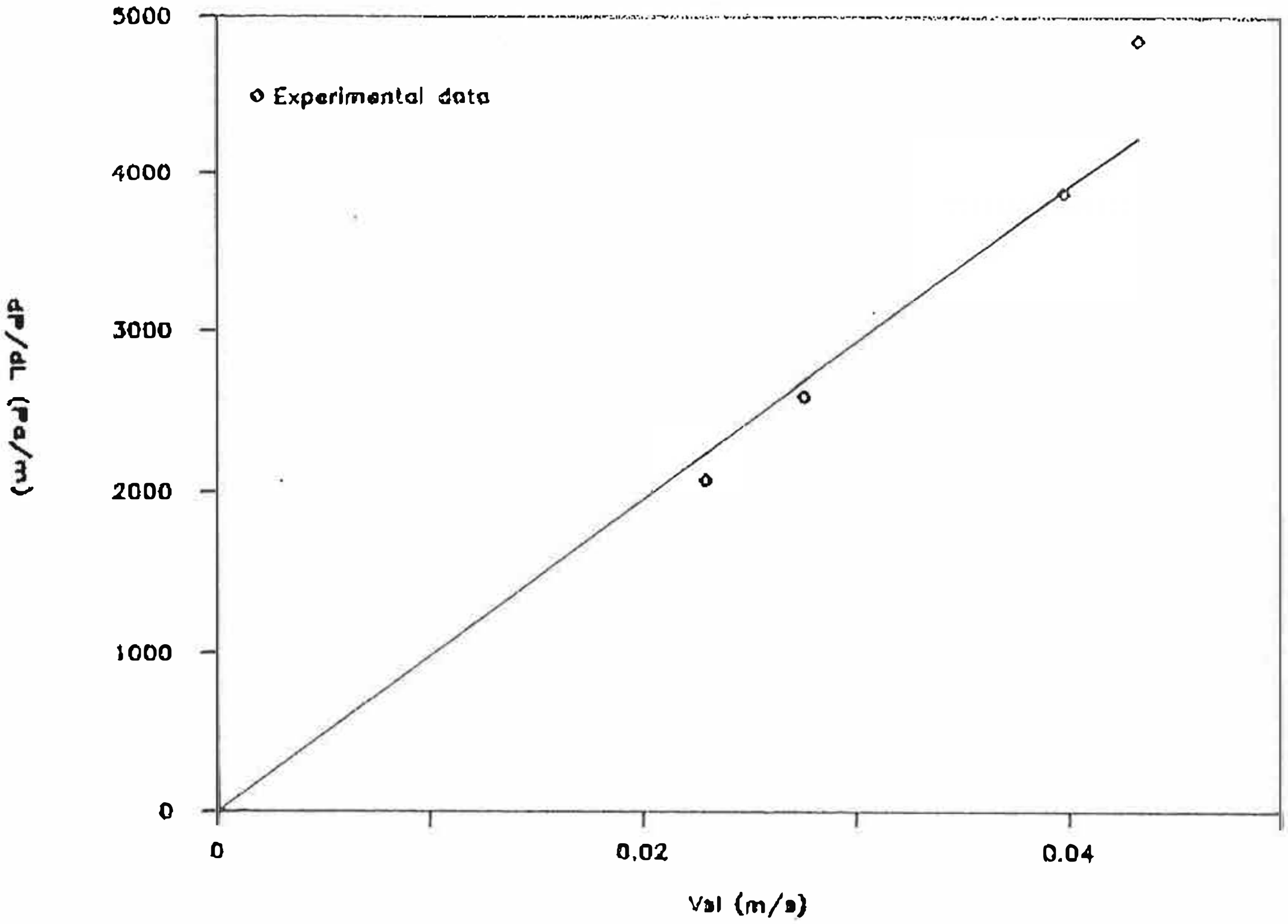

Figure 4.12: Standpipe Pressure Drop Variation with Slip Velocity

flow is evident. At the top of the column, the wispy annular flow regime dominates. Many experimental units exhibit a strong downflow of solids along the wall which would indicate annular flow. Brereton (1987) discusses the theoretical basis of the models and gives a detailed literature review. As indicated by Brereton, a number of experimental methods are available to examine the local radial and longitudinal distribution and include: tracer particles (coloured, radioactive, fluorescent salt), γ-ray photography, photography, impact meters with piezo-electric crystals, optical fibres, thermistor probes, capacitance probes, isokinetic sampling and pressure drop measurements. In Table 4.4, a list of the various methods is presented together with the researchers who employed the technique. In general, pressure fluctuations, using manometers or pressure transducers are used in conjunction with other methods.

Given the number and diversity of the experimental techniques, what then, are the conclusions concerning the hydrodynamics in the riser? Most studies suggest the presence of a dense annular region and a lean core. Isokinetic sampling studies indicate that the solids concentration increases radially from the axis, substantiating the hypothesis of a lean core region. However, the nature of the dense wall phase and core region is uncertain. For example, Brereton's (1987) study of the character of the wall and core zone indicates heterogeneity, particular to the cluster model, in both regions. At high circulation rates, the heterogeneity is most prevalent near the

Table 4.4: Experimental techniques for solids phase studies

Method	Reference
Tracers	
- Salt	Bader et al., 1986
- Coloured particles	Roberts, 1986
- Fluorescent particles	Kojima et al., 1989
Quick closing valves	Capes and Nakamura, 1973 Arena et al., 1986
Pressure fluctuations	Schnitzlein and Weinstein, 1988 Lee and Kim, 1988 Wirth, 1988 Kato et al., 1988
Fibre optic probes	Horio et al., 1986 Ishii et al., 1988, 1989 Hartge et al., 1988 Hartge et al., 1986 Matsamuto et al., 1986
Photography	Arena et al., 1989 Konno and Sato, 1969
Capacitance probes	Brereton, 1987 Hartge et al., 1986
Laser Doppler Anemometry	Lee and Srinivansan, 1978,1982
φ-ray absorption	Hartge et al., 1986
X-ray absorption	Weinstein et al., 1985
Isokinetic sampling	Rhodes and Geldart, 1986 Bolton and Davidson, 1988 Monceaux et al., 1986

base and decreases longitudinally. The wall region is typically more heterogeneous than the core, especially higher up the column. The inhomogeneous flow is described as "intermittent packets of dense and dilute phase". These observations confirm the existence of clusters, in the center of the riser but even more surprisingly imply the existence of clusters in the wall region. This result is supported by visual observations in the present study as described in the preceding section.

4.4.1 Solids Phase Models

There are almost as many theoretical models to describe the hydrodynamics in the riser as there are experimental techniques. Two general classes of models exist: those derived from the phenomenological equations of mass continuity and momentum and correlations based on experimental data. Both are empirical to a certain extent requiring parameters to fit the data. The work of Kato et al.,(1989) is a good example of an empirical model. He expresses the particle hold-up by the following equation:

$$\frac{\epsilon}{1-\epsilon} = 0.048\,\frac{e^{\alpha}}{e^{\alpha}+1}\left[\frac{U_g - V_t}{V_t}\right]^{1.35}\left[\frac{G_s}{\rho_p V_t}\right]^{-1.28} Re_p^{0.23}\, D^{-1.28} \qquad (4.18)$$

where,

$$\alpha = z - Z_i \qquad (4.19)$$

and Z_i is the height of the inflection point between the dilute phase and dense phase,

$$Z_i = 360 \left[\frac{U_g - V_t}{V_t}\right]^{-1.45} \left[\frac{G_s}{\rho_p V_t}\right]^{1.2} Re_p^{-0.29} \tag{4.20}$$

The range of application of these empirical relations is

$$1.4 \le U_g \le 6.0 \text{ m/s}, \quad 0.1 \le V_t \le 0.9 \text{ m/s}, \quad 30 \le G_s \le 130 \text{ kg/m}^2\text{s},$$
$$0.45 \le Re_p \le 10, \quad 0.04 \le D \le 0.1 \text{ m} \tag{4.21}$$

The limitations of purely empirical relations are evident upon examination of the application range: What happens when $D>0.1$?

Rhodes and Geldart (1989) develop the empirical approach a little further. They assume the lean phase (longitudinally) of CFB's behaves much like the freeboard region of fluidized beds. The entrainment flux at any height is given by

$$E_z = E_\infty + (E_o + E_\infty)\, e^{-az} \tag{4.22}$$

where E_∞ is the elutriation rate and E_o is the entrainment flux at the bed surface (Wen and Chen, 1982). The longitudinal solids concentration is calculated assuming the slip velocity is equal to the single particle terminal velocity where,

$$V_g = U_g/\epsilon_z \tag{4.23}$$

$$V_s = E_z/\rho_p(1 - \epsilon_z) \tag{4.24}$$

and,

$$V_t \epsilon_z^2 - \epsilon_z (U_g + V_t + E_z/\rho_p) + U_g = 0 \qquad (4.25)$$

Patience and Chaouki (1990) suggest an improvement to the model by replacing the elutriation rate, E_∞, with the imposed solids circulation rate, G_s. Equation (4.22) becomes

$$E_z = G_s + (E_o + G_s)\, e^{-az} \qquad (4.26)$$

A major drawback of this empirical relation is that the actual slip velocity is greater than the particle terminal velocity (Capes and Nakamura, 1973) and therefore, E_z, calculated from Equation (4.26) is not a true measure of the entrainment flux. The model could be improved by including a more realistic solids velocity.

Berruti and Kalogerakis (1989) postulate a core-annular flow model and develop expressions for each region based on the experimental results of various researchers. They assume the slip velocity in the core equals the particle terminal velocity and that solids descend along the wall at the particle terminal velocity. They also give an expression for the net particle radial flux.

Kmeic and Leschonski (1987) discuss four hydrodynamics models developed from the phenomenological equations of mass continuity and momentum for vertical pneumatic conveying. They assume one-dimensional flow and mathematically describe the transport phenomena using three equations: mass continuity of the gas and solids phase and a mixture momentum balance. The four models vary according to the postulated phase behaviour. Among the four models considered, the annular flow model and the model with the pressure drop in the fluid phase show good agreement with the experimental pressure distribution in the acceleration region of the tube.

Nakamura and Capes (1973) developed an annular flow model and proposed the following relationship for the pressure drop above the acceleration zone based on a momentum balance

$$\frac{-dP}{dz} = \rho_p(1-\epsilon)g + \frac{4}{D}(\tau_g + \tau_p) \qquad (4.27)$$

and expressed the slip velocity by

$$\frac{U_g}{\epsilon} - \frac{U_p}{1-\epsilon} = \left[\rho_p\frac{\epsilon(1-\epsilon)g}{\beta} + \frac{1}{\rho_p(1-\epsilon)}\left[\frac{4\tau_p}{gD} - \frac{4(1-\epsilon)\tau_g}{gD\epsilon}\right]\right]^{0.5} \qquad (4.28)$$

Whereas fitted parameters are essential to correlations from step one, models derived phenomenologically require empirical relations in the second step, i.e. to express the presumed behaviour of the unknowns in the developed equation. For example, in Equation (4.28) and (4.27) expressions are required for β, the fluid particle drag relationship, τ_g the gas shear stress and τ_p, the particle shear stress.

Ishii et al., (1989) developed a clustering annular flow model that contains nine material balance equations and four momentum balance equations. The model assumes that the riser essentially consists of clusters that ascend in the core as well as fall along the wall.

Hydrodynamic models predict the solids distribution from a knowledge of the system parameters, particle properties and gas velocity. The one-dimensional model proposed by Rhodes and Geldart (1989) gives an adequate cursory description of the void fraction. Model predictions compare reasonably well with experimental results. However, there is considerable evidence that the solids are heterogeneously distributed radially. Hence, a compromise must be met in minimizing the number of adjustable parameters used to fit the data and having a sufficient number to adequately model the behaviour.

4.4.2 Solids Hold-Up

The basic measurements necessary to evaluate the hydrodynamics of CFB risers include: superficial gas velocity, solids circulation rate, particle properties, and the longitudinal suspension density. The gas velocity and particle properties are generally straightforward to measure. Particle characterization is covered in many text books. A standard orifice meter is adequate to measure the gas flow rate. Solids flux measurements are not as straightforward as indicated in Section 4.2. The suspension density is calculated based on the pressure gradient.

The variation of the time averaged pressure drop along the length of the riser is illustrated in Figure 4.13 at four mass fluxes and a gas velocity of 6 m/s. The pressure drop is greatest at the solids entry and decays exponentially. At the top of the column, the pressure drop increases again. This effect, as reported earlier by Brereton (1987), is attributable to the exit geometry. For an abrupt exit, the solids tend to drop out of the suspension and cascade downwards along the wall. Smooth exits do not exhibit an increase in pressure drop.

In general, the longitudinal riser density profile is calculated assuming that the time averaged pressure gradient is equal to the weight of the solids,

$$\rho_{susp} = -\frac{1}{g}\frac{dP}{dZ} \tag{4.29}$$

Frictional effects and particle acceleration are considered negligible compared to the hydrostatic head of the solids. These assumptions are easily quantified by comparing the suspension density, given by Equation (4.28), with the estimated density including frictional and acceleration terms.

The pressure drop due to particle acceleration, as given by

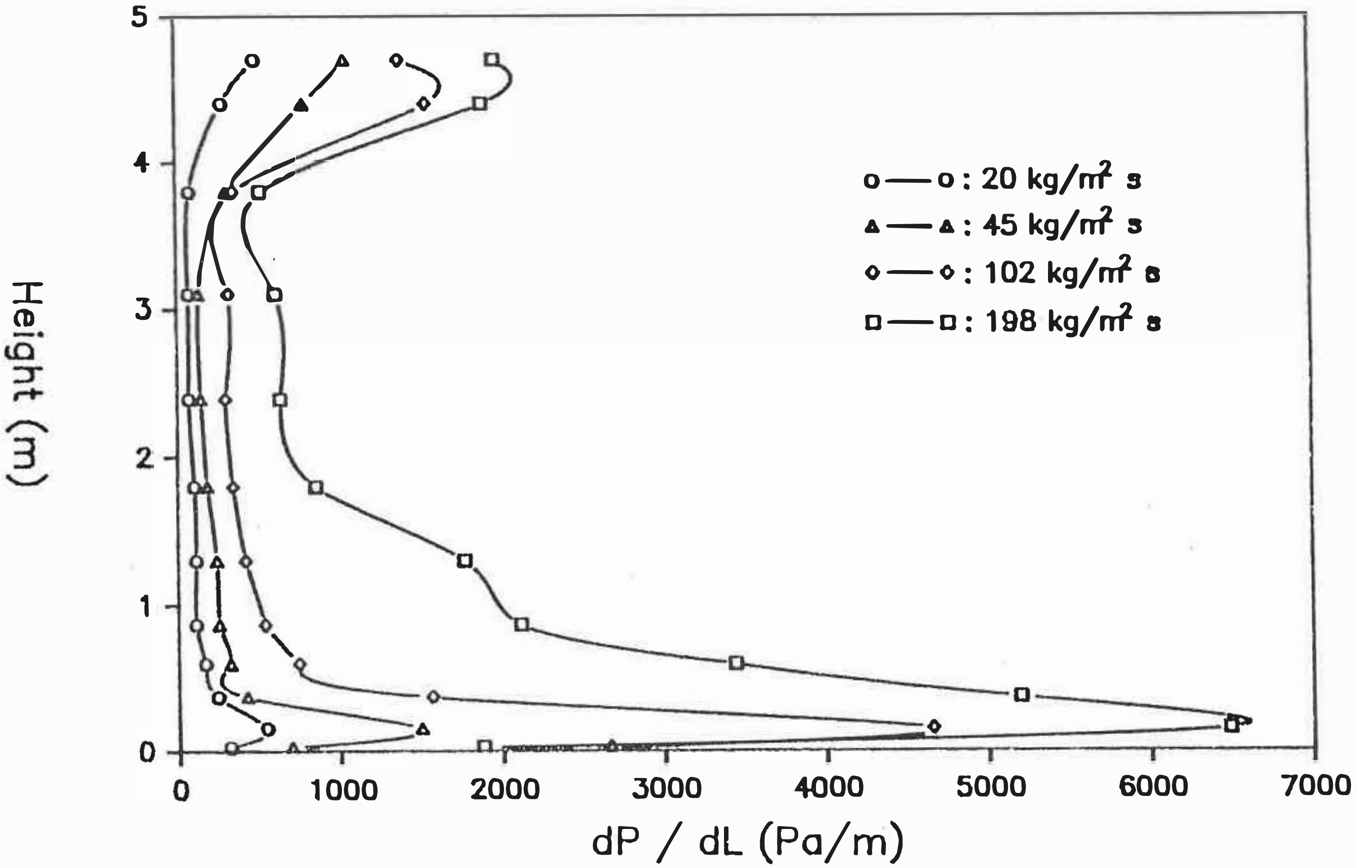

Figure 4.13: Longitudinal Pressure Gradient, U_g=6 m/s

Equations (4.8) and (4.10) is,

$$\Delta P = G_s(V_{s2} - V_{s1}) \qquad (4.30)$$

where, V_{s1} is the entrance velocity of the solids and V_{s2} is the particle velocity above the acceleration zone. In the present system, $V_{s1} = 0$ and V_{s2} is assumed equal to the difference between the gas velocity and single particle terminal velocity in an infinite medium. The acceleration pressure drop equals 820 Pa at a riser gas velocity of 8 m/s and for a solids circulation rate of 200 kg/m^{2}s. Considering that the solids are accelerated at the bottom of the riser the decelerate at the top, the net contribution is zero. The local contribution at the entrance and exit can be large. The acceleration pressure drop contribution analysis is further complicated by the radial heterogeneity, the solids refluxing along the wall, and the entrance geometry. Further discussion on the hydrodynamics of the entrance is given in Chapter 5.

The frictional contribution to the pressure drop is more difficult to quantify. Arena et al. (1988) suggest that errors could be up to 70 % in 40 mm units operating at 7 m/s if the frictional effects are ignored. Many correlations have been proposed to characterize the frictional contribution to the pressure drop. To be consistent with the analysis as given in Section 4.2, the model developed by Patience et al. (1990) for horizontal two phase flow, is used. The work by Rose and Duckworth (1969) suggests that the change in orientation has a marginal effect on the pressure drop (typically less than 10%). The frictional pressure drop over the 4.72 m length is 690 Pa at a gas velocity of 6 m/s and a circulation rate of 200 kg/m^{2}s which is lower than the acceleration pressure drop and corresponds to a pressure gradient of 146 Pa/m. This pressure gradient is equivalent to a "frictional density" equivalent of 15 kg/m^3. The frictional contribution is proportional to the solids circulation rate and decreases with an increase in diameter. Under similar operating conditions the "frictional density" in a 152 mm riser is 9.6 kg/m^3 and in a 40 mm unit it is 36 kg/m^3.

In Figure 4.14, the variation of the suspension density along the length of the riser is presented. In the lean phase (above a height of 2 m for G_s=198 kg/m^{2}s and U_g=6 m/s) the suspension density is approximately 65 kg/m^3, which suggests that the frictional contribution to the measured density is 25% of the total. The Julian-Duckler (1965) correlation predicts a frictional pressure drop about 8 % of the measured pressure drop. In the lean phase of risers particles are generally assumed to ascend with a slip velocity equal to the particle terminal velocity. Equation 4.9 correlates data taken in the acceleration region where the relative velocity between the gas and solids is much greater than the terminal velocity. Hence, predicted frictional pressure drops are presumably to high. The Julian-Duckler correlation indicates that frictional contributions in

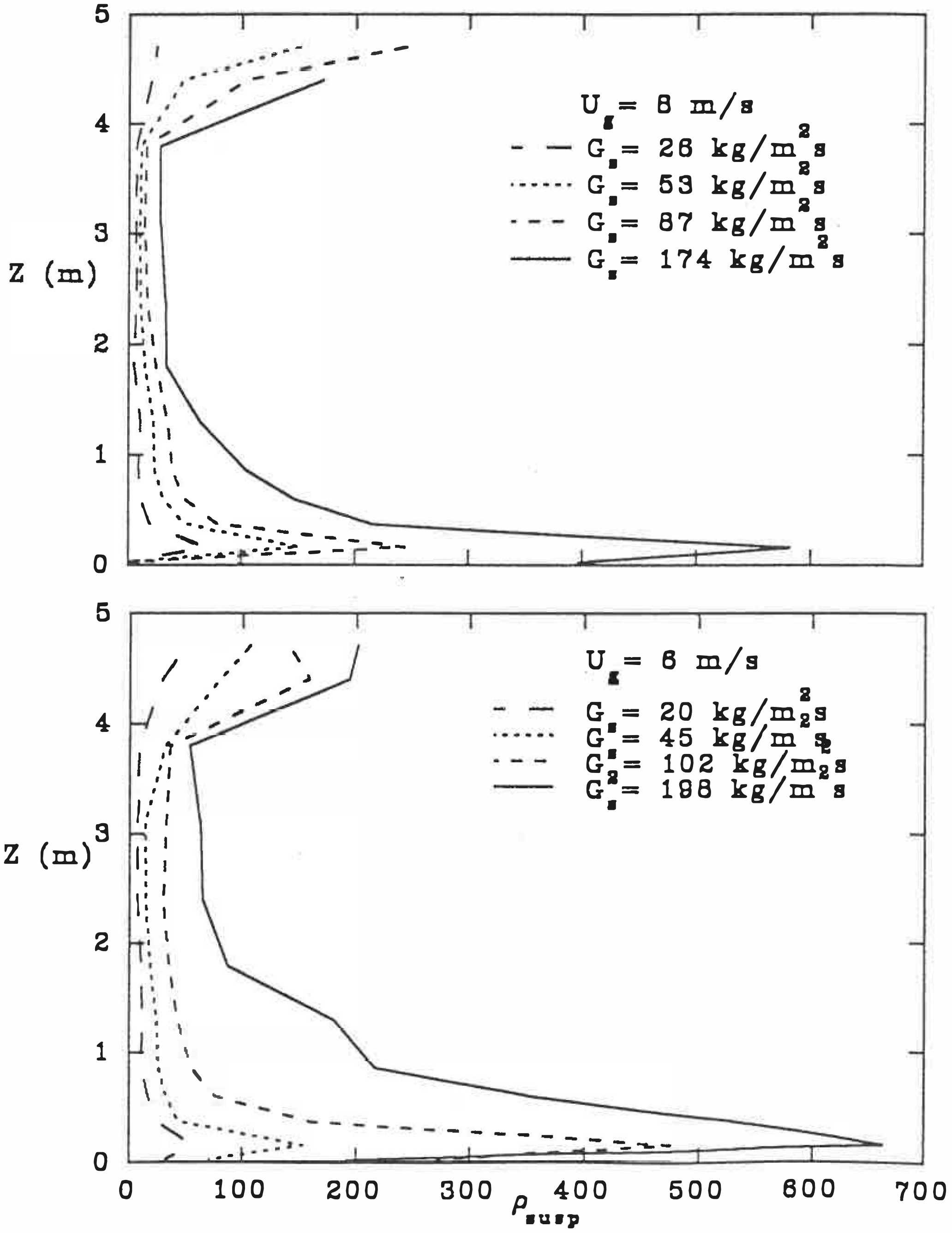

Figure 4.14: Longitudinal Suspension Density

the riser, at the conditions tested, are largely negligible. Even in the developing region (i.e. $Z<2$ m) the frictional pressure drop calculated by Equation 4.9 is negligible compared to the measured pressure drop.

5. GAS AND SOLIDS RESIDENCE TIME DISTRIBUTION

The phase behaviour of gas-solid mixtures in flow systems has been examined using a number of measuring techniques, including: high speed photography, optical probes, mechanical devices such as quick closing valves, electro-capacitance probes, laser Doppler anemometry, iso-kinetic sampling and tracers. Tracer studies entail injecting a detectable species, either continuously or as a slug, into a vessel and measuring the concentration at a distant point. In the chemical engineering literature the resultant residence time density function is commonly referred to as the residence time distribution (RTD) curve. In general, the RTD curve is used to determine such phenomena as dispersion, channeling, short circuiting, internal recirculation and stagnant regions. It depends on a number of factors including the input function, the system geometry, boundary conditions and the detection method. For example, the output concentration of a slug injection, characterized as a Heaviside unit step function, is much different than for a Gaussian or isosceles triangular input function.

Radioactive tracers are particularly suited as a means to examine the gas and particulate phase of CFBs. They are versatile, non-intrusive, capable of in-situ measurement, on-line and easily detected. In addition, relatively small quantities are required which minimizes the injection perturbation. The solids phase is traced with irradiated sand and radioactive argon is used for the gas phase.

Empty column studies were conducted to serve as standards with which to compare the RTD of the gas and solids phase under normal operating conditions. In addition, the results of the control studies were compared with literature values to establish the injection and detection methods. Together with the empty column experiments, the following parameters are considered: superficial gas velocity, solids circulation rate, particle size, injector position and detector position.

5.1 GAS RTD

Gas residence time distribution (RTD) measurements are useful to evaluate the potential of CFBs as catalytic reactors. Generally, CFBs are characterized as excellent gas-solid contactors in which the gas phase approaches plug flow. In Table 5.1, the techniques used to trace the gas phase together with the researchers are listed. The early studies by Cankurt and Yerushalmi (1978) and Yang et al. (1983) indicate that gas back mixing is practically negligible. The recent studies of Weinstein et al. (1989) and Brereton et al. (1988) suggest that a single parameter dispersion model is inadequate to describe the large variance. The apparent discrepancy in the results have been attributed to the injection method (Weinstein et al., 1989). The gas and solids are heterogeneously distributed across the radius. Therefore it is necessary to distribute tracer uniformly over the cross section or inject tracer at a number of radial positions. Tracer was injected in the center of the column in the earlier studies. In the present investigation, a pulse of radioactive argon is introduced tangentially into the reactor by a syringe. The argon is assumed to distribute across the radius uniformly. The tracer is detected at three locations: at heights of 1 m, 4 m and in the horizontal section between the cyclone and the riser 4.72 m above the point of injection. In addition, the radioactive argon is injected 1.5 m above the distributor to examine the lean region.

Table 5.1: Gas RTD Measurement Techniques

Tracer	Injection method	References
CH_4	continuous	Cankurt & Yerushalmi, 1978 Adams, 1988
He	continuous	Yang et al., 1985 Bader et al., 1988 Weinstein et al., 1989
	semi-continuous	Brereton et al., 1988
Ar	pulse	Helmrich et al., 1986
CO_2	pulse	Helmrich et al., 1986
Hot air	pulse	Dry et al., 1987

5.1.1 Empty column measurements

Levenspiel (1972) has collected data for axial dispersion coefficients in turbulent flow in empty tubes. Considerable scatter is evident because much of the data were taken in commercial pipelines with valves, elbows and other types of flow disturbances. In this study, two detectors in series measure the gas residence time density function. The difference between the means gives a reliable measure of the transit time between the detectors from which the gas velocity is calculated,

$$\mu_2 - \mu_1 = L/V_g \tag{5.1}$$

where, 1 refers to the response of the detector immediately downstream of the injector and 2 refers to the response further up the column. The agreement between the predicted gas velocity and that obtained by an orifice meter is quite good as shown in Table 5.2. The orifice was calibrated using a gas counter. The design equation for the orifice is as follows,

$$U_g = 0.0563\ (P\Delta P_o)^{0.5} \tag{5.2}$$

where, ΔP_o is the pressure drop across the orifice, P is the line pressure and U_g is the superficial gas velocity in the riser.

The Peclet number is calculated based on the difference of the second moments,

Table 5.2: Comparison of Gas Velocity from RTD Measurements and the Orifice Calibration

P (kPa)	ΔP_o (kPa)	V_g (orifice) (m/s)	V_g (RTD) (m/s)
758	6.94	4.08	4.06
745	15.7	6.09	6.10
717	28.6	8.06	8.18

Table 5.3: Empty Column Gas Dispersion in Turbulent Flow

V_g (m/s)	D_{exp} (m^2/s)	Pe_{exp}	D_{lit} (m^2/s)	Pe_{lit}
4	0.085- 0.13	157 - 101	0.11	110
6	0.10 - 0.14	172 - 125	0.14	130
8	0.13 - 0.18	180 - 135	0.17	142

$$\sigma_2^2 - \sigma_1^2 - \Delta\sigma_{det}^2 = 2/Pe \qquad (5.3)$$

Results of the predicted dispersion coefficients and Peclet numbers are compared with the literature values in Table 5.3. A number of experiments were performed to determine the variation. The variability in the data, noted previously by Levenspiel and Bischoff (1962), has been attributed to the contribution of accessories such as valves, elbows, fittings etc. However, in this study, measurements were taken in straight tubes indicating that the variability in the dispersion is a result of the other factors, principally, the incertitude in defining the cut-off point. The second moment represents the square of the spread of the distribution. A long tail will bias results and increase the calculated dispersion.

Figure 5.1 shows typical responses to an impulse of radioactive argon at three gas velocities. The first peak corresponds to the signal recorded by the detector 0.86 m above the injector and the second to the detector at a height of 3.89 m. The analyzer dwell time was set at 0.02 s. The argon tracer reaches the first detector in approximately 0.11 s at a gas velocity of 8 m/s and about 0.2 s at a velocity of 4.2 m/s. Assuming the transit time is given by,

$$t = \mu - t_{inj}/2 \qquad (5.4)$$

the experimental gas velocity is the distance to the detector divided by the time. Calculated gas velocities are given Table 5.4. The

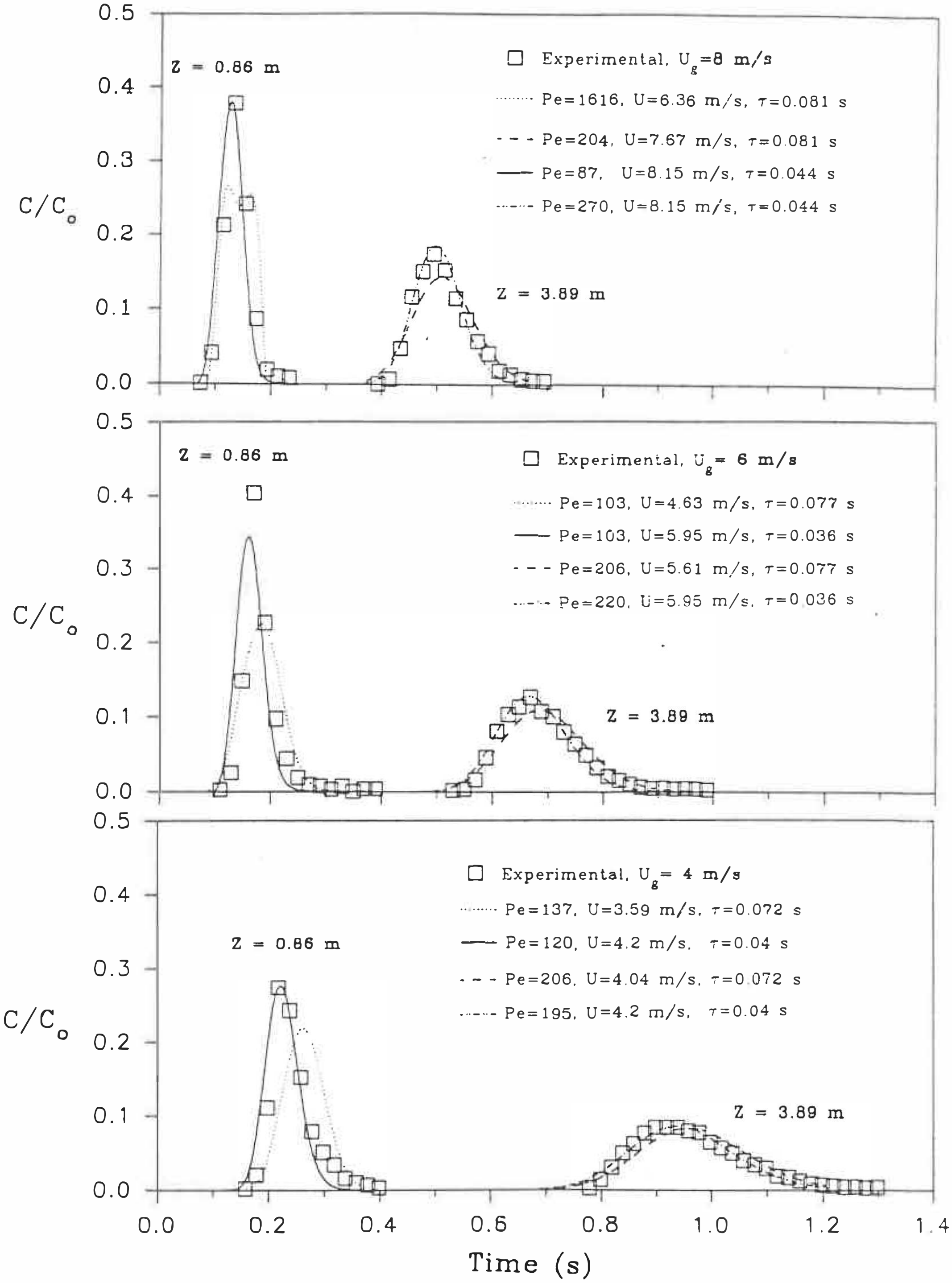

Figure 5.1: Empty column gas RTD

second column is the average velocity between the two detectors from Equation (5.1). The values in the third column are the predicted gas velocities using Equation (5.4). Whereas the difference of the first moments of the two detectors agrees with the orifice calibration, the experimental velocity given by Equation (5.4) does not. The calculated gas velocity between the injection point and detector was lower than the velocity between the two detectors. The reason for this discrepancy is not attributable to gas acceleration or poor mixing at the injection point but rather to the syringe injector, i.e. injection pulse.

Included in Table 5.4 are the predicted dispersion coefficients and Peclet numbers assuming the injection pulse is a bolus. The calculated RTD curve is compared with the experimental results in Figure 5.1. The maximum peaks predicted by the analytical expression given by Equation (3.22) is much lower than the data at 0.86 m. The match between the two at 3.89 m is better, however, the analytical solution still under predicts the peaks. The tall first peaks cannot be explained based on acceleration effects nor on poor mixing characteristics. The radioactive pulse passes the detector as a reasonably concentrated packet indicating little dispersion. Unreasonably high Peclet numbers are required to model this behaviour, particularly at 8 m/s for which Pe=1600.

The original analysis assumes a syringe input function of a

Table 5.4: Mean velocity and Pe number compared with values predicted assuming a bolus input pulse

Z (m)	V_g (m/s)	V_{inj-z} (m/s)	Pe	Pe_{inj-z}
0.86	4.20	3.59	98	138
3.89		4.04		205
0.86	5.95	4.63	123	103
3.89		5.61		297
0.86	8.15	6.36	135	1616
3.89		7.67		261

bolus which requires the tracer be injected at a constant velocity over the length of the plunger stroke. This assumption is probably not valid. In fact, the plunger accelerates from the time it hits the first micro-switch until the end of the stroke. There is some resistance to the movement of the gas which may indicate compression. Hence, the gas enters the reactor only after some delay. The true input function is more likely to be a skewed Gaussian than a bolus. Solving such an input function is complicated, so a simple model was assumed: a bolus with a delay. This model is not easily verified experimentally. However, the match between the experimental data and the numerical predictions, as shown in Figure 5.1, is very good. The peak heights are sensitive to the width of the pulse. Long pulse times correspond to short maximum peaks that are shifted to the right. Tall peaks are characteristic of short injection times. The detector 0.86 m downstream of the injector is very sensitive to the assumed injection pulse, errors of ±0.02 s at gas velocities of 8 m/s result in errors of up to 20%. The sensitivity to the injector pulse is much less at a distance of 4 m. In Table 5.5 the delay times and assumed Peclet numbers are presented.

Table 5.5: Pe numbers assuming a bolus input pulse with a delay

Z (m)	V_g (m/s)	t_{inj} (s)	t_{delay} (s)	Pe_{inj-Z}
0.86	4.20	0.072	0.032	120
3.89				195
0.86	5.95	0.077	0.041	100
3.89				220
0.86	8.15	0.081	0.037	87
3.89				270

The results presented above are qualitative in nature. Much more study is required, and is possible with the present experimental apparatus, to better define the single phase turbulent dispersion characteristics. Comparing variances is inaccurate due to the weight attributed to the tail. It is preferable to compare the curve shapes and peak heights. The results indicate that tracer injection may not be assumed to be a bolus and that a delay time should be included to account for the plunger acceleration and syringe effects. Model predictions, presented in Figure 5.1, match the data reasonably well. The detector 0.86 m downstream of the injector is the most sensitive to error. However, maximum peak heights are sensitive to the injection time, hence, reasonable estimates may be deduced by comparing experimental peak heights with predicted values. In addition, dispersion coefficients based on the calculated second moments show a large spread due to the uncertainty of the tail.

5.1.2 Dilute Phase Gas RTD

At low solids circulation rates the longitudinal voidage profile is nearly constant. The response curve of a dilute suspension of solids is compared to the single phase turbulent response curve in Figure 5.2 at gas velocities of 6 and 8 m/s. The shapes of the curves with and without solids are similar at a distance 0.86 m downstream from the detector. The tracer response recorded by the detector positioned at a height of 3.89 m and a gas velocity of 8 m/s exhibits a long tail. At a gas velocity of 6 m/s, multiple peaks are recorded by the detector positioned in the horizontal section between the cyclone and riser. The apparent flow anomalies are probably due to the solids that descend along the wall at the top of the column which entrains some gas. It is important to distinguish exit effects and the effects of solids on dispersion. The following discussion details gas RTD in the lean zone without exit effects.

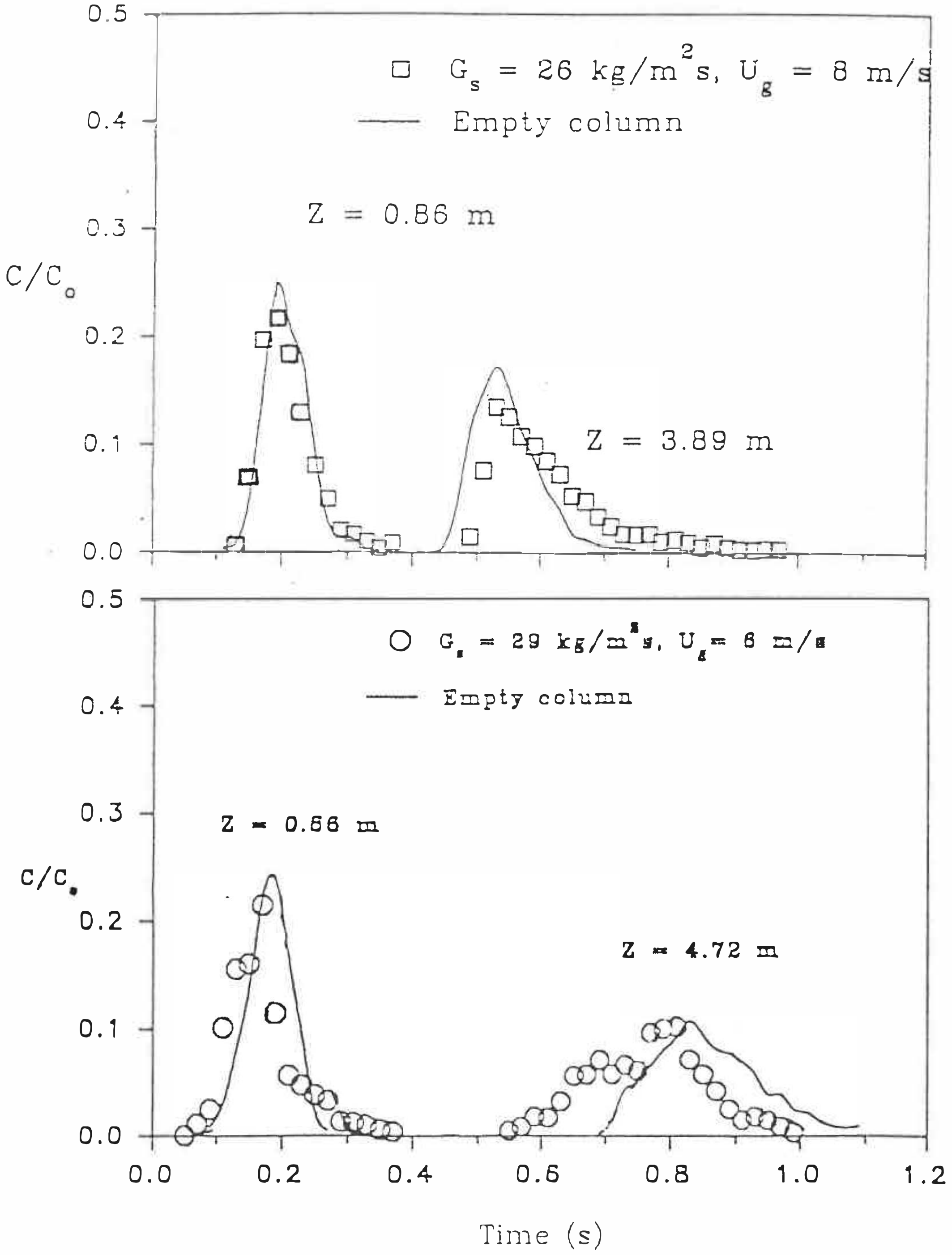

Figure 5.2: Gas Tracer Response at Low Solids Circulation Rates

Under normal operating conditions, the riser reactor contains two distinctive longitudinal regions. At the base, near the solids entry, the gas-solids mixture is characterized as highly turbulent. Above this dense, turbulent phase is a relatively lean gas-solids suspension. Injecting at the bottom of the riser, into the dense mixture, and detecting at the top of the column gives average results over the entire length. Interpreting the data to characterize the flow either in the dense region or lean region is impossible. Therefore, tracer studies were performed in the middle of the column to determine the flow characteristics of the lean region. Typical response curves are shown in Figure 5.3. Radioactive argon is injected 1.75 m above the distributor, the detector is positioned at a height of 3.99 m. Two circulation rates were tested, G_s=116 kg/m^{2}s and G_s=60 kg/m^{2}s; the gas velocities were 8.1 m/s and 7.9 m/s. The curves are quite narrow and a significant tail is evident. Assuming a simple one-dimensional dispersion type model results in a Peclet number of over 300. The form of the curve does not fit the data well. Most studies concerning CFB risers indicate the existence of radial flow segregation. Therefore, a single parameter does not accurately represent the flow phenomena.

Brereton et al. (1988) have modelled the gas phase assuming that the cross-section can be divided into two zones; a dense stagnant annulus and a lean core. The following equations describe the

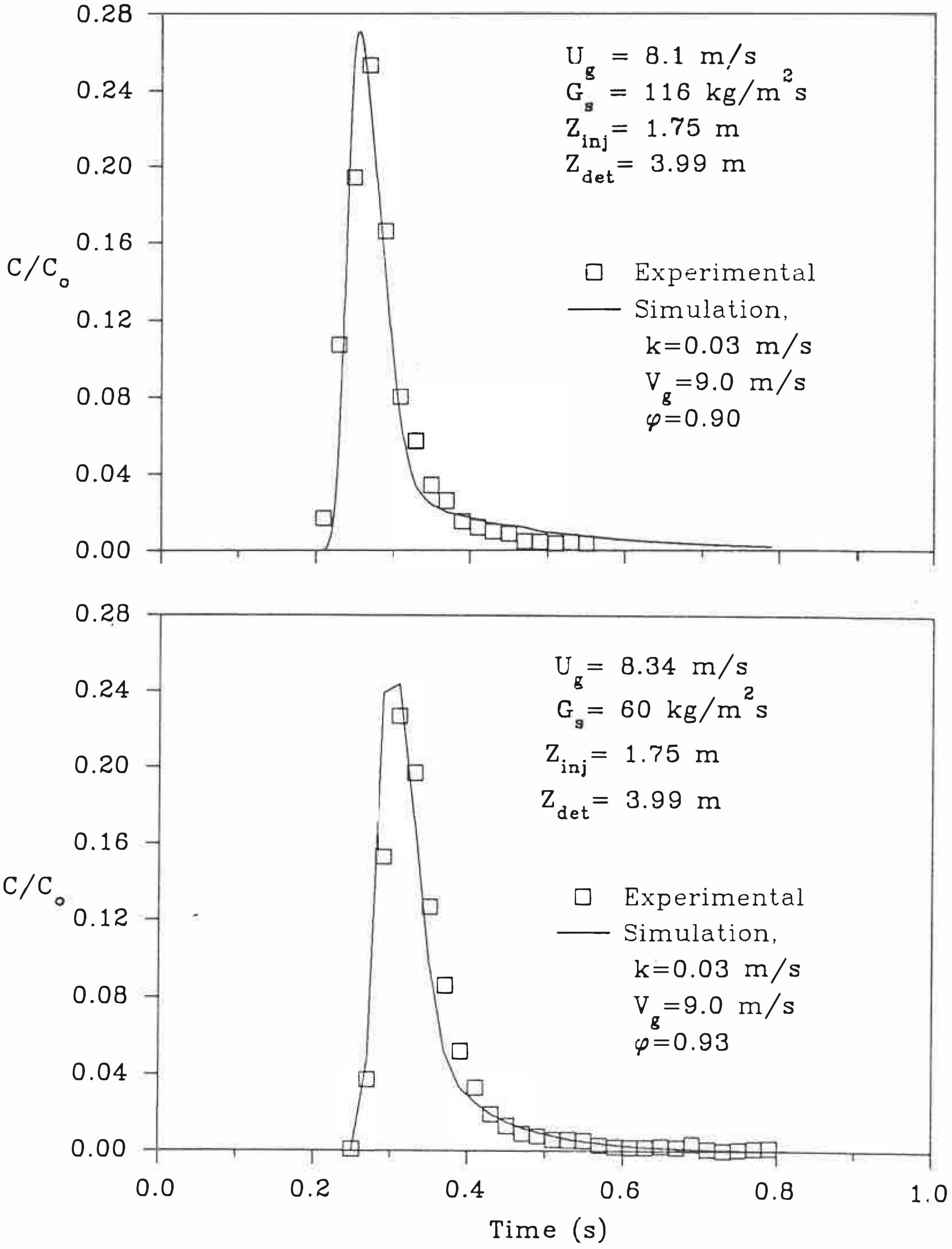

Figure 5.3: Lean Phase Gas RTD

proposed model,

$$\frac{\partial C_c}{\partial t} + V_c \frac{\partial C_c}{\partial z} = -\frac{2k}{r_c}(C_c - C_a) \tag{5.5}$$

$$\frac{\partial C_a}{\partial t} = 2kr_c/(R^2 - r_c{}^2)(C_c - C_a) \tag{5.6}$$

with the following initial and boundary conditions:

$$C_a = C_c = 0, \qquad z > 0, \quad t = 0 \tag{5.7}$$

$$C_a = C_o, \qquad z = 0, \quad t > 0 \tag{5.8}$$

$$\partial C_c/\partial z = 0, \qquad z = L \quad t > 0 \tag{5.9}$$

The exit concentration is assumed to be C_c, k is the transfer coefficient between the two zones and r_c is the radius of the core.

Equation (5.5) and (5.6) are solved numerically as outlined in Section 3.2. Forward numerical dispersion is eliminated by introducing a 'break-through' parameter into the computer program. The only mode for longitudinal transport is by convection; hence, the concentration can advance only as quickly as the velocity of the stream. For example, if the first grid block is one metre long (this example is exaggerated for demonstration purposes) and the gas velocity is 1 m/s, tracer cannot reach the second grid block before 1 s. The equations are expressed so that all concentrations at distances greater than the time multiplied by the velocity are zero.

The core gas velocity is difficult to measure; it depends on mass hold-up and radial solids distribution. Assuming two zones exist across the radius, it is necessary to determine the fraction occupied by the stagnant zone. Velocity measurements are further complicated because the actual time at which the gas first enters the riser is not known precisely. The gas injector calibration indicates that the input function can be considered as a bolus with a delay, but the injection time is not constant and varies from run to run. To accurately determine the effective injection time and delay the computer program is used to fit the data. The peak height is extremely sensitive to the assumed injection time, small changes in the pulse length change the predicted maximum peak heights significantly. It is not as sensitive to the mass transfer coefficient, k. Hence the two parameters are not coupled and may be fitted independently.

The core velocity is simply the distance between the injector and detector divided by the difference in times at which the peaks reach maxima. The radius and volume fraction of the lean core are,

$$r_c = R(U_g/V_g)^{0.5} \tag{5.10}$$

$$\varphi = (r_c/R)^2 \tag{5.11}$$

At a superficial gas velocity of 8.1 m/s and a solids circulation rate of 116 kg/m^{2}s the core velocity is 9.0 m/s and φ=0.9. Results of the numerical simulation with k=0.03 m/s are presented together with the experimental values in Figure 5.3. The agreement between the experimental curve and numerical solution is quite good. A reasonable fit to the data is obtained with k=0.03 at G_s=60 kg/m^2s and U_g=8.34 m/s as demonstrated in Figure 5.3. The core velocity is 9.0 m/s and φ=0.93. The stagnant zone decreases as the solids circulation rate decreases; however,he mass transfer coefficient changes little.

Results of Brereton et al. (1988) are not directly comparable with the data presented above. Tracer was introduced in the windbox and detected at the top of the riser in their experiment, and their CFB unit is almost twice the diameter and height of the present system. They considered a gas velocity of 7.1 m/s and a solids flux of 60 kg/m^2s. The equations were solved explicitly, and the best fit values of φ and k were 0.68 and 0.08 m/s, respectively. The higher value for k is most probably due to the turbulence in the dense region at base of the column and at the exit. A better fit to the data, obeying continuity, might be obtained by assuming a larger core radius, hence a lower core velocity, which is consistent with the results presented in Figure 5.3.

Small quantities of solids may affect the gas residence time distribution in the riser considerably. The long tails and curve abnormalities present in the low solids circulation rates are attributable to the increased solids concentration at the exit. A simple two zone model is adequate to model the behaviour of the gas in the lean phase of risers operating at normal circulation rates.

5.1.3 Overall Riser Gas RTD

The lean region of the riser may be adequately modelled using two zones, a lean core and a dense annulus. Does this assumption hold for the dense phase at the solids entrance? A cursory glance at the RTD distribution, presented in Figure 5.4 for U_g=8.0 m/s and at two solid circulation rates, G_s=116 kg/m^{2}s and 60 kg/m^2, suggests that it does. The recorded signal at the first detector (0.86m) is very narrow and tall with a noticeable tail. The tail does not decay uniformly as in the dilute phase study; secondary flow patterns are evident.

Stagnant regions with mass transfer to the flowing stream generally have smooth tracer response curves, while recycle flow response curves can have bumps and humps and other things. The RTD at the first detector is relatively smooth. In Figure 5.4, a slight hump at the second detector is apparent at a circulation rate of 116 kg/m^{2}s. The the hump is more prominent at 60 kg/m^{2}s indicating larger extents of internal recirculation. The reason for the large difference has not been attributed to the random nature of the flow behaviour, although it is tempting to suppose this, but to the position of the detector. The detector is located in the horizontal section between

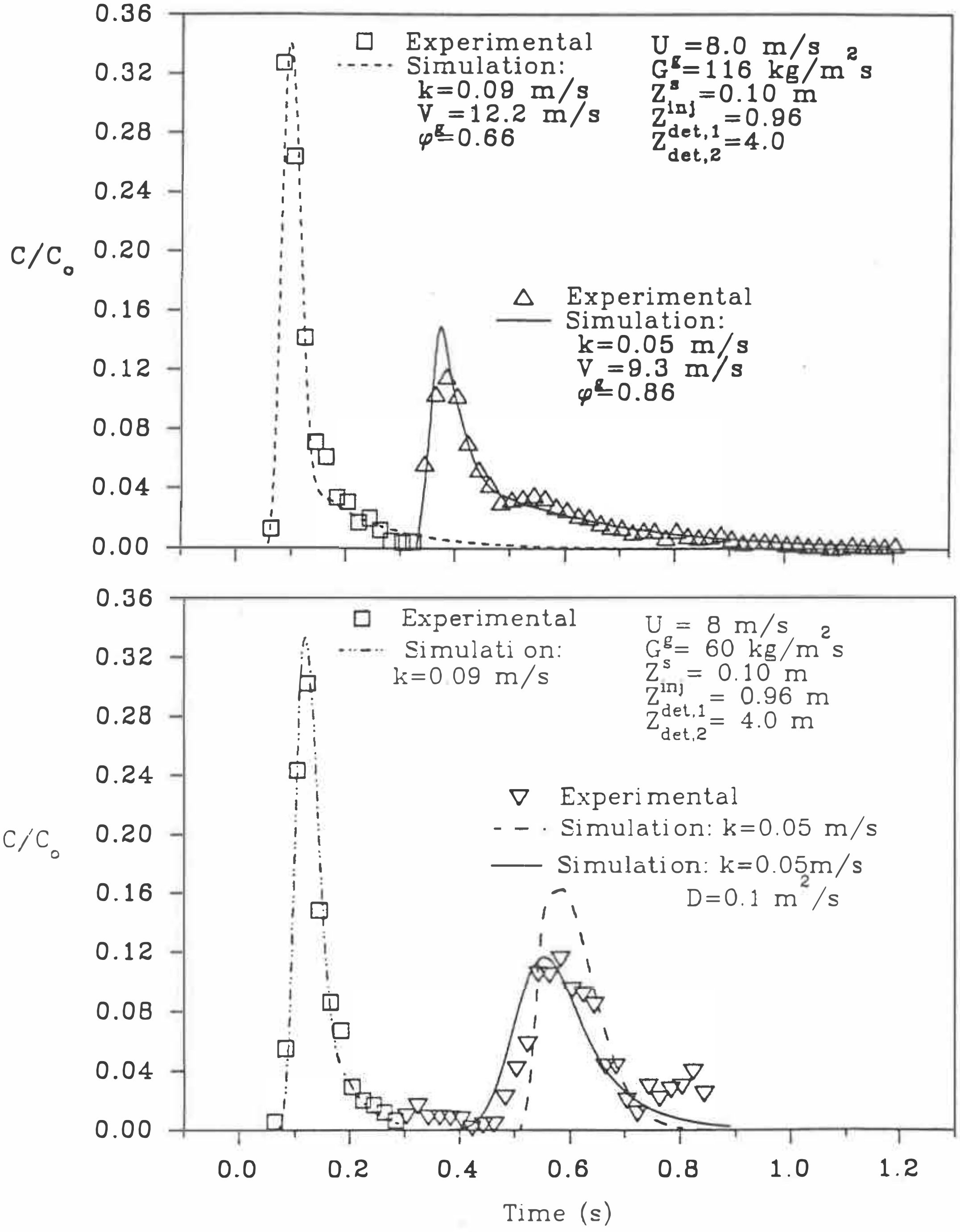

Figure 5.4: Gas RTD, injection at the tee

the riser and cyclone at the lower circulation rate. Evidently the effect of the exit geometry is not insignificant.

The injection time is critical to the RTD analysis over short distances. At superficial gas velocities of 8 m/s and distances of 1 m errors of ±0.01 s correspond to an uncertainty in the gas velocity of ± 0.8 m/s. Fortunately, the calculated height of the first peak is equally sensitive to the assumed pulse length so that an accurate injection time may be evaluated. The measured maximum normalized concentration shown in Figure 5.4 is 0.327. Solving Equations (5.5) and (5.6) assuming an impulse of 0.046 s gives a maximum value of only 0.29. A maximum value of 0.33 is calculated assuming an injection pulse of 0.040 s. The measured injection time was 0.066 s. Consequently, the delay time is 0.026 s necessitating a translation of the experimental results to the left by this amount. Assuming a simple bolus injection results in a calculated velocity of 7.4 m/s, less than the superficial velocity. The actual gas velocity, based on the corrected injection time, ranges from 13.4 to 12.2 m/s and φ from 0.6 to 0.64 At least 36% of the cross-section is taken up by the annular ring.

Results from the simulation assuming a gas velocity of 12.2 m/s and k=0.09 are included in Figure 5.4. The fit between the experimental and numerical results is quite good. This figure demonstrates that a two-zone model adequately represents the phase behaviour of the gas. However, it should be recognized that any two zone model, such as a cluster or cluster-annular model, could be made to fit the data given the appropriate mass transfer coefficient. Equations (5.5) and (5.6) should not be interpreted literally suggesting that the dense region is restricted to the annulus. Moreover, the flow abnormalities could be attributed to tracer that diffuses into a cluster, for example, with which it is transported to the top of the riser.

The response to the impulse of tracer recorded by the second detector is more rounded than the first and may be ascribed to dispersion. Best fit parameters to the curve are k=0.05 m/s and φ=0.86. It is interesting to note that the mass transfer coefficient, k, and the core volume fraction, φ, over the 3.9 m length are between the parameters used to fit the data in the dense region and dilute region.

The principal difference between the results at the lower solids circulation rate and at G_s=116 kg/m^{2}s is the location of the second detector. The injection time was not recorded. Therefore, any attempt to estimate the solids hold-up would be mere speculation. However, the mass transfer coefficient is less sensitive to the solids velocity and a reasonable fit to the data was obtained with k=0.09 m/s. The response curve of the second detector clearly demonstrates the effects of dispersion. The tall curve gives the model prediction assuming a core annular model for k=0.05 m/s. The lower curve corresponds to a combined dispersion-annular-core model,

$$\frac{\partial C_c}{\partial t} + V_c \frac{\partial C_c}{\partial z} = \frac{-2k}{r_c} (C_c - C_a) + D \frac{\partial^2 C}{\partial z^2} \tag{5.12}$$

$$\frac{\partial C_a}{\partial t} = 2k r_c / (R^2 - r_c{}^2)(C_c - C_a) \tag{5.13}$$

The model fits the data well with an assumed dispersion coefficient of 0.1 m^2/s.

Bader et al. (1988) report data taken in a 0.305 m diameter riser with equilibrium cracking catalyst (d_p=76 μm) at a gas velocity of 6.1 m/s and a solids flux of 98 kg/m^2s. They indicate that φ ranges from a value of 0.74 to 0.92. However, they contend that 75% of the gas passes through 80% of the cross sectional area (i.e., φ=0.64).

The following expressions are proposed to correlate the variation of the cross-flow coefficient and φ along the length of the riser at a gas flow rate of 8 m/s and are used for simulation purposes in Chapter 6:

$$k = 0.1\, e^{-0.41z} \tag{5.14}$$

$$\varphi = 0.95 + (0.55 - 0.95) e^{-0.74z} \tag{5.15}$$

These expressions are adequate as a first approximation for larger scale equipment. Lower values of 'k' indicate greater gas bypassing and should be used for conservative estimates. The work of Brereton et al. (1988) suggest values of 'k' in the range of 0.08 m/s for a riser 152 mm in diameter and 9.1 m high. The effect of varying the value of the cross-flow coefficient on butane conversion is discussed in Chapter 6. Large values of 'k' correspond to excellent uniform radial concentrations. In the lean zone, the lower cross-flow coefficients would indicate poor radial mixing.

The core/annular model characterizes the gas flow behaviour well. Further work is required at different gas velocities, solids circulation rates, particle diameters and reactor diameters to generalize Equations (5.14) and (5.15). Gas RTD studies are very useful as analytical tools, but great attention must be devoted to the experimental method in order to minimize systematic errors.

5.2 SOLIDS RTD

The solids residence time distribution analysis is somewhat more involved than the gas RTD. Not only are the solids heterogeneously distributed axially and radially, but the hydrodynamics depend on particle characteristics such as density, diameter and sphericity. Furthermore, the solids injection technique is more difficult to characterize because neither is the input function a bolus nor does the time at which the analyzer starts counting correspond to the time at which the tracer enters the reactor. To quantify these factors, pseudo-single particle experiments were performed and the results compared with established physical principles. In particular, the contribution to the variance of the injector is estimated as well as the injection time and the effect of particle acceleration.

5.2.1 Pseudo-single particle hydrodynamics

Research concerning fluid resistance to falling bodies dates back to Sir Isaac Newton (1717). Newton's experiments involved timing the descent of hollow glass spheres and hog bladders from the dome of St. Paul's Cathedral (London) at a height of 80 m. Since that time, a number of researchers have considered the effect of different materials and heights under various conditions. The most extensive study is that of Lunnon (1926) who presents data for the terminal velocity and acceleration effect of steel, wood, rubber and stone spheres. These experiments were conducted over distances up to 568 m in coal mine shafts. Despite the long lengths, Lunnon notes that the heaviest steel balls continue to accelerate after 320 m. More recently, Rose and Duckworth (1969) detail particle acceleration in pneumatic conveying. Their results indicate that the length required to accelerate sand particles (d_p=0.275 mm) in a riser 0.0828 m in diameter is on the order of 19 m.

The analysis of single particle motion is less complicated than that of suspensions; three principal forces that act on the particle are: (1) the force of gravity, F_g; (2) the buoyant force, F_b; and (3) the drag force, F_d. The acceleration of a particle in a moving stream is derived from a force balance,

$$m \frac{dV_{sl}}{dt} = F_g - F_b - F_d \tag{5.16}$$

where, V_{sl} is the relative velocity between the fluid and particle. The drag force is,

$$F_d = C_d V_{sl} \rho A_p^{2}/2 \tag{5.17}$$

and for particles in the intermediate range (McCabe and Smith, 1976),

$$C_d = 18.5/Re_p^{0.6} \tag{5.18}$$

Buoyancy is negligible in gas-sand systems. Substituting in the force of gravity, the drag force and dz/V_{sl} for dt in Equation (5.16) gives,

$$V_{sl}\frac{dV_{sl}}{dz} = g - 13.9\,\frac{\mu^{.6}\rho^{.4}V_{sl}}{\rho_p d_p^{1.6}} \tag{5.19}$$

Equation (5.19) is easily solved using the numerical technique outlined in Section 3.3. The variation of the particle velocity with distance for three diameters at a superficial gas velocity of 5.95 m/s is illustrated in Figure 5.5. The distance required to reach a steady state velocity increases for larger diameter particles and at higher riser gas velocities. A distance of 0.88 m is sufficient to

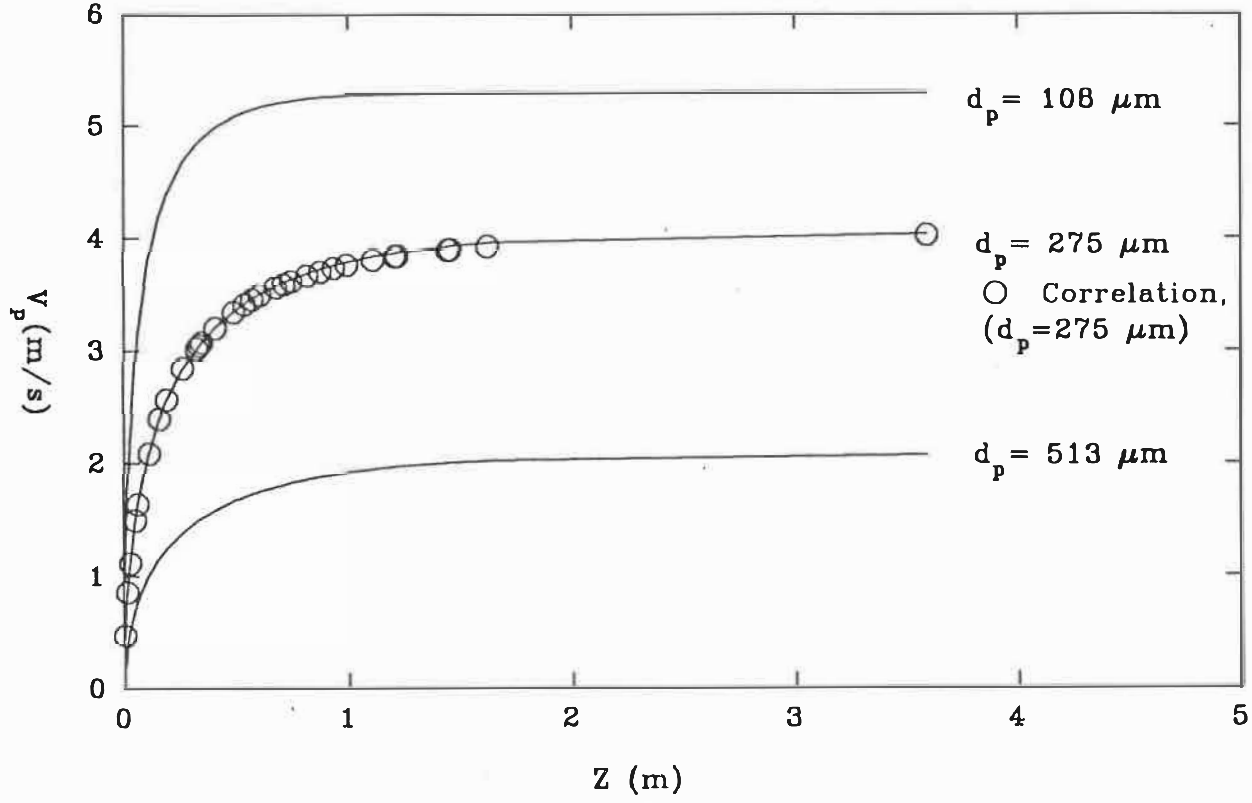

Figure 5.5: Particle acceleration in an empty column, V_g=5.95 m/s

accelerate solids 0.108 mm in diameter to 99% of the terminal velocity at riser velocities of 6 m/s, whereas, distances over 2.7 m are required for particles 0.513 mm in diameter. The following expression is proposed to correlate the particle velocity:

$$V_p \quad = \quad V_t(1\text{-}\exp(az^b)) \qquad (5.20)$$

where 'b' is approximately equal to 0.6 and 'a' ranges from a value of -6 at low gas velocities and small particle diameters to -1.5. Predictions from the correlation are compared with the simulation in Figure 5.5 for d_p=0.277 mm. A value of 0.6 was taken for 'a' and -2.7 for 'b'.

Equation (5.20) applies to discrete particles in an infinite continuum. The actual experimental method consists of injecting a 10 g sample into a stream of air. To model the experimental behaviour, the dispersion equation (Levenspiel and Smith, 1957) is modified to read,

$$\frac{\partial C}{\partial t} + \frac{\partial}{\partial z}(V_p C) = D\frac{\partial^2 C}{\partial z^2} \qquad (5.21)$$

where, V_p is the particle velocity given by Equation (5.20).

The injection pulse input function is not as easily expressed mathematically as for the gas injector input function. High injection pressures propel the radioactive sample into the riser in a reasonably tight packet as a bolus. However, the accompanying influx of air perturbs the system significantly. Therefore low injection pressures are preferred. Unfortunately, the sand does not enter as a concentrated packet. In fact, the solids exit the injector as a continuous stream. Figure 5.6 illustrates the variation of the injector pressure drop with time. The short square curve demonstrates the pressure drop in the absence of sand. The pressure drop increases to a maximum value and remains constant for approximately 0.2 s before finally decreasing. The response of the detector with sand is slightly different. The curve is notably narrower and taller. Furthermore, there is no plateau. Evidently, the sand issues from the injector only after a minimal valve opening, reaches a maximum when the ball is in line with the valve housing before finally decreasing. This isosceles triangular input function, described by Sternberg (1966) as unrealistic for chromatographic purposes, has first and second moments given by Equations (5.22) and (5.23):

$$\mu = \tau/2 \tag{5.22}$$

$$\sigma^2 = \tau^2/24 \tag{5.23}$$

where, τ represents the base width, i.e. the time when the sand first starts to exit to when it stops moving. The experimental variance, calculated from Equation (3.30), equals 0.00337 s^2 which is close to a value of 0.00296 s^2, the variance calculated from Equation (5.23). The base width depends on the reaction time of the operator of the solids injector. The base width, τ, may vary from 0.28 s up to 0.5

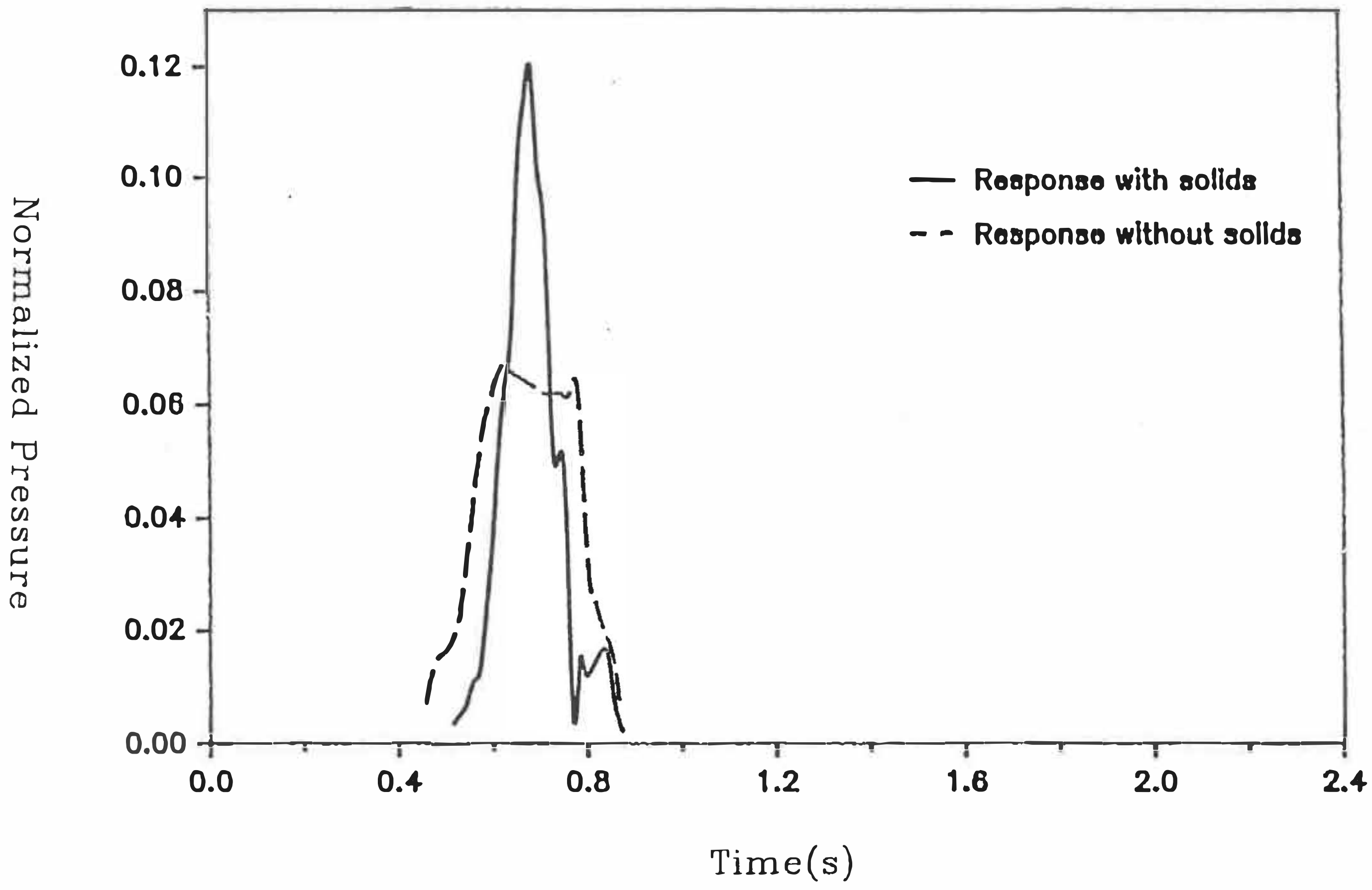

Figure 5.6: Solids Injector Normalized Pressure Variation

s. To reduce the error in the uncertainty of τ, tests were conducted in which the valve was left open. Unfortunately, the input function changes, and it is no longer a simple isosceles triangular function. Solids continually issue from the injector producing a long tail which complicates the analysis tremendously.

To complete the injector analysis, it remains to determine time zero, t_0. The counting mechanism of the analyzer begins when the solids pass in front of the photo-diode, 120 mm upstream of the column. The dead time is the time it takes for the radioactive sand to travel the 120 mm. It is not easily measured but can be estimated by shooting sand into the atmosphere from a known height and measuring the horizontal distance traveled which is related to the tip velocity. The tip velocity depends on the injection pressure and varies with the riser gas velocity. At a riser velocity of 8 m/s the injection pressure is 30 Pa whereas it is only 14 Pa at a riser velocity of 4 m/s. For a riser velocity of 8 m/s, the dead time is less than 0.05 s and it is less than 0.1 s for a velocity of 4 m/s.

In Figure 5.7, the response to an impulse of solids is demonstrated for a riser gas velocity of 6 m/s of two detectors positioned at 0.86 m and 3.89 m for three particle diameters. Unfortunately, due to excessive overlap in which both detectors see radioactive sand simultaneously, the experimental procedure entailed detecting at one height at a time. Slight variations in the riser gas velocity makes

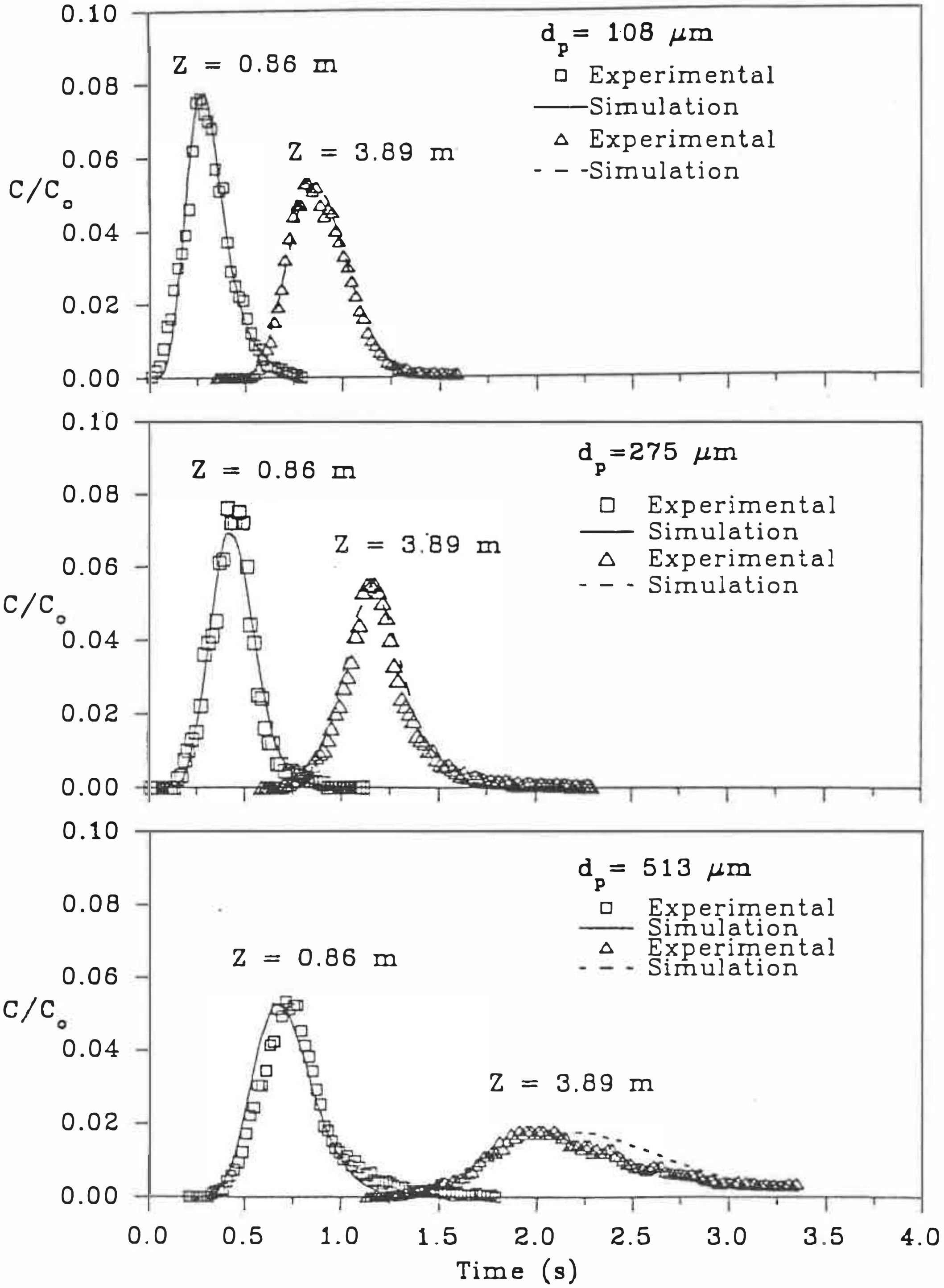

Figure 5.7: Empty Column Particle RTD, U_g=6 m/s

direct comparison between the RTD of the two detectors difficult. Results from the model (Equation 5.21) are given as the smooth curves. The dead time and first moment of the input function were lumped together. A summary of the values used together with the dispersion coefficient is presented in Table 5.6. To minimize numerical dispersion 400 grid blocks and 1000 time steps were used for all calculations.

Table 5.6: Empty Column Solids Dispersion in a Turbulent Air Stream

d_p (μm)	V_g (m/s)	L (m)	V_s (m/s)	τ (s)	Pe
108	6.20	0.86	4.91	0.3	3
108	6.07	3.89	5.27	0.3	59
108	5.2	3.89	4.45	0.4	173
275	6.36	0.86	3.35	0.36	14
275	6.07	3.89	3.86	0.40	150
513	6.03	0.86	1.55	0.30	13
513	6.06	3.89	2.01	0.30	39
108	7.0	3.89	6.1	0.35	237
277	7.8	3.89	5.3	0.3	137
513	7.8	3.89	3.4	0.35	88

The experimental results demonstrate that an isosceles triangle with a base width between 0.3-0.4 s is a reasonable assumption for the input pulse function. However, a constant dispersion coefficient is not a good assumption. Moreover, the dispersion contribution of the injection pulse is of the same order of magnitude as the dispersion coefficient rendering a precise analysis difficult. The Pe number is greater at higher gas velocities and increases at increasing distances from the injection point. The solids dispersion is attributable to fluid turbulence as well as the particle size distribution of the injected sample of sand. The following size ranges were used: 120/170 mesh, 50/60 mesh and 30/40 mesh. Only the size of the injected radioactive sample was tested and not the effect of changing the size distribution of the entire solids inventory. At gas velocities much higher than the terminal velocity of the largest particle an arithmetic mean diameter is a good approximation for the sample. The maximum and minimum terminal velocity of the 50/60 mesh sand is 1.7 and 2.1 m/s with an average of 1.9 m/s. The poor fit to the experimental data of sand 0.513 mm in diameter, plotted in Figure 5.7, is a result of the large spread between the maximum and minimum particle terminal velocities which are 3.1 and 4.6 m/s respectively. On average, the smallest particles reach the second detector, positioned 3.89 m above the injector, 1.5 s before the largest. The difference in transit time to reach the first detector, at a height of 0.86 m is only 0.4 s. The long tail shown in Figure 5.7 is a consequence of the large spread in particle diameter of the sand sample.

Many factors must be considered before attempting to analyze the solids phase RTD in CFB risers. The effect of solids acceleration is most significant for particles whose terminal velocity is near the riser gas velocity. The contribution to the first and second moments of the input pulse increases the closer the detector is to the injection point. Finally, a narrow size distribution of particles is necessary to minimize additional dispersion effects introduced by differences in particle terminal velocities.

5.2.2 Dilute Phase Transport

The CFB riser is characterized by two hydrodynamic regimes: a dense region at the solids entry and a dilute region above. The lean region is often compared to the freeboard region of fluidized beds. Most investigations of this zone employ intrusive probes which may disturb the flow suspension. Non-intrusive optical methods have been successfully used to measure particle velocities in small tubes (Matsumoto et al., 1986). However, these methods are most effective for large d_p/D ratios and would be difficult to apply to CFB risers in which clustering and downflow along the wall occur.

Acceleration effects are readily calculated from a simple force balance for single particles in a flowing fluid. Velocity profiles are not as easily determined for dilute suspensions. Velocity gradients around the particle vary because of the proximity of adjacent particles which affects the drag force. The analysis is further complicated by the formation of clusters and a dense annular region at the wall.

Ambler et al. (1990) and Kojima et al. (1989) have examined the fast fluidization regime using tracer particles. In the former study, radioactive particles were used, whereas in the latter tracer particles were tagged with a fluorescent dye. The data collected by Ambler (1988) is difficult to analyze because the radioactive signal seldom returned to the base line. Kojima et al. (1989) studied FCC particles at low gas velocities (less than 2 m/s). However, the bimodal peaks reported are similar to those obtained in this study.

RTD curves for particles 108 μm in diameter injected at the base of the riser operating at a gas velocity of 4.3 m/s and a solids mass flux of 28 kg/m^2s are shown in Figure 5.8. The most curious characteristic of the experimental data is the bimodal distribution of the curve with 108 μm particles; two peaks are clearly evident. These peaks could be explained either by the presence of a dense annular ring of solids with mass transfer between the core and the annulus or by the flow pattern at the solids entry point. As illustrated in Figure 4.1, the flow pattern in the tee changes with solids circulation rate. At low mass fluxes, the solids are accelerated

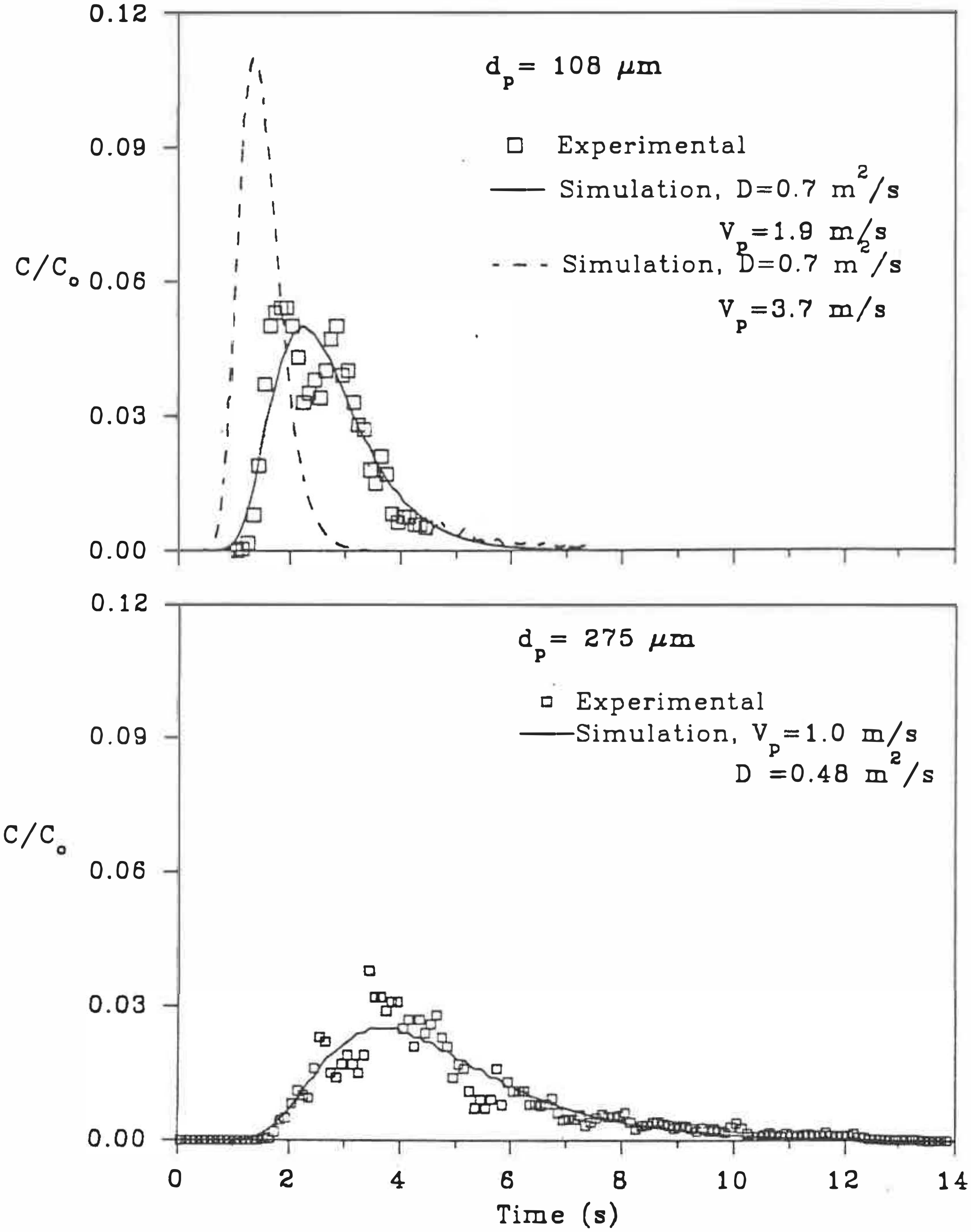

Figure 5.8: Dilute Phase Transport Solids RTD;
U_g=4.4 m/s, G_s=28 kg/m^{2}s

immediately upon entering the tee. At fluxes above 12 kg/m^{2}s, some of the solids accelerate but another fraction initially descends before eventually accelerating upward. A third potential source of the two peaks is the exit geometry. Particles may get held up in the abrupt exit at the top of the riser.

Modelling the particle RTD in the dilute phase transport regime assuming particles behave similarly to those in straight pipe and ignoring the effect of secondary flow patterns would yield erroneous results as indicated in Figure 5.8. Two models were proposed to explain the solids flow pattern. The tallest curve assumes discrete particles in an infinite continuum. The solids accelerate from 0 m/s to 3.67 m/s, the particle steady state velocity. Clearly, the average bulk solids velocity is much less than $U_g/\epsilon - V_t$. The second model assumes that the velocity is a function of the first moment and the dispersion coefficient may be calculated from the variance,

$$V_p = \frac{L}{\mu - \tau_{inj}/2} \tag{5.24}$$

$$D = (\sigma^2 - \tau_{inj}^2/24)\, V_p^3/2L \tag{5.25}$$

where, τ_{inj}, the injection time equals 0.4 s. The average particle velocity is 1.9 m/s, approximately 50 % of the predicted velocity assuming the slip velocity equals the particle terminal velocity. A reasonable fit to the data is obtained with Equation (5.21) and a fitted dispersion coefficient of 0.7 m^2/s.

The RTD of 275 μmm particles is included in Figure 5.8. The experimental velocity based on the first moment is only 1.01 m/s, which is almost half the velocity calculated for solids 0.108 mm in diameter. The fitted dispersion coefficient is 0.48 m^2/s which is somewhat less than the dispersion coefficient for the smaller particles.

In Table 5.7, results are presented for the dispersion of dilute suspensions. The range of solids circulation rates tested was narrow. Differences between the Peclet number for two sizes of particles at gas velocities between 4 and 6 m/s are small. An average Peclet number of 12 could reasonably correlate the data. The average particle velocity is approximately half the predicted velocity assuming the slip velocity equals the particle terminal velocity. The dispersion coefficient is much greater than that obtained for particles in an infinite continuum. For example, at 6 m/s the average dispersion coefficient at 0.8 m^2/s is obtained for particles in a dilute suspension. For the same conditions in an empty column the dispersion coefficient over a length of 3.9 m is only 0.1 m^2/s. The large extents of dispersion are a result of either secondary flow patterns, such as internal recirculation, or dead zones. Part of the sand is immediately accelerated upon entering the riser and another part descends before eventually accelerating vertically. Another contribution to the dispersion is the exit effect. These experiments were conducted with the detector positioned in the horizontal section between the riser and the cyclone.

Brereton (1988) suggests that there is a significant amount of internal recirculation at the top of the riser which would contribute the experimental dispersion.

Table 5.7: Dispersion of gas-solid dilute suspensions, L=4.72 m

d_p (μm)	U_g (m/s)	$U_g - V_t$ (m/s)	V_s (m/s)	D (m_2/s)	Pe	Gs ($kg/m^2 s$)
108	4.32	3.67	1.9	0.7	13	28
275	4.23	2.33	0.99	0.34	14	25
275	4.37	2.47	1.0	0.48	10	28
275	6.32	4.42	2.0	0.91	10	36
275	5.94	4.04	2.1	0.67	14	31

Low solids velocities imply internal recirculation and perhaps long acceleration distances. Therefore, models assuming slip particle velocities equal to the particle terminal velocity are seriously in error,

$$V_p \neq V_g - V_t \tag{5.26}$$

A constant Pe number of 12 approximates the results reasonably well.

However, the most significant parameter is not the dispersion but the solids velocity.

5.2.3 Global Solids RTD

The global solids RTD in the riser was measured by injecting tracer at the base and detecting the signal in the horizontal section between the cyclone and riser. Typical results are shown in Figures 5.9 and 5.10. A number of operating conditions and particle diameters were considered and are summarized in Table 5.8. The curves consist of large fluctuations resembling the riser pressure variation. Figure 5.9 compares the RTD of three particle diameters, d_p=0.513 mm, 0.275 mm and 0.108 mm, at similar operating conditions; U_g=4.2 m/s and G_s=45 kg/m^{2}s. The velocity of the smallest particles is greater than that of the largest particles. Moreover, the fluctuations in the RTD curve are less violent. The average velocity for the small particles, based on the first moment, was 0.63 m/s compared to an average velocity of 0.22 m/s for particles 0.513 mm in diameter. Considering the terminal velocity of the smaller particles is over 3 m/s than that of the larger particles the spread in mean velocity under operating conditions is not significant and indicates that elutriation (i.e. the preferential entrainment of smaller particles) is not large. The variation in Peclet number is small and ranges from 5.2 to 4.5 at a velocity of approximately 4.2 m/s.

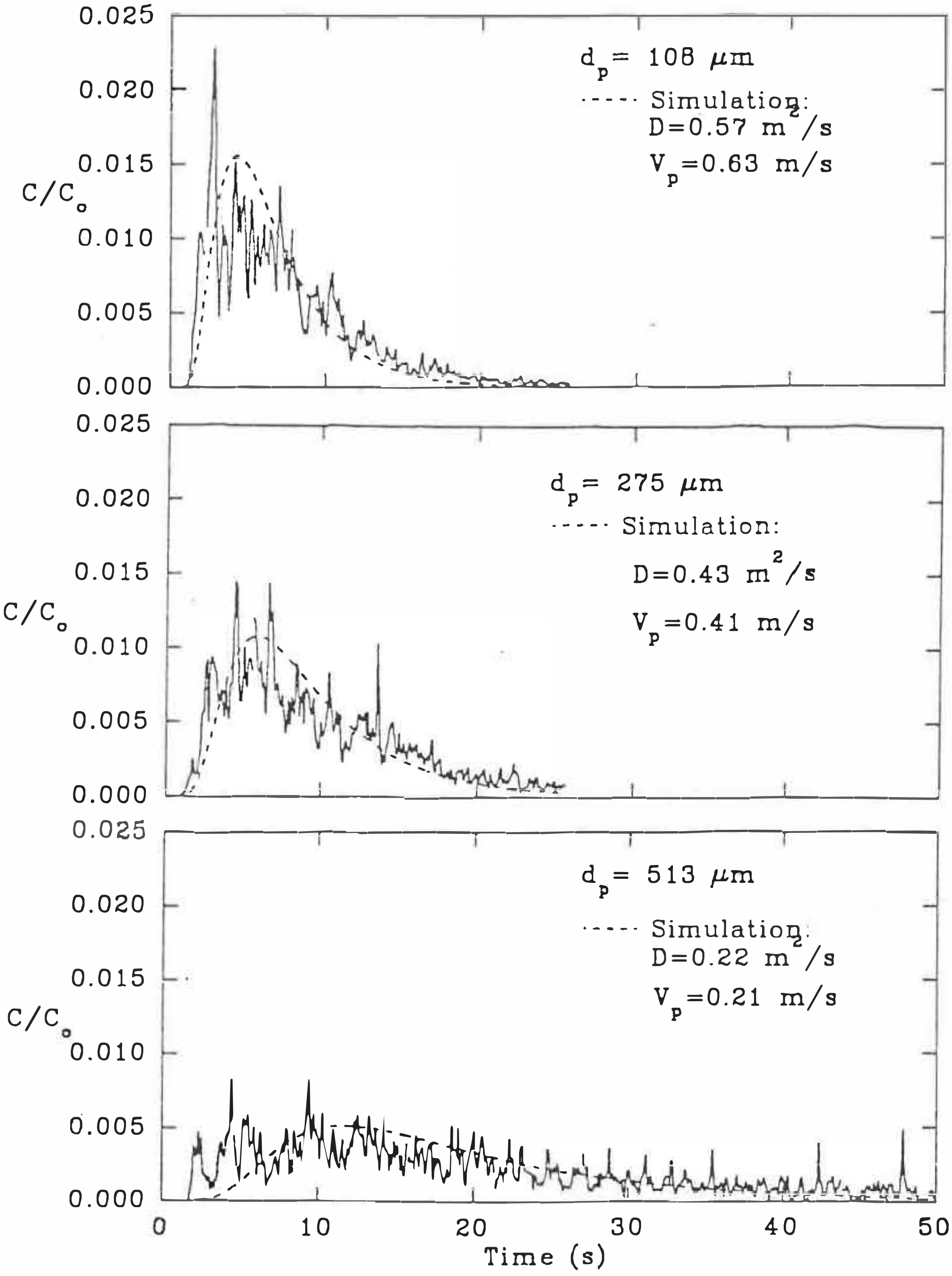

Figure 5.9: Global Solids RTD; U_g=4.2 m/s, G_s=45 kg/m^{2}s

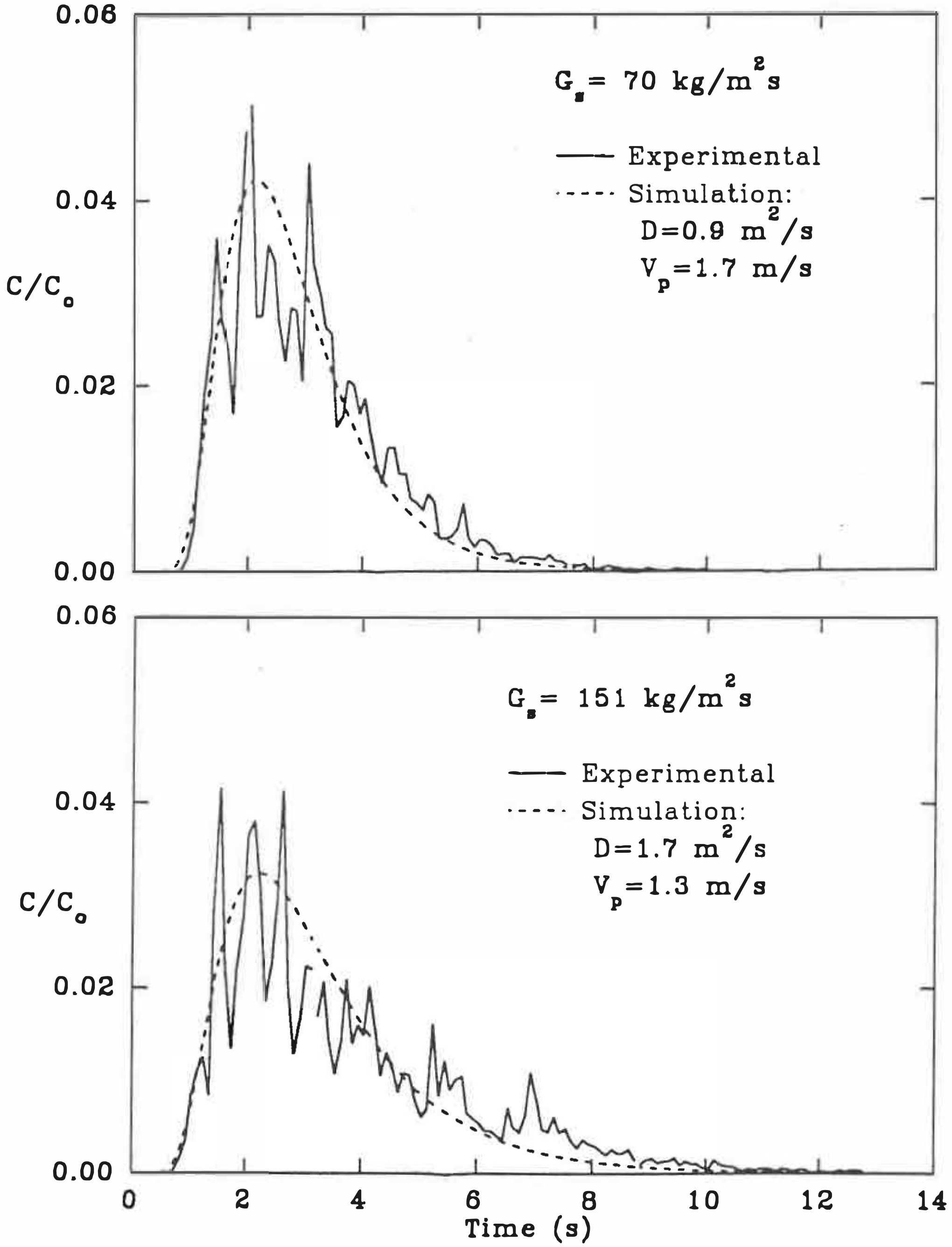

Figure 5.10: Solids RTD at high mass fluxes; U_g=6.0 m/s d_p=275 μm, V_t=1.9 m/s

Figure 5.10 demonstrates the effect of increasing the solids circulation rate at a constant superficial gas velocity of 6 m/s. Generally, the average solids velocity decreases with an increase in G_s as do the maximum peak heights. The Peclet number also decreases with an increase in mass flux. Typically, Pe=8 at a mass flux of 70 kg/m^2s and ranges between 3.5 to 4.8 at mass fluxes greater than 150 kg/m^2s.

Table 5.8: Global RTD, L=4.72 m

U_g (m/s	G_s (kg/m^2s)	d_p (mm)	V_s (m/s)	D (m^2/s)	Pe
4.1	42	108	0.63	0.57	5.2
4.1	50	275	0.44	0.43	4.8
4.3	45	275	0.41	0.39	5.0
4.3	40	513	0.21	0.22	4.5
6.0	70	275	1.7	0.90	8.9
6.1	70	275	1.5	0.92	7.7
5.8	99	275	1.34	1.12	5.6
5.9	99	275	1.62	1.65	4.6
6.2	151	275	1.32	1.67	3.5
6.1	166	275	1.24	1.23	4.8

Yerushalmi and Avidan (1985) review axial dispersion of fluid cracking catalyst. At low gas velocities and circulation rates effective dispersion coefficients range between 0.02 and 0.05 m^2/s. The dispersion is shown to increase with gas velocity and circulation rate. Peclet numbers typically range between 5 and 20 and are also reported to increase with U_g and G_s. For example, at a solids flux of 140 kg/m^2s and a superficial gas velocity of 5.5 m/s Pe=20, while Pe=7.5 at a gas velocity of 3.4 m/s and a mass flux of 75 kg/m^2s. The trends found in this study are in general agreement with that reported by Yerushalmi and Avidan (1985). Differences in the results may be attributable to the type of particle used and/or geometry of the riser considered.

As indicated in the dilute phase study, the slip velocity is greater than the particle terminal velocity. However, the figures demonstrate that some of the solids are entrained at high velocities. Break-through times are reasonably short and correspond to slip velocities higher than particle terminal velocities. The match between the experimental data and the dispersion model is generally good but the model should not be considered physically representative of the flow phenomena. Recirculation at the base of the reactor and at the abrupt elbow at the exit contribute to the effective dispersion and mask the true identity of the solids phase behaviour. To better understand the nature of the flow patterns, it is preferable to measure the radioactive signal at a number of locations along the length of the reactor.

In Figure 5.11, the variation of the residence time with solids circulation rate and gas velocity is shown. At superficial gas velocities of 4 m/s, small increases in the circulation rate increase the residence time significantly. This result is valid for both large and small particle diameters. The effect of increasing the circulation rate is less significant at higher superficial gas velocities.

5.2.4 Lean Phase RTD

The solids movement above the dense region was studied under typical operating conditions. Tracer is introduced 1.56 m above the distributor and detected either at a height of 3.99 m or 0.96 m. The experiments were designed to quantify the core-annular model, as well as the nature of the flow pattern and solids velocity in the lean zone.

In the hydrodynamic model proposed by Berruti and Kalogerakis (1989), a core-annular flow model is postulated. The dense annulus is assumed to descend along the wall at a velocity close to the single particle terminal velocity. Glicksman (1988) reports that particles injected horizontally into a turbulent air stream fall along the wall and within 0.15 to 0.20 m of the injection point reach a constant velocity between 1.2 and 2.0 m/s before eventually breaking up. Rhodes (1990) assumes that the downflow velocity along the

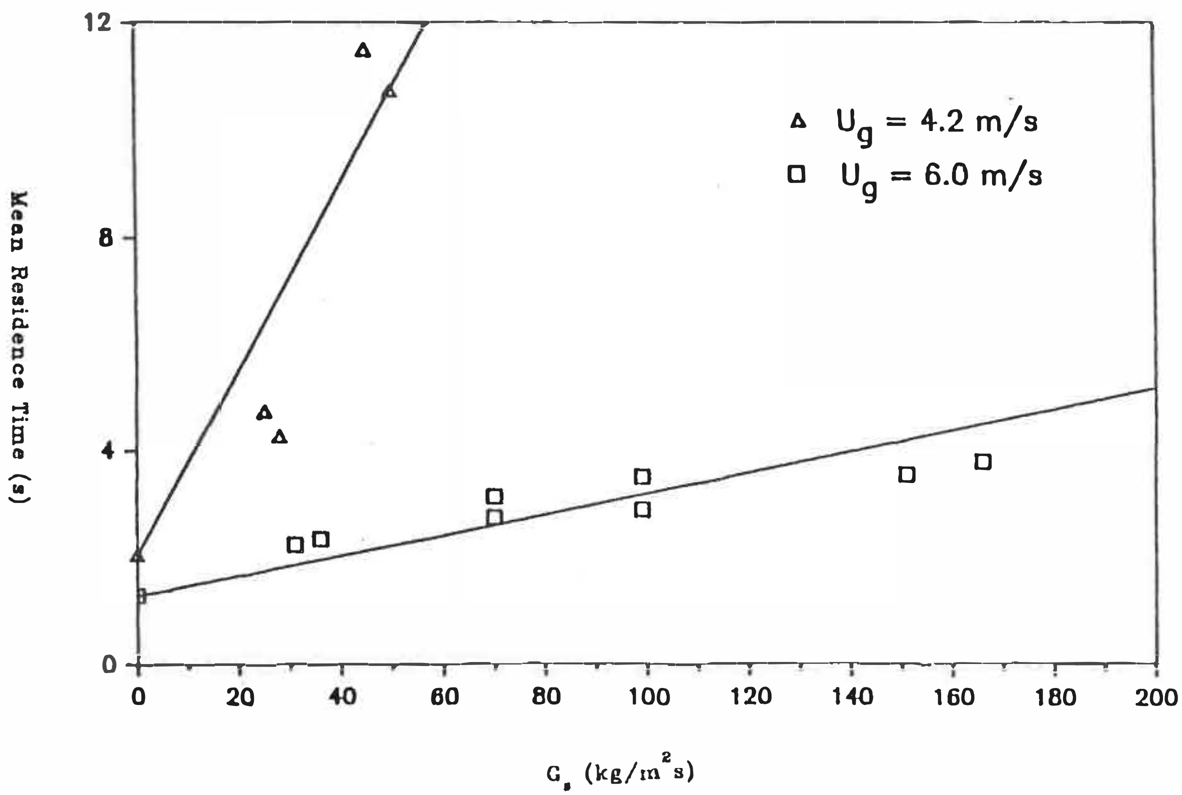

Figure 5.11: Solids Residence Times, d_p=275 μm

wall of risers may be calculated by a force balance involving the gravitational term and wall frictional forces. Based on visual observations, Rhodes (1990) takes the annular wall velocity to be 0.2 m/s.

The solids wall velocity must certainly depend on the particle properties, mass flux and gas velocity. A simple experiment was performed to obtain an order of magnitude of the annular particle velocity. In Figure 5.12, the response to an impulse of radioactive tracer is illustrated when the detector is positioned 0.6 m underneath the injection point (located 1.56 m above the distributor). The radioactivity is first detected 1.5 s after being injected which corresponds to a velocity between 0.4 and 0.5 m/s. Tracer injected at a similar mass flux and a gas velocity of 8 m/s was not detected indicating the drop distance is shorter at higher velocities, confirming Glicksman's results.

Figure 5.13 shows results conducted with 275 μm diameter tracer particles at a gas velocity of 8 m/s and three solids fluxes. Two peaks are evident in each of the three curves in which the first peak is much taller than the second. The second peak is a mere soupcon at a circulation rate of 86 kg/m^{2}s and increases in magnitude at higher rates. The experimental mean velocity, calculated based on the first moment, decreases with an increasing mass flux. At a flux of 160 kg/m^{2}s, V_p=3.2 m/s compared with V_p=5.5 m/s at a flux of 86 kg/m^{2}s.

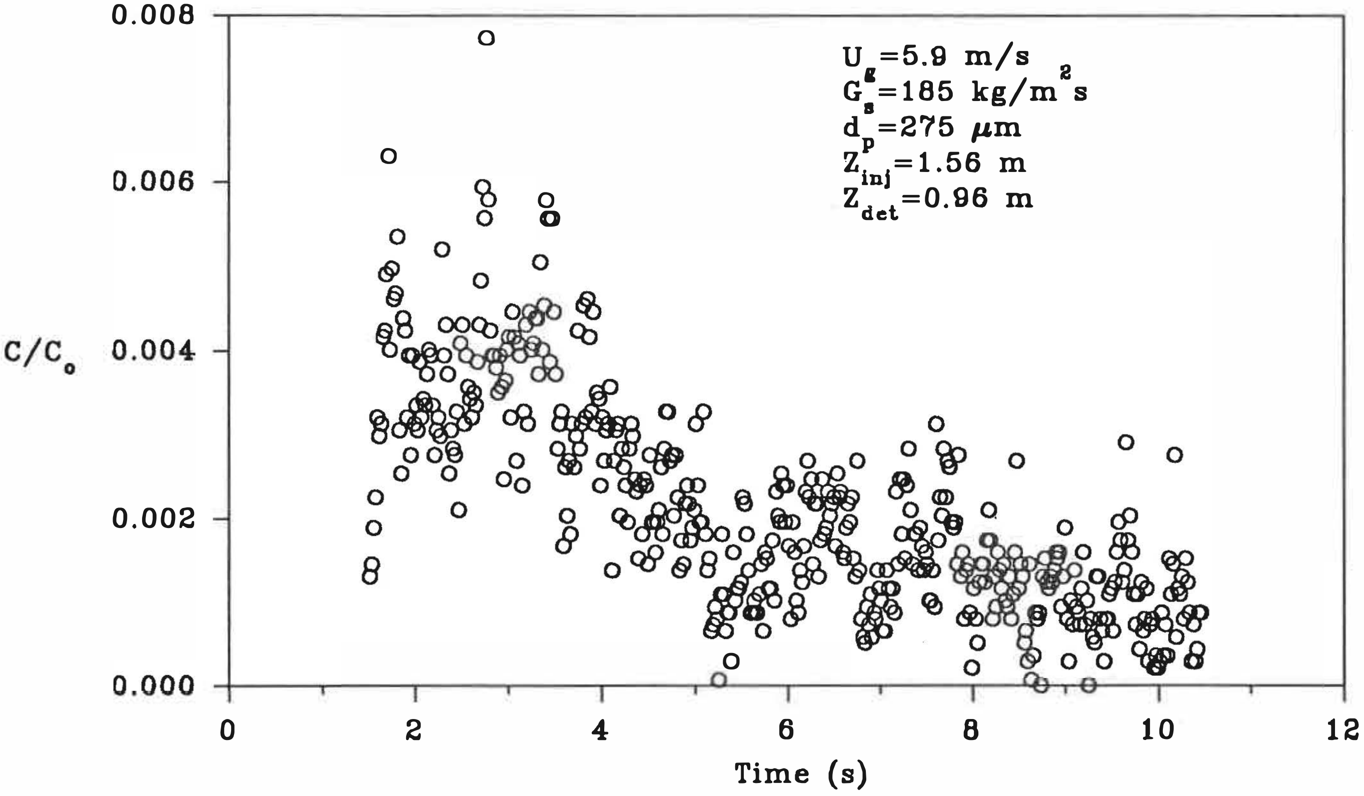

Figure 5.12: Annular Wall Solids RTD

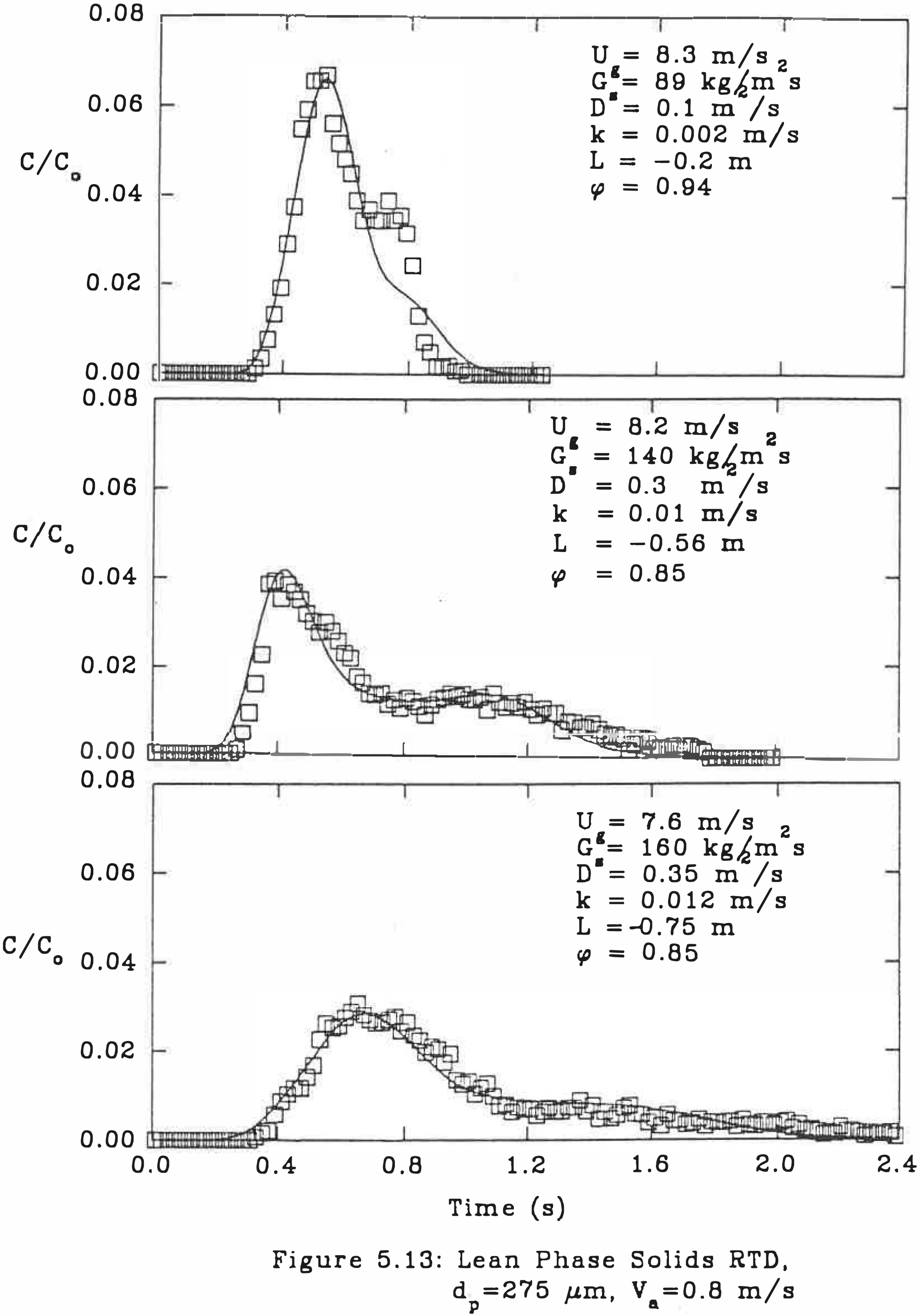

Figure 5.13: Lean Phase Solids RTD, d_p=275 μm, V_a=0.8 m/s L_{inj}=1.75 m, L_{det}=3.99 m

However, this large variation in mean velocity does not apply to the breakthrough velocity, the time the first tracer particles reach the detector, which is 0.15 s ±0.01s, assuming a constant 0.30 s injection time. Moreover, there is little variation in the time at which the normalized concentration reaches a maximum; 0.38 s at G_s=86 kg/m^{2}s, 0.24 s at G_s=139 kg/m^{2}s and 0.49 s at G_s=180 kg/m^{2}s. The corresponding velocities are 6.4 m/s, 10 m/s and 4.8 m/s, respectively, significantly higher than experimental mean velocities. The character of the first peak is similar at each of the gas velocities tested, only the magnitude changes. The maximum normalized concentration is 0.068 at the lowest circulation rate whereas, $C/C_{o,max}$=0.039 at G_s=140 kg/m^{2}s and $C/C_{o,max}$=0.032 at G_s=180 kg/m^{2}s. In addition, the tail increases with increasing mass flux.

Best fit dispersion coefficients assuming that a one-dimensional single phase axial dispersion model applies are presented in Table 5.9. The dispersion coefficient, D, was obtained from the variance of the experimental curve. The match between the model and experimental results was very poor. Predicted maxima were too low and the curves were too far to the right. A multi-zone model would be more appropriate to characterize the flow phenomena.

The three principal multi-zone models include: (I) core-annular, a lean core region with a dense annulus which flows downward along the wall; (II) stagnant wall, a lean core with mass transfer to a dense wall region that neither flows up nor down; and (III) clusters, dense concentrations of particles that generally flow in the upward direction.

Table 5.9: Lean phase RTD, d_p=0.275 mm

U_g (m/s)	G_s (kg/m^{2}s)	Z (m)	V_p (m/s)	D (m^2/s)	Pe
5.9	197	-0.62	-0.25	-	-
7.9	180	-0.62	-	-	-
8.3	86	2.42	5.5	0.3	44
8.2	139	2.42	4.5	0.6	18
8.3	180	2.42	3.2	1.2	6.5

The nature of the lean and dense zones may be deduced from a cursory examination of the experimental results. Short break-through times and tall narrow peaks indicate bypassing of tracer at high velocities. The long tail and shorter second peak indicate some sort of delay such as localized backmixing, a stagnant wall region, or clusters which rise more slowly due to their large diameter.

The model predictions, illustrated in Figure 5.13 and 5.14, are based on the following assumptions:

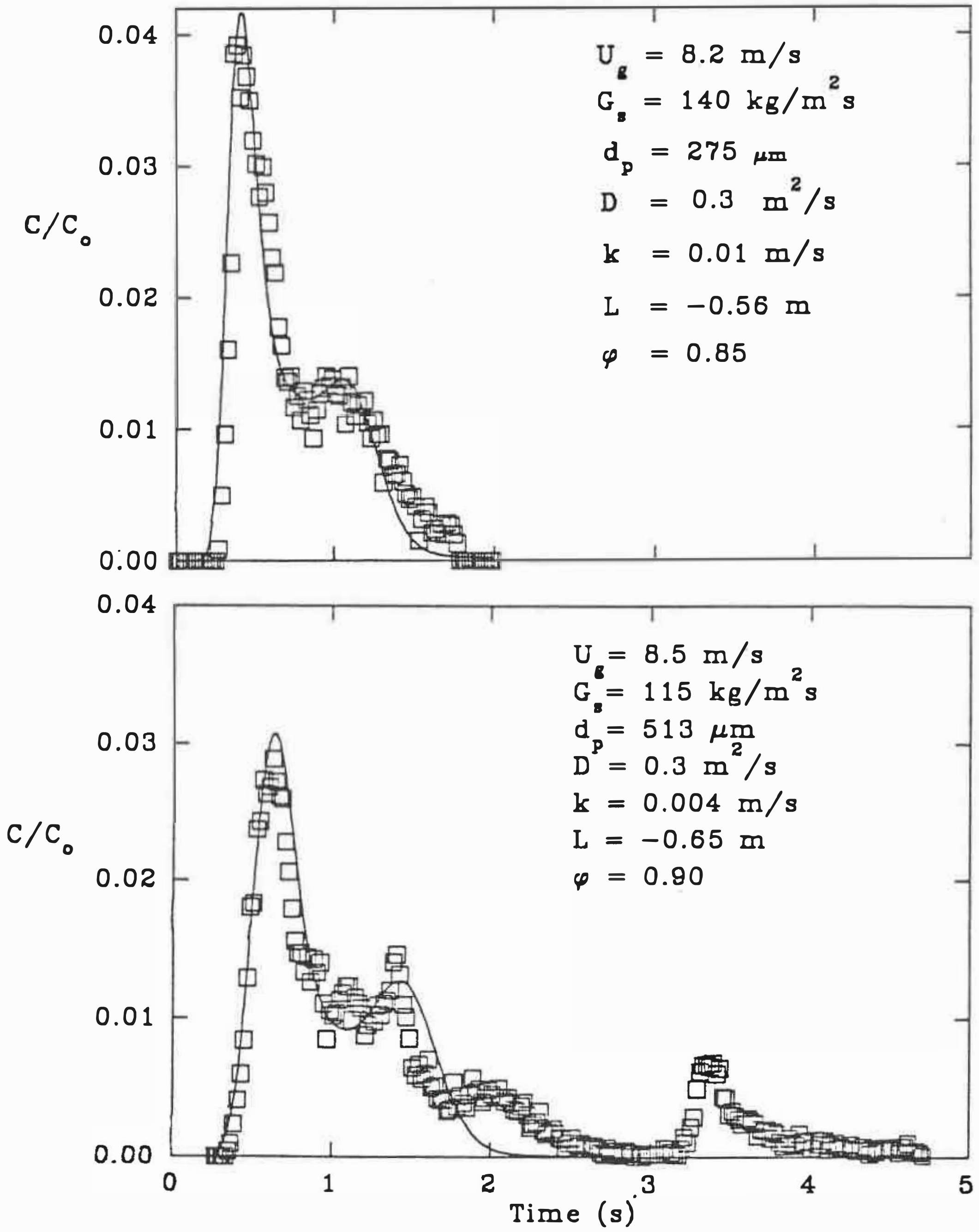

Figure 5.14: Lean Phase RTD, V_a=0.8 m/s

(i) Slip velocities in the core are equal to the single particle terminal velocity.

(ii) Annular regions are equivalent to those determined from the gas phase studies.

(iii) A fraction of the tracer enters the core zone directly and the rest descends along the wall at a constant velocity of 0.8 m/s (a compromise of the literature values discussed above).

(iv) The distance the tracer falls depends on the solids circulation rate and is calculated by comparing the difference in time between the two peaks.

(v) Solid concentrations in the core and annular zones are not considered in the computer simulation.

(vi) The cross flow coefficient is constant along the length as is the dispersion coefficient and φ.

A summary of the parameters used to fit the data is given in Table 5.10. The distance the particles fall, L, increases with an increase in the solids circulation rate, i.e. the residence time of the particles in the annular zone increases with an increase in the circulation rate. Small values of 'k' indicate low mass transfer rates between the core and annular zones. Considering that the core radius is larger (meaning the annular ring is smaller) at lower solids circulation rates the mass transfer rate must also be lower. The particles have less of a tendency to go to the annular region and stay in the core. It is interesting to note that the solids cross-flow coefficients are lower than the gas counter parts. The experimental run with 513 μm tracer particles (Figure 5.14) exhibit peaks at 2 s and 3.5 s. These additional peaks may not be explained by a simple mass transfer mechanism between a core and annulus. Clusters may be more appropriate to explain this behaviour. Multiple peaks were also observed at gas velocities of 6 m/s and 4 m/s.

Table 5.10: Fitted Parameters of Solids RTD in the Lean Region of the Riser, Ug=8m/s

G_s (kg/m^2s)	d_p (μm)	φ	L_{fall} (m)	k (m/s)	D (m^2/s)
89	275	0.94	0.2	0.002	0.1
140	275	0.85	0.56	0.01	0.3
160	275	0.85	0.75	0.012	0.35
115	513	0.9	0.65	0.004	0.3

In the Appendix, the effects of each of the parameters on the predicted RTD curve are studied more quantitatively. The experimental data, shown in Figure 5.13 (U_g=8.2 m/s and G_s=140 kg/m^2s), was chosen for illustration purposes. Three values of the six parameters were varied independently and the resulting RTD predictions are compared against the experimental data. It is interesting to note that the effect of the dispersion coefficient and cross-flow coefficient are similar; low values exaggerate the height of the second peak and large values merge the two peaks into one. It is difficult, if not impossible, to differentiate between the axial dispersion and mass transfer between the two phases based on the studies conducted to the present. Future studies should concentrate on introducing particles in the core and annulus regions separately to be able to further quantify the solids mass transport.

5.2.5 Dense Region RTD

The three graphs in Figure 5.15 compare the RTD in the dense region of the riser operating at a superficial gas velocity of 8 m/s and a solids circulation rate of 210 kg/m^2s. Peak maxima are significantly lower than for the lean zone studies. In addition, the tails are much longer and multiple peaks observed at lower gas velocities in the lean zone are evident even for 108 μm particles. The first series of experiments involves injecting tracer 0.1 m above the distributor and detecting at 0.92 m. A second set of measurements was made in which the tracer was detected at 3.99 m.

Constant cross flow coefficients were inadequate to describe the long tails, so unequal values of k were used. Physically, this suggests that the transfer of solids from the annulus to the core is less than that in the lean region. Fitted cross-flow coefficients from the core to the annulus are greater than in the lean region.

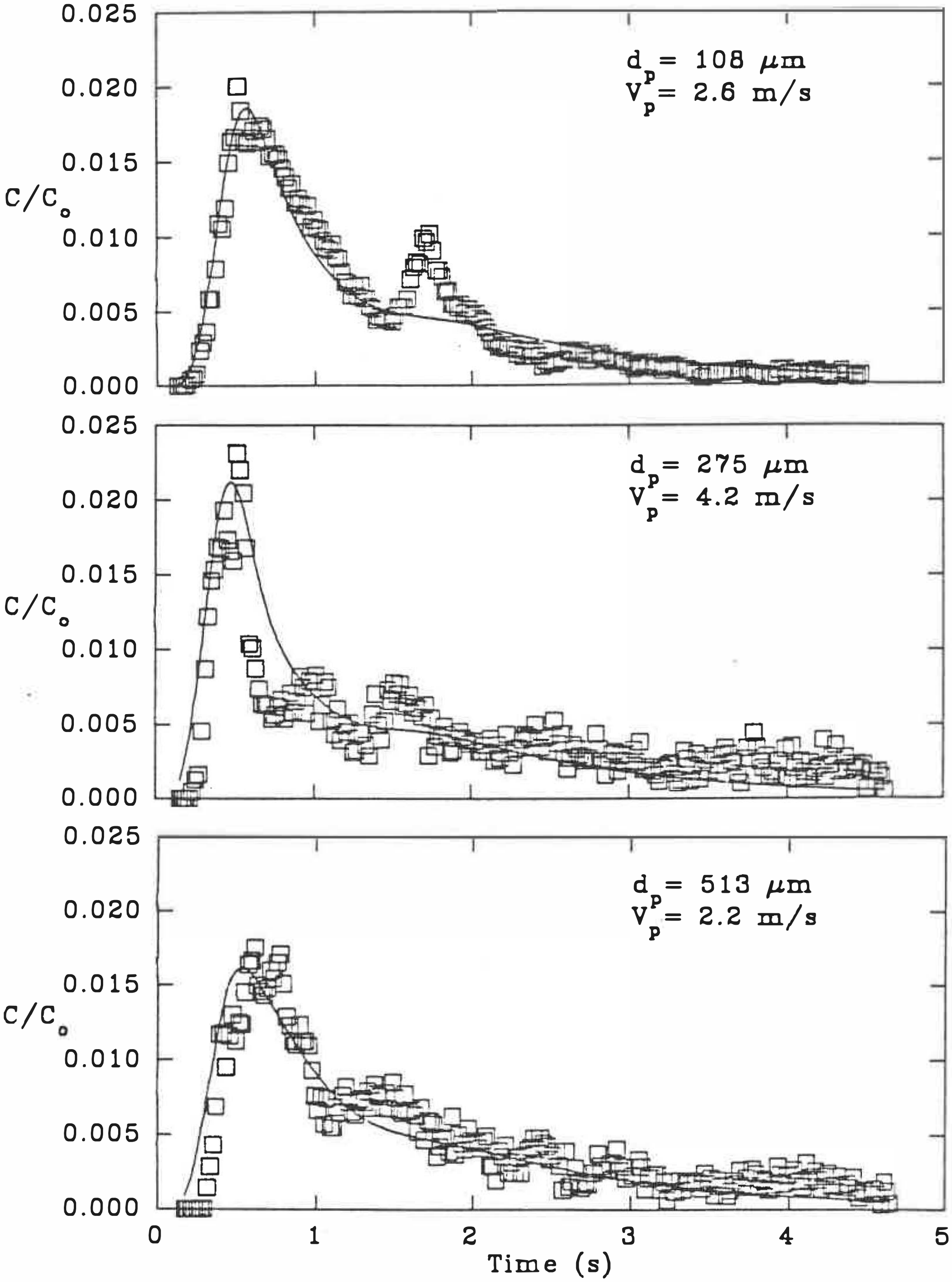

Figure 5.15: Dense Phase Solids RTD, U_g=8 m/s, G_s=210 kg/m^{2}s D=0.5 m^2/s, k_{c-a}=0.002 m/s, k_{a-c}=0.02 m/s, V_a=0.1 m/s L_{inj}=0.1 m, L_{det}=0.96 m

Moreover, the assumed wall velocity of 0.8 m/s was much too large and since the drop distance was constant (0.1 m) the annular velocity was varied to fit the data. Slip velocities in the core equal to the particle terminal velocities were too low and were also fitted. Core velocities in the dense region seemed to be independent of the particle diameter. A velocity of 2.6 m/s fitted the results for 513 μm particles equally as well as for 108 μm particles. The core fraction, φ, was assumed constant at 0.66 and the dispersion coefficient was fixed at 0.5 m^2/s. High cross-flow coefficients were used to simulate the annular break-up on reaching the drop length in the lean zone simulations (k_1=1 m/s). A value of 0.01 m/s was used for k_1 at the distributor. The multiple peaks recorded by the detector at 0.92 m must be the result of strong recirculation patterns in which concentrated particles such as clusters retain their identity through a number of cycles. The magnitude of the second peak is probably a function of the solids distribution at the time of injec-

Table 5.11: Fitted Parameters of Solids RTD in the Dense Region of the Riser, U_g=8m/s

G_s (kg/m^{2}s)	d_p (μm)	$V_{p,a}$ (m/s)	$V_{p,c}$ (m/s)	k_{c-a} (m/s)	k_{a-c} (m/s)
210	108	0.1	2.6	0.02	0.004
210	275	0.07	4.2	0.02	0.004
210	513	0.1	2.6	0.02	0.004

tion as well as the gas velocity. No definite trend is discernable concerning the different particle sizes tested. At the base of the reactor mixing is most probably independent of the particle size.

The differences between the solids RTD for varying particle sizes are more evident with the detector positioned at 3.99 m as illustrated in Figure 5.16. The 513 μm particles are quite dispersed in comparison to the 108 μm particles whose peak is sharper and well defined. Particle velocities decrease with an increase in size at the same reactor conditions. Multiple peaks are not evident. The tail is much longer for the larger particle and the maximum peak height is shorter. Model predictions, illustrated in Figure 5.16, are based on parameters developed for the lean region and dense region results (Tables 5.10 and 5.11). Annular velocities below 0.9 m are assumed to be 0.1 m/s; above 0.9 m a value of 0.8 m/s is taken. Assumed values of φ are taken from the results of the gas phase studies. At a solids circulation rate of 210 kg/m^{2}s φ=0.8. Mass transfer between the two zones is limited to the rate in the dense zone. The same values were used throughout the length of the column as given in Table 5.11. A summary of the principle parameters used to fit the data is presented in Table 5.12. Average particle velocities are significantly greater than those obtained at the base of the riser but are lower than the gas velocity minus the particle terminal velocity.

Reasonable approximations to the overall solids RTD is obtained

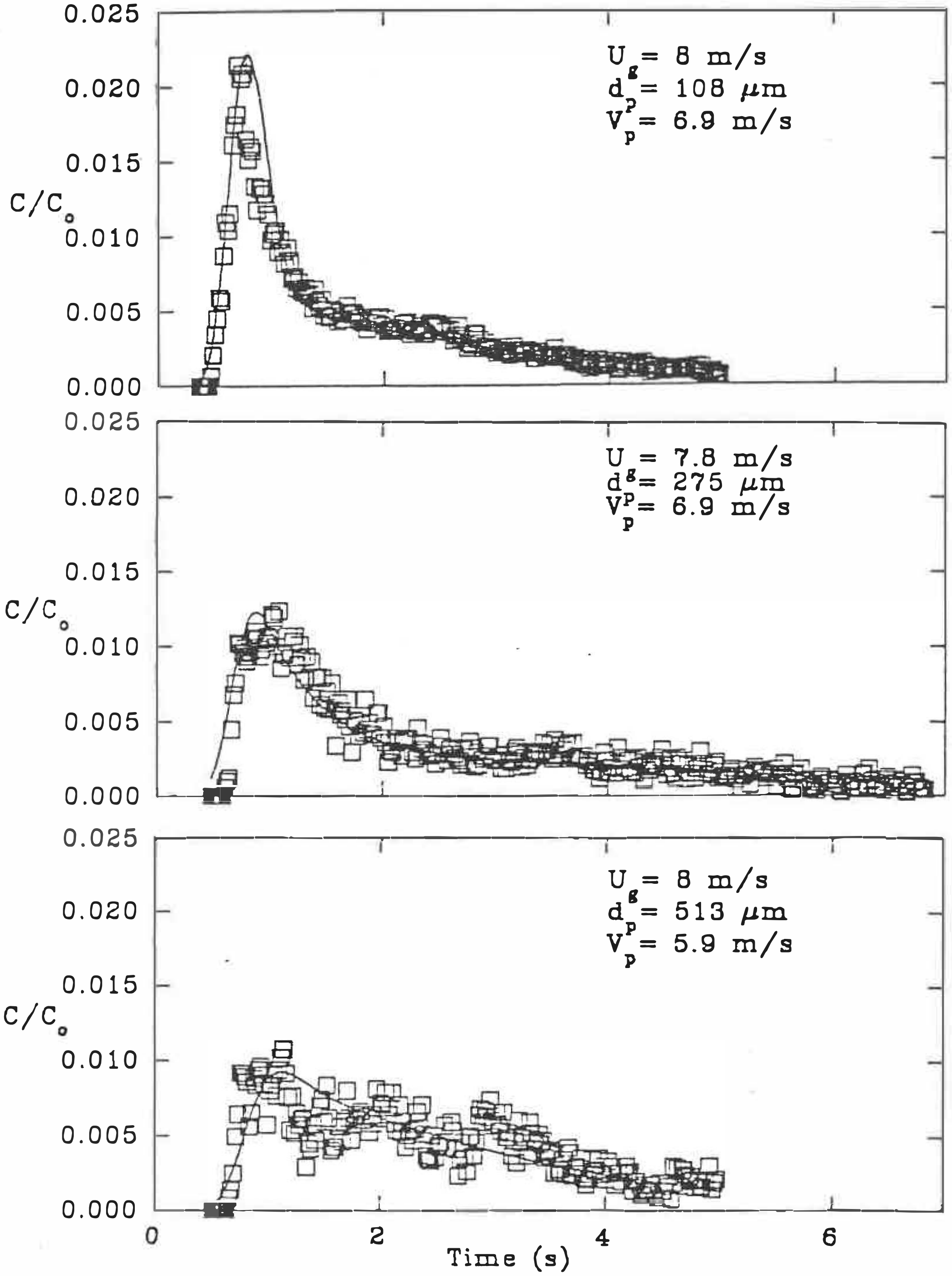

Figure 5.16: Riser Solids RTD, G_s=210 kg/m^{2}s
D=0.5 m^2/s, φ=0.8
L_{inj}=0.1 m, L_{det}=3.99 m

Table 5.12: Fitted Parameters of Solids RTD, Z_{inj}=0.1 m, Z_{det}=4 m Ug=8m/s

G_s ($kg/m^2 s$)	d_p (μm)	D (m^2/s)	$V_{p,c}$ (m/s)	k_{c-a} (m/s)	k_{a-c} (m/s)
210	108	0.5	6.9	0.02	0.004
210	275	0.5	6.9	0.02	0.004
210	513	0.5	5.9	0.02	0.004

with a simplistic one-dimensional two zone dispersion model for the solid. However, considerable evidence is presented indicating the presence of at least two zones and has been approximated by a lean core surrounded by a dense annular region at the wall. The core radius increases vertically as does the annular solids velocity. The solids in the core behave as individual particles but refluxing from the core to annulus, particularly for large particles and at low gas superficial velocities, results in large secondary peaks on the tracer response curves. Particles in the core accelerate over short distances at the solids entry point. The core solids velocities appear to be independent of particle size. The dispersion coefficient decreases with decreasing solids flux. Cross-flow coefficients are lower than for gas exchange. However, it is difficult to differentiate between the effects of dispersion and mass transfer between the core and annulus. In the dense region the k values greater from core to the annulus results in improved fits.

5.2.6 Design Considerations

The following parameters are proposed as a first approximation for design purposes at a riser superficial gas velocity of 8 m/s: (I) The gas is in plug flow with mass transfer between the core and annulus, k_g=0.05 m/s. (II) At high solids circulation $\varphi_{overall}$=0.85. Average values of φ at the base of the column are around 0.66 and 0.9 for the lean zone at the top. (III) Particle residence times in the lean region and dense region of the annulus zone are approximately equal to 1 s. (On the RTD curves, this time is equivalent to the time between the two peaks). Particle velocities along the wall are 0.8 m/s in the lean zone and 0.1 m/s in the dense zone. (IV) The slip velocity is equal to the particle terminal velocity in the core region except in the dense region where the velocity is independent of diameter and equals 3 m/s (approximately $U_g/4\varphi$). (V) The solids mass transfer rate between the two zones is less than the gas mass transfer rate. Values depend on the height above the solids entry point and the particle diameter. For G_s> 150 kg/m^{2}s, $k_{s,c-a}$=0.02 and $k_{s,a-c}$=0.004 m/s in the dense region and $k_{s,c-a}$=$k_{s,a-c}$=0.012 m/s in the lean region. (VI) An average solids dispersion coefficient of 0.5 m^2/s is a reasonable approximation over the length of the riser.

The total particle residence time is calculated based on the sum of the four pseudo regions: (a) the core lean zone, (b) core dense zone, (c) annular lean zone and (d) annular dense zone. The dense zone, (c) annular lean zone and (d) annular dense zone. The following example illustrates the calculation procedure. Consider a gas velocity of 6 m/s at a circulation rate of 150 kg/m^{2}s with a mean particle diameter of 277μm:

$$t_a = \frac{L}{(U_g/\varphi - V_t)} = \frac{3.8}{(6/0.9-1.9)} = 0.8 \text{ s} \tag{5.27}$$

$$t_b = \frac{L}{(U_g/\varphi)/4} = \frac{1}{(6/0.66)/4} = 0.5 \text{ s} \tag{5.28}$$

$$t_c = t_d = 1 \text{ s} \tag{5.29}$$

$$\Sigma t = t_a+t_b+t_c+t_d = 3.3 \text{ s} \tag{5.30}$$

In Figure 5.11 the average residence time of the particle is shown to be approximately 3.8 s, which agrees reasonably well with the rough approximation given by the example. In Figure 4.14, the variation of the longitudinal suspension density along the length of the reactor is compared for different gas velocities and solids circulation rates. For the same solids mass flux the solids hold-up is greater at lower gas velocities. Hence, a one second residence time in the annular regions may be too low. This result is confirmed in Figure 5.12 in which the annular RTD at a gas velocity of 6 m/s is illustrated. At the same solids circulation rates and a gas velocity of 8 m/s the radioactive particles are not detected. Hence, residence times in the annular regions are greater at lower superficial gas velocities.

6. PARTIAL OXIDATION OF BUTANE TO MALEIC ANHYDRIDE

A computational study involving the partial oxidation of butane to maleic anhydride is developed to quantify parameters proposed to model the riser hydrodynamics. In particular, the sensitivity to the assumed core radius, solids concentration in the lean and dense zones as well as the mass transfer coefficient between the two zones are examined. The catalytic oxidation of C_4 hydrocarbons in CFBs has not been commercialized, as of yet, and there is a lack of information concerning the effect of the various phases in the riser on reactor performance.

Maleic anhydride (MA) is an industrially important chemical and its synthesis has undergone many dramatic changes in the last 15 years. "First generation" MA production consisted of multi-tubular fixed bed reactors using benzene as a feedstock. With the development of catalysts capable of partially oxidizing C_4 hydrocarbons a switch from benzene to butane began. Currently most producers in North America use butane as a feedstock compared to 1980 when more than 85% of MA was produced using benzene (Chowdhury and Ushio, 1987). A "second generation" process in which fixed bed reactors are being substituted by fluidized beds is underway. Advantages of higher throughput, better temperature control, and smaller oxygen requirement are cited as reasons for the change (Contractor and Sleight, 1987).

Currently, Du Pont is developing a third generation process for MA production based on circulating fluidized bed reactors (Contractor, 1988). A number of advantages of this reactor have been cited, including: separate catalyst oxidation and reduction zones, high selectivity, low catalyst inventory and concentrated product streams (Contractor and Sleight, 1987). Lower O_2 concentrations in the oxidation zone are permissible because the catalyst is reactivated in the recirculation leg. In fixed and fluid bed processes excess O_2 is a requisite to avoid over reduction and loss of activity.

Presently, the petrochemical industry is dependent upon expensive unsaturated molecules to produce derivative products. Maleic anhydride from butane is the only reaction in which a C-H bond of a saturated straight chain hydrocarbon is activated catalytically producing an unsaturated molecule. Further economic development of this process could render the production of other derivative chemicals, such as 1,4 butanediol, γ-butyrolactone and tetrahydrofuran, viable.

6.1 KINETICS

A knowledge of many diverse fields of science are required to adequately model a catalytic reactor. Heterogeneous catalysis involves the synthesis of organic reactions promoted by inorganic material for which mass and heat transfer must be transferred across phase boundaries. In addition to the requirement of a fundamental understanding of reaction kinetics and thermodynamics, a familiarity with the hydrodynamics of two phase, gas-solid flow is necessary. After having developed a model it is then necessary to solve the resulting equations, requiring a numerical technique for systems to complicated to solve analytically.

A complex reaction sequence has been proposed for the partial oxidation of butane to maleic anhydride for which the principal intermediate products include 1-butene, 1,3 butadiene, crotonaldehyde and furan. Methanol, acetone formaldehyde, formic acid, acetic acid and glycols are among the by-products (Ozkan and Schrader, 1985 a,b,c; Hodnett and Delmon, 1984). The uniqueness of this reaction is attributable to the vanadium phosphorous oxide catalyst. Although its chemistry is well defined and the effects of various preparation methods have been examined (Schneider et al., 1986; Schneider, 1985) the mechanism is not well understood. The problem lies in the fact that in-situ dynamic studies of catalysts are not presently available. Most data collected are measured on a post-mortem or pre-natal basis. Consequently valuable information concerning the active phases during reaction are not available.

Escardino et al. (1973) initially proposed three single pseudo-first-order reactions to model the reaction,

$$C_4H_{10} + 3.5\ O_2 \longrightarrow C_4H_2O_3 + 4\ H_2O \qquad (6.1)$$

$$C_4H_2O_3 + 3\ O_2 \longrightarrow 4\ CO_2 + H_2O \qquad (6.2)$$

$$C_4H_{10} + 6.5\ O_2 \longrightarrow 4\ CO_2 + 5\ H_2O \qquad (6.3)$$

This reaction sequence was found to adequately represent the experimental data for low butane partial pressures and a temperature range between 400-480•C. Wohlfahrt and Hofmann (1980) extended the range of oxygen and butane concentrations, but their results were limited to higher temperatures (450-500°C). Schneider (1985) compared the Mars van-Karmen reaction mechanism to the Eley Ridel for a temperature range of 370-500°C. The Eley-Ridel mechanism was found to fit the data obtained from an optimized catalyst developed in their laboratory. A significant drawback of the reaction sequence proposed by these authors is that they did not allow for the successive combustion of maleic anhydride to CO_2 and CO. They did show, however, that the use of a factorial design of experiments is a very effective tool in optimizing the selectivity and conversion capabilities of catalysts.

In this study, the kinetic model proposed by Centi et al. (1985) is used. The vanadium-phosphorous catalyst developed was found to be very active and selective to maleic anhydride at temperature in the 300°C range. Two pathways for the oxidation of n-butane were proposed. The first pathway, selective in maleic anhydride, was found to follow the Langmuir-Hinshelwood model, depending on the hydrocarbon concentration:

$$r_{MA} = \frac{k_1 \; K_B \; C_B \; C_O^{\alpha}}{1 + K_{BB}} \qquad (6.4)$$

The second pathway, selective in carbon dioxide, was found to be independent of butane concentration,

$$r_{CO2} = k_2 \; C_O^{\beta} \qquad (6.5)$$

The rate of maleic anhydride decomposition was formulated as follows:

$$r_{-MA} = k_3 \; C_{MA} \; C_O^{\gamma}/C_B^{\delta} \qquad (6.6)$$

6.2 MATHEMATICAL MODEL

To simulate the partial oxidation of butane in a CFB riser requires no less than ten equations, one equation for each of the chemical species, C_4H_{10}, O_2, $C_4H_2O_3$, CO_2, and H_2O in each of the two zones. The mass balance equations for the lean core and dense annular region read as follows:

CORE:

$$\frac{\partial (V_g C_{i,c})}{\partial x} + \rho_p (1-\epsilon_c) \varphi \Sigma r_i + \frac{2k}{r_c}(C_{i,c} - C_{i,a}) = 0 \qquad (6.7)$$

ANNULUS:

$$\rho_p(1-\epsilon_a)(1-\varphi)\Sigma r_i - 2kr_c/(R^2-r_c^2)\ (C_{i,c}-C_{i,a}) = 0 \qquad (6.8)$$

The boundary conditions are given by Equations (5.8-9).

The system of equations are expressed in finite difference form and solved numerically using a Newton Raphson iteration scheme. The computer program is included as Appendix A. It was written in a general manner so that any number of coupled partial differential equations (one dimension) may be solved with a minimum of change.

The geometry of the experimental unit is considered for all calculations. A superficial gas velocity of 8 m/s and a circulation rate of 174 kg/m^2s is assumed. The total catalyst inventory, at these conditions, is approximately 1.85 kg and corresponds to an average void fraction of 0.974. Conversions at the conditions, as predicted by the model given by Centi et al. (1985), are typically less than 0.5 % at a temperature of 300 °C. The catalyst developed by these researchers is selective to MA but not very active. Its activity is approximately 50 times less than that of Schneider (1986). This exercise is directed at quantifying the effect of the hydrodynamic parameters of the riser. Therefore, for simulation purposes, a reaction temperature of 500 °C is assumed thus increasing the rate constants. In Table 6.1 the kinetic parameters given by Centi et al. (1985) are summarized together with the simulation values.

Table 6.1: Kinetic Parameters for the Oxidation of Butane and Maleic Anhydride

Temp. (°C)	k_1 (10^{-7}) $\frac{\mathrm{mol}^{1-\alpha}\ell^{\alpha}}{\mathrm{gs}}$	k_2 (10^{-7}) $\frac{\mathrm{mol}^{1-\beta}\ell^{\beta}}{\mathrm{gs}}$	k_3 (10^{-7}) $\frac{\mathrm{mol}^{\delta-\gamma}\ell^{1-\delta+\gamma}}{\mathrm{gs}}$
300	3.357	2.001	0.440
320	4.621	4.364	0.606
340	6.230	9.040	0.966
500	336	200	44

$K_B = 2616\ \ell/\mathrm{mol}$, $\alpha = \beta = 0.23$, $\gamma = 0.63$, $\delta = 1.15$

To quantify the sensitivity of the model parameters, five cases for the solids distribution are considered:

(I) catalyst evenly distributed longitudinally and radially (ϵ=0.974),

(II) single phase exponentially decaying solids distribution ($\epsilon=\epsilon(z)$, Equation 4.25),

(III) two zone model (Brereton et al., 1990; φ=0.86, ϵ_c=0.99, ϵ_a=0.88, k=0.05 m/s),

(IV) two zone model (Berruti and Kalogerakis, 1989; k=0.05 m/s, $\varphi=\varphi(z)$, $\epsilon_c=\epsilon_c(z)$, $\epsilon_a=\epsilon_{mf}$, $V_{p,a}=U_g/\varphi(z)\epsilon_a-V_t$),

(V) two zone model ($\epsilon_a=\epsilon_a(z)$, $\epsilon_c=\epsilon_c(z)$, $\varphi=\varphi(z)$, Equation 5.14

k=k(z), Equation 5.15, $V_{p,a}$=0).

6.3 SIMULATION RESULTS

The predicted butane conversion along the length of the reactor for each of the models is compared in Figure 6.1. The single phase plug flow model (I) with catalyst evenly distributed radially and longitudinally gives the highest butane conversion. The exponentially decaying solids distribution, model II, predicts lower conversion since the gas velocity near the base of the riser is higher. Hence, the gas is in contact with the bulk of the catalyst for a shorter period of time. The two zone model (III) of Brereton et al. (1988) is comparable to model (I) in that longitudinal variations in solids hold-up are ignored. Total butane conversion is lower in the two zone model (III) as a result of the resistance to mass transfer between the core and annulus. Evidently, k values in the range of 0.05 m/s are reasonably high since the differences between the model predictions of (I) and (III) are small. Conversions from models (IV) and (V) are lowest and may be attributable to the low suspension density in the top portion of the riser. The selectivity was not sensitive to the assumed solids distribution.

In Figure 6.2, the variation of the calculated conversion is compared for different values of the cross flow coefficient using model (III). Higher values of k increase the mass transfer rate,

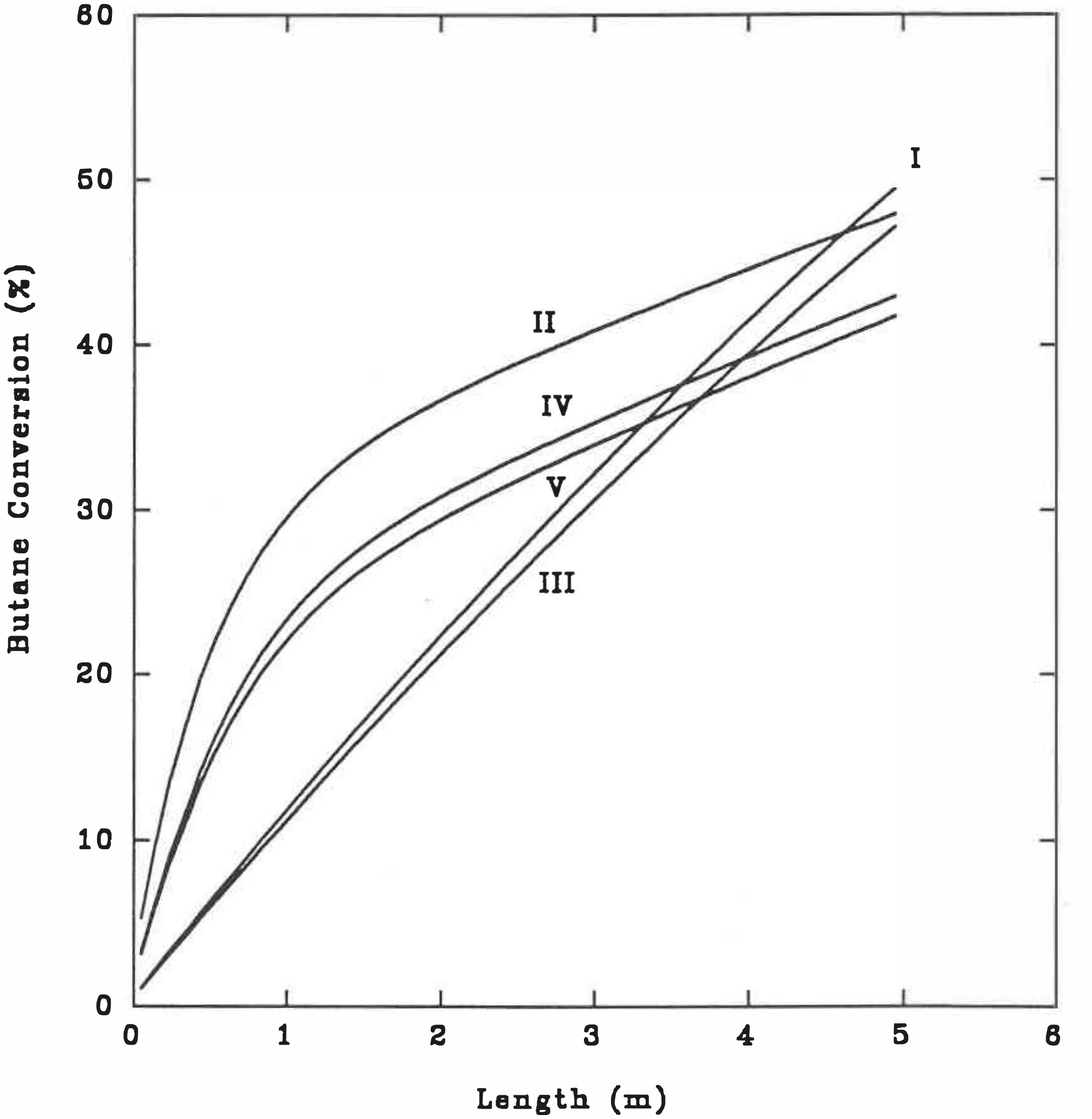

Figure 6.1: Butane conversion predictions of five hydrodynamics models

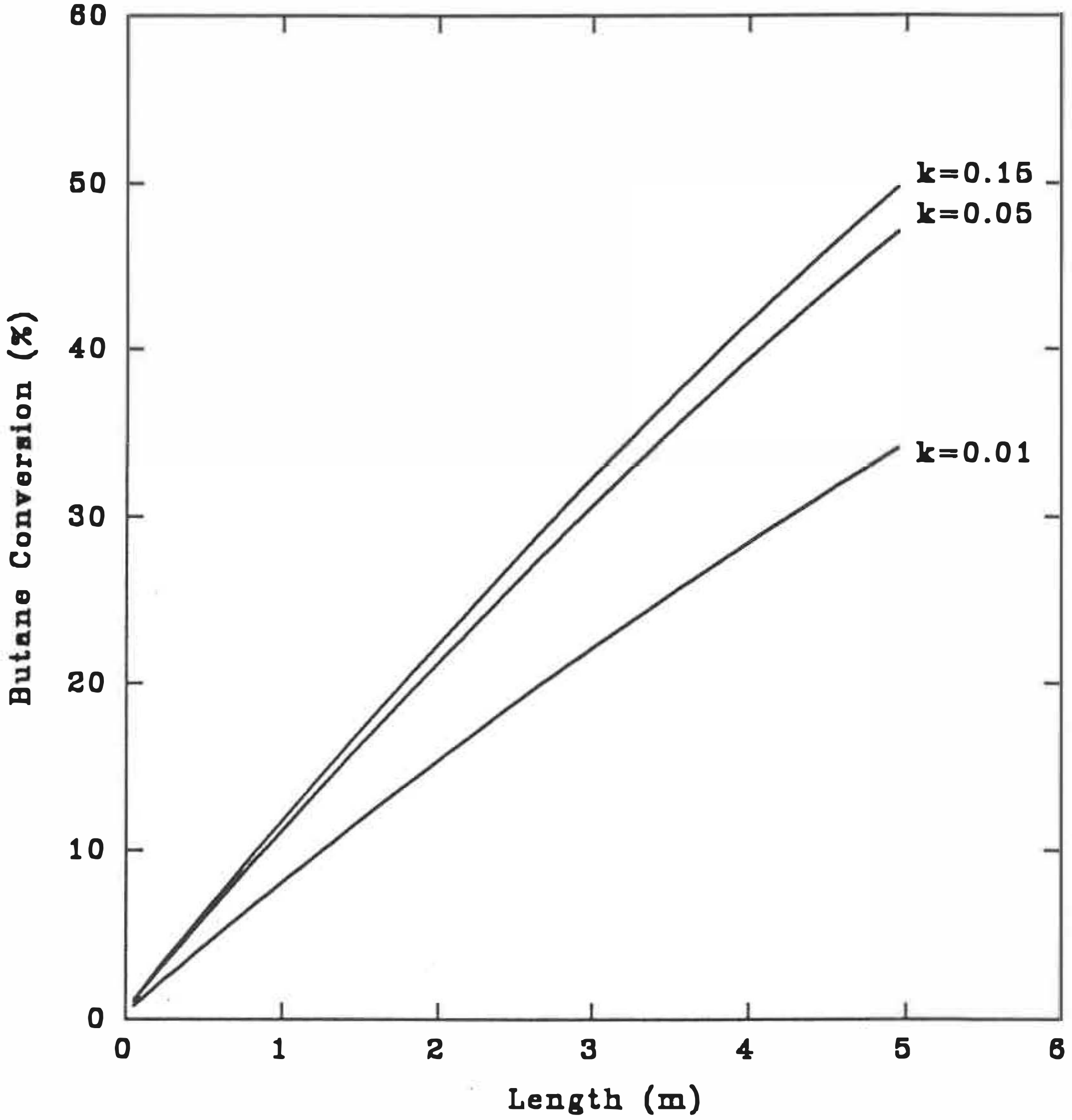

Figure 6.2: Core Annular Model Predictions, variation with cross-flow coefficient, k

hence conversion. The gas RTD studies indicate that the mass transfer rate decreases longitudinally. Typical values range from 0.09 m/s at the base of the riser to 0.03 m/s in the lean phase. The total conversion is sensitive to the assumed values and further work is necessary to establish the effect of different particles on the transfer rate as well as the diameter of the riser. Brereton (1987) presents results on the variation of the suspension density for smooth exits. The total solids hold-up was shown to be much less than for abrupt exits. Presumably, the smooth exits would result in lower mass transfer rates between the two zones. Total conversion would also be lower for the smooth exit because the solids inventory is less compared to the abrupt exit.

The effect of φ on total butane conversion is illustrated in Figure 6.3. Higher values of φ correspond to higher gas velocities in the core which implies a shorter gas residence time. The assumed value of φ is not as critical to conversion as is the cross flow coefficient.

A brief study was undertaken to determine the effect of diameter on conversion. The experimental results given by Brereton (1987) were used. The experimental system consisted of a 152 mm diameter riser 9.3 m high. At a gas velocity of 7.1 m/s and a solids circulation rate of 60 kg/m^2s the average riser void fraction is 0.94. Assuming $k=0.08$ m/s and $\varphi=0.825$ the conversion of butane was 100%.

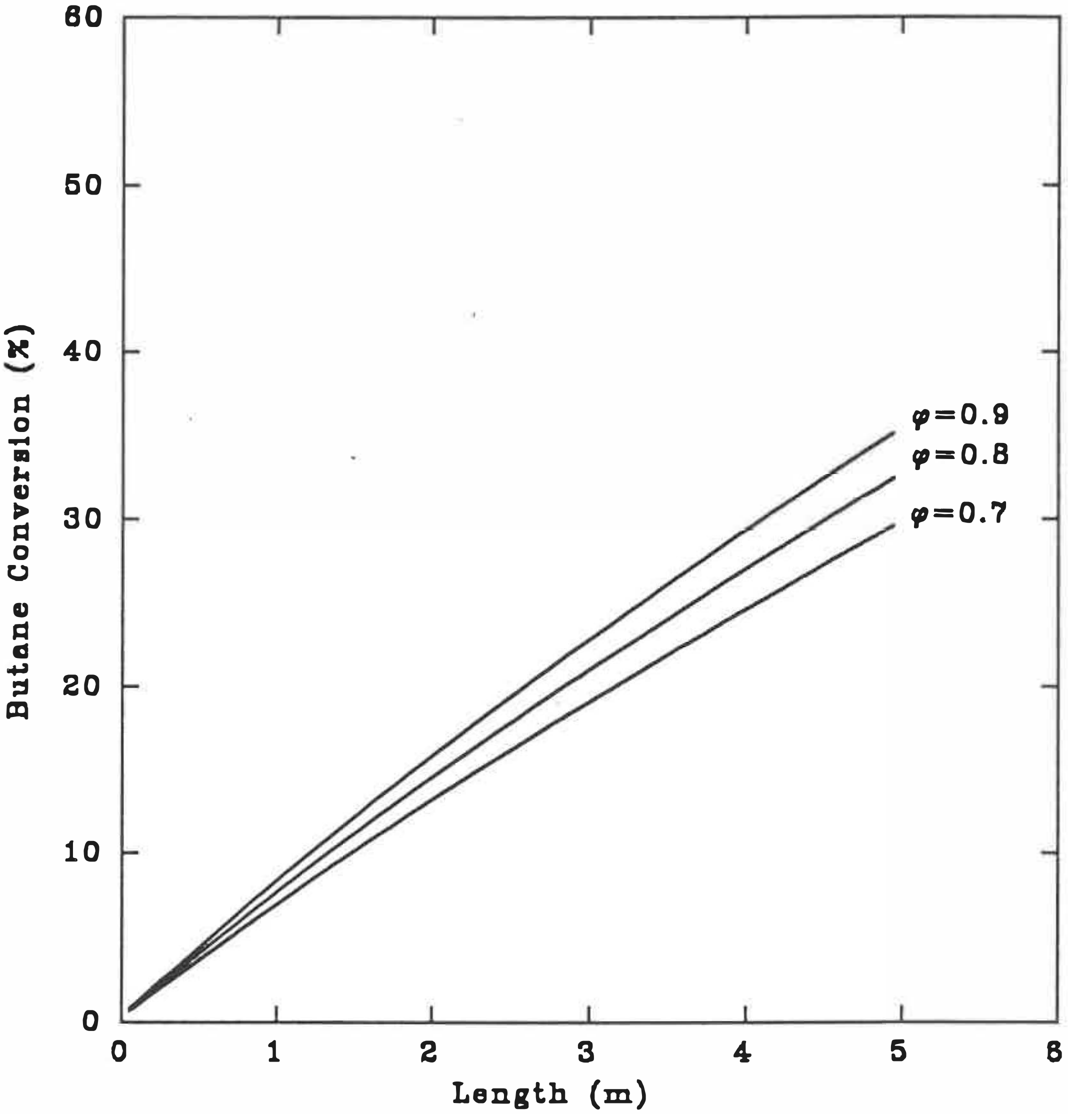

Figure 6.3: Core Annular Model Predictions, Variation with φ

Reducing the column height to 5 m and decreasing k to 0.03 m/s still resulted in 100% conversion. Clearly, the most important parameter is the total solids hold-up. Higher solids concentrations result in higher conversions. Comparisons between different diameter units should be made on a constant void fraction basis. Be that as it may, if the void fraction is less for larger diameter columns presumably the total conversion will be greater.

The selective oxidation of butane to maleic anhydride in a CFB riser was studied numerically to examine the effect of the hydrodynamic parameters determined from radioactive tracer studies. Predicted conversions are shown to be sensitive to both the cross flow coefficient between the annular zone and core as well as to φ. The kinetic model used was developed based on fixed bed studies and are not directly applicable to CFB risers. The lattice oxygen plays an important role in the synthesis of maleic anhydride. High butane inlet concentrations are permissible since much of the oxygen is carried by the catalyst. Hence future simulations should consider the redox mechanism of the surface oxygen to model and eventually optimize the riser.

7. CONCLUSIONS AND RECOMMENDATIONS

In this study of circulating fluidized bed systems, a number of important issues concerning the nature of gas solid transport are addressed. Dilute vertical phase transport, horizontal pneumatic conveying, packed bed flow and slug flow are all common to CFB systems. A correlation is developed relating the solids circulation rate to the measured pressure drop and gas velocity in the horizontal section between the riser and cyclone. The flow pattern, designated as a "degenerate suspension", is characterized by elongated clusters that deflect of the top and sides of the pipe wall and slide along the bottom.

In the standpipe, packed bed flow predominates. The gas is generally dragged down the standpipe with the solids. However, at low gas velocities (>4 m/s) and high suspension densities in the entrance region of the riser, standpipe gas flows counter-current to the solids. The solids circulation rate is a unique function of the aeration air whereas the standpipe pressure drop depends on both the solids flux and the riser conditions. The Ergun equation correlates the pressure drop data and flow rates well. The void fraction is approximately equal to ϵ_{mf} and the bulk velocity is greater than the velocity seen along the tube wall. Errors of up to 100% result assuming that

$$G_s = \rho_s(1-\epsilon_{mf})V_w \qquad (7.1)$$

The L-valve pressure drop varies little at high circulation rates. No attempt was made to model this region. However, it is believed that the pressure drop depends on the fraction of gas moving through emulsion phase compared to the slug phase. Significant gas override occurs at all gas velocities.

The solids and gas behaviour in the riser is characterized by a two zone model: a lean core surrounded by a dense annulus. The magnitude of the cross-flow coefficients, k_g, decreases vertically as does the ratio of the core radius to riser radius. Typically k_g varies from 0.03 m/s in the lean zone of the riser to 0.09 m/s in the dense region at the base. An average value of 0.05 m/s correlates the combined effect of the dense and lean regions well. Results from the numerical simulation of butane to maleic anhydride indicate that the total conversion is sensitive to the assumed cross-flow coefficient.

The solids behaviour is more complicated than the gas phase. The slip velocity in the core of the lean region is equal to the single particle terminal velocity. In the dense zone, the slip velocity is greater than the terminal velocity of the particles. Average residence times in the annulus of the dense region are equal to the residence time in the lean zone and equal one second at a circulation rate of 150 kg/m^{2}s and a gas velocity of 8 m/s. The residence times in the annulus increase with a decrease in gas velocity at the same circulation rate. Cross-flow coefficients of the solids are less than for the gas. Equal values of the cross-flow coefficient simulate the RTD in the lean zone. In the dense zone $k_{s,c\rightarrow} > k_{s,a\rightarrow}$.

A computational study is detailed concerning the selective oxidation of butane to maleic anhydride. Predictions of a number of different hydrodynamic models are compared. The core-annular model with an exponentially decaying cross-flow coefficient and core radius predicts the lowest total butane conversion. Mass transfer rates between the core and annulus in the lean regoion are low as is the butane conversion.

A similar experimental design is required to quantify the effect of particle characteristics on the hydrodynamics of the riser and standpipe. In particular, Geldart Group C powders such as FCC should be examined. The experimental study should start by evaluating the solids circulation rate. Both radioactive gas and solids tracer are required to determine the standpipe velocities and to evaluate the amount of axial dispersion. Subsequently, radioactive tracers are required to study the hydrodynamics of the riser in both the lean region and dense region. To initiate such a program, however, requires a secondary cyclone and perhaps a bag filter. The knock-out drum near the exhaust could used as a housing for the filter.

In addition to varying the particle characteristics, a detailed study is required to examine the entrance and exit effects. Particle RTD with a round exit geometry could elucidate the backmixing introduced by an abrupt right angle. Different standpipe geometries and their effect on the acceleration zone of the riser should also be examined.

The effect of height may be studied without modification of the system because a manifold was installed in the exhaust line. However, a short standpipe will not develop the head necessary to study high circulation rates. Therefore, it might be advantageous to add another two meters to the system. This might be accomplished by adding a metre at the base of the riser and another metre at the top.

The original intention of the unit was to study the partial oxidation of butane to produce maleic anhydride. Due to the unavailability of the catalyst a simpler reaction could be considered, such as the degradation of maleic anhydride by silica. This experiment would help fine tune the analytical equipment and might provide greater insight as to the gas phase transfer between the core and annular zones. Moreover, this reaction would be much less hazardous than butane oxidation.

REFERENCES

Adams, C. K., "Gas Mixing in Fast Fluidized Beds", in Circulating Fluidized Bed Technology II, P. Basu and J. F. Large, Eds., 43-46 Pergamon Press, Toronto (1988).

Ambler, J.P.A., "Residence Time Distribution of Binary Solids Mixtures in a Circulating Fluidized Bed", M.A.Sc. Thesis, University of Waterloo, Canada (1988).

Ambler, P.A., Milne, B.J., Berruti, F. and Scott, D.S., "Residence Time Distribution of Solids in a Circulating Fluidized Bed: Experimental and Modelling Studies", Chem. Eng. Sci., 45 (8), 2179-2186 (1990).

Ananthakrishnan, V., Gill, N. and Barduhn, A. J., "Laminar Dispersion in Capillaries: Part I. Mathematical Analysis", A.I.Ch.E. Journal, **11**, (6), 1063-1072 (1965)

Arena, U., Cammarota, A., and Pistone, L., "High Velocity Fluidization Behaviour of Solids in a Laboratory Scale Circulating Bed", in Circulating Fluidized Bed Technology, P. Basu, Ed., 119-126 Pergamon Press, Toronto (1986).

Arena, U., Cammarota, A., Marzocchella, A., and Massimilla, L., "Solids Flow Structures in a Two-Dimensional Riser of a Circulating Fluidized Bed", J. Chem. Eng. Japan, **22**, (3), 236-241 (1989).

Aris, R., "Notes on the Diffusion-Type Model for Longitudinal Mixing in Flow", Chem. Eng. Sci., **9**, 266-267 (1959).

Aziz, A. and Settari, K., Petroleum Reservoir Simulation, Applied Science Published (1983).

Bader, R., Findlay, J., and Knowlton, T. M., "Gas/Solids Flow Patterns in a 30.5 cm Diameter Circulating Fluidized Bed", in Circulating Fluidized Bed Technology, P. Basu, Ed., 123-137, Pergamon Press, Toronto (1988).

Bate, H., Rowlands, S., and Sirs, J. A., "Influence of Diffusion on Dispersion of Indicators in Blood Flow", J. Appl. Physiol, **34** (6), 866-871 (1973).

Berruti, F. and Kalogerakis, N., "Modelling the Internal Flow Structure of Circulating Fluidized Beds", Can. J. Chem. Eng., **67**, 1010-1014 (1989).

Bielanski, A. and Haber, J., "Oxygen in Catalysis on Transition Metal Oxides", Catal. Rev. Sci. Eng., **19** (1), 1-41 (1979).

Bischoff, K. B., "Notes on the Diffusion-Type Model for Longitudinal Mixing in Flow", Chem. Eng. Sci., **12**, 69-70 (1960).

Bischoff, K. B. and Levenspiel, O., "Fluid Dispersion-Generalization and Comparison of Mathematical Models-I Generalization of Models", Chem. Eng. Sci., **17**, 245-255 (1962).

Bolton, L. W. and Davidson, J. F., "Recirculation of Particles in Fast Fluidized Risers", in Circulating Fluidized Bed Technology II, P. Basu and J. F. Large, Eds., 139-146, Pergamon Press, Toronto (1988).

Brereton C. M. H., Grace, J. R., and Yu, J., "Axial Gas Mixing in a Circulating Fluidized Bed", in Circulating Fluidized Bed Technology II, P. Basu and J. F. Large, Eds., 209-212, Pergamon Press, Toronto (1988).

Brereton, C. M. H., "Fluid Mechanics of High Velocity Fluidized Beds", Ph.D. Dissertation, U.B.C., Vancouver, B.C., Canada (1987).

Burkell J. J., Grace, J. R., Zhao, J. and Lim, C. J., "Measurement of Solids Circulation Rate in Circulating Fluidized Beds", in Circulating Fluidized Bed Technology II, P. Basu and J.F. Large, Eds., Pergamon Press, Toronto, 501-509 (1988).

Cankurt, N. T. and Yerushalmi, J., "Gas Mixing in High Velocity Fluidized Beds", in Fluidization, J.F. Davidson and D.L. Kearins, Eds., 387-392, Cambridge Univ. Press, Cambridge (1978).

Capes, C. E. and Nakamura, K., "Vertical Pneumatic Conveying: An Experimental Study with Particles in the Intermediate and Turbulent Flow Regimes", Can. J. Chem. Eng., **51**, 31-38 (1973).

Centi, G., Galassi, G., Maneti, I., Riva, A., and Trifiro, F., in Preparation of Catalysts III, G. Ponclet, P. Grange and P. A. Jacobs, Eds., Elsevier, Amsterdam (1983).

Centi, G., Fornasari, G., and Trifiro, F., "n-Butane Oxidation to Maleic Anhydride on Vanadium-Phosphorous Oxides: Kinetic Analysis with a Tubular Flow Stacked-Pellet Reactor", Ind. Eng. Chem. Prod. Res. Dev., **24**, 32-37 (1985).

Chowdhury, J. and Ushio, S., "Big Changes are in Store for Maleic Anhydride Makers", Chem. Eng., Aug 17, 29-33 (1987).

Contrator, R. M., "Butane Oxidation to Maleic Anhydride in a Recirculating Solids Riser Reactor", in Circulating Fluidized Bed Technology II, P. Basu and J. F. Large, Eds., 467-474, Pergamon Press, Toronto (1988).

Contractor, R. M. and Sleight, A. W., "Maleic Anhydride from C-4 Feedstocks using Fluidized Bed Reactors", Catalysis Today, **1**, 587-607 (1987).

Danckwerts, P. V. "Continuous Flow Systems: Distribution of Residence Times", Chem. Eng. Sci., 2 (1), 1-13 (1953).

Deckwer, W.-D. and Mahlmann, E. A., "Boundary Conditions of Liquid Phase Reactors with Axial Dispersion", Chem. Engng. J., **11**, 19-25 (1976a).

Deckwer, W.-D. and Mahlmann, E. A., Chem. Eng. Sci., **31**, 1221 (1976b).

Dogin, M. E. and Lebedev, V. P., Ind. Chem. Eng. (USSR), 2 (1962) 64.

Dry, R. J., Christenn, I. M., and White, C. C., "Gas-Solids Contact Efficiency in a High-Velocity Fluidised Bed", Powder Technol., **53**, 243-250 (1987).

Dwivedi, P. N. and Upadhay, S. N., "Particle-Fluid Mass Transfer in Fixed and Fluidized Beds", Ind. Eng. Chem. Proc. Des. Dev., **16**, 157-165 (1977).

Escardino, A., Sola C., and Ruiz, F., "Oxidation Catalitica de Butano a Anhidrido Maleico", Anal. de Quim., **69**, 1157-1168 (1973).

Garbassi, F., Bart, J. C. J., Tassinari, R., Vlaic, G., and Lagarde, P., "Catalytic n-Butane Oxidation Activity and Physicochemical Characterization of Vanadium-Phosphorous Oxides with Variable P/V Ratios", J. of Catalysis, **98**, 317-325 (1986).

Geldart, D., "Estimation of Basic Particle Properties for use in Fluid-Particle Process Calculations", Powder Technol., 60, 1-13 (1990).

Geldart, D. and Rhodes, M. J., "From Minimum Fluidization to Pneumatic Transport - A Critical Review of the Hydrodynamics", in Circulating Fluidized Bed Technology, P. Basu, Ed., 21-31, Pergamon Press, Toronto (1986).

Glicksman, L.R., "Circulating Fluidized Bed Heat Transfer", in Circulating Fluidized Bed Technology II, P. Basu and J. F. Large, Eds., 13-29, Pergamon Press, Toronto (1988).

Govier, G. W. and Aziz, K., The Flow of Complex Mixtures in Pipes, Robert E. Krieger, New York (1972).

Grace, J. R., "Contacting Modes and Behaviour Classification of Gas-Solid and Other Two-Phase Suspensions", J. Can. Chem. Eng., **64**, 353-363 (1986).

Hartge, E.-U., Rensner, D., and Wether, J., "Solids Concentration and Velocity Patterns in Circulating Fluidized Beds", in Circulating Fluidized Bed Technology II, P. Basu and J. F. Large, Eds., 165-180, Pergamon Press, Toronto (1988).

Hartge, E.-U., Li, Y., and Werther, J., "Analysis of the Local Structure of the Two-Phase Flow in a Fast Fluidized Bed", in Circulating Fluidized Bed Technology, P. Basu, Ed., 153-160, Pergamon Press, Toronto (1986).

Helmrich, H., Schugerl, K., and Janssen, K., "Decomposition of $NaHCO_3$ in Laboratory and Bench Scale Circulating Fluidized Bed Reactors", in Circulating Fluidized Bed Technology, P. Basu, Ed., 161-166, Pergamon Press, Toronto (1986).

Hodnett, B. K. and Delmon, B., "Influence of Reductive Pretreatments on the Activity and Selectivity of Vanadium-Phosphorous Oxide Catalysts for n-butane Partial Oxidation", Ind. Eng. Chem. Fundam., 23, 465-470 (1984).

Horio, M., Morishita, K., Tachibana, O., and Murata, N., "Solid Distribution and Movement in Circulating Fluidized Beds", in Circulating Fluidized Bed Technology II, P. Basu and J. F. Large, Eds., 147-154, Pergamon Press, Toronto (1988).

Hsu, J. T. and Dranoff, J. S., "On Initial Problems for Reactor Dispersion Model", Chem. Eng. Sci., **41** (7), 1930-1934 (1986).

Ishii, H., Nakajima, T., and Horio, M., "The Clustering Annular Flow Model of Circulating Fluidized Beds, J. Chem. Eng. Japan, **22** (5), 484-490 (1989).

Jaffres, J. L., Chavarie, C., Patterson, I., Perrier, M., Casalegno, L., and Lagerie, C., "Conversion and Selectivity Modeling of the Oxidation of Benzene to Maleic Anhydride in a Fluidized Bed Reactor", Fourth International Conference on Fluidization, Japan (1983).

Jones, J. H., Braun, W. G., Daubert, T. E. and Allendorf, H. D., "Estimation of Pressure Drop for Vertical Pneumatic Transport of Solids", AIChE J., **13** (3), 608-611 (1967).

Kato, K., Shibasaki, H., Tamura, K., Arita, S., Wang, C., and Takarada, T., "Particle Holdup in a Fast Fluidized Bed", J. Chem. Eng. Japan, **22** (2), 130-136 (1989).

Kehoe, P. W. K. and Davidson, J. F., Inst. Chem. Eng. Symp. Ser., **33**, 97 (1971).

Kennedy, G., personal communication (1989).

Klinzing, G. E., Gas-Solid Transport, McGraw-Hill, New York (1981).

Kmiec, A. and K. Leschonski, K., "Acceleration of the Solid Phase During Pneumatic Conveying in Vertical Pipes", Chem. Eng. J., **36**, 50-70 (1987).

Knowlton, T. M. and Hirsan, I., "L-Valves Characterized for Solids Flow", Hydrocarbon Processing, March, 149-156 (1978).

Knowlton, T. M., Hirsan, I. and Leung, L. S., "The Effect of Aeration Tap Location on The Performance of a J-Valve", Fluidization, Cambridge University Press, 128-133 (1978).

Knowlton, T. M., "Nonmechanical Solids Feed and Recycle Devices for Circulating Fluidized Beds", in Circulating Fluidized Bed Technology II, P. Basu and J. F. Large, Eds., 31-41, Pergamon Press, Toronto (1988).

Kojima, T., Ishihara, K. I., Guilin, Y., and Furusawa, T., "Measurement of Solids Behaviour in a Fast Fluidized Bed", J. Chem. Eng. Japan, **22**, (4), 341-346 (1989).

Kolev, S. D. and Pungor, E., "Numerical Solution of Hydraulic Models

Based on the Axially-Dispersed Plug Flow Model by Laplace Transforms", Anal. Chim. Acta, **194**, 61-75 (1987).

Konno, H. and Saito, S., "Pneumatic Conveying of Solids Through Straight Pipes", J. Chem. Eng. Japan, **2**, 211-217 (1969).

Kwauk, M., Ningde, W., Youchu, L., Bingyn, C., and Zhiyuan, S., "Fast Fluidization at ICM", in Circulating Fluidized Bed Technology, P. Basu, Ed., 33-62, Pergamon Press, Toronto (1986).

Lanneau, K. P., "Gas-Solids Contacting in Fluidized Beds", Trans. Inst. Chem Eng., **38**, 125 (1960).

Lapidus, L. and Amundson, N. R., "Mathematics of Adsorption in Beds. VI. The Effects of Longitudinal Diffusion in Ion Exchange and Chromatographic Columns", J. Phys. Chem., **56**, 984-987 (1952).

Lee, G. S. and Kim, S. D., "Pressure Fluctuations in Turbulent Fluidized Beds", J. Chem. Eng. Japan, **21** (5), 515-521 (1988).

Lee, S. L., and Srinivansan, J., "Measurement of Local Size and Velocity Probability Density Distributions in Two-Phase Suspension Flows by Laser-Doppler Technique", Int. J. Multiphase Flow, **4**, 141-155 (1978).

Lee, S. L., and Srinivansan, J., "An LDA Technique for In-Situ Simultaneous Velocity and Size Measurement of Large Spherical Particles in a Two-Phase Suspension Flow", Int. J. Multiphase Flow, **8**, 47-57 (1982).

Leung, L. S. and Jones, P. J., "Flow of Gas-Solid Mixtures in Standpipes, a Review", Powder Technol., **20**, 145-160 (1978).

Levenspiel, O., Chemical Reactor Engineering, John Wiley and Sons Inc., New York (1972).

Levenspiel, O., Lai, B. W., and Chatlynne, C. Y., "Tracer Curves and Residence Time Distribution", Chem. Eng. Sci., 25, 1611-1613 (1970).

Levenspiel, O. and Smith, W. K., "Notes on the Diffusion-Type Model for the Longitudinal Mixing of Fluids in Flow", Chem. Eng. Sci., **6**, 227-233 (1957).

Levenspiel, O. and Sater, V. E., "Two Phase Flow in Packed Beds", Ind. Engng. Chem. Funds., 5, 86-92 (1966).

Levenspiel, O. and Turner, J. C. R., "The Interpretation of Residence Time Experiments", Chem. Eng. Sci., **25**, 1605-1609 (1970).

Matsumoto, S., Harakawa, H., Suzuki, M., and Ohtani, S., "Solid

Particle Velocity in Vertical Gaseous Suspension Flows", Int. J. Multiphase Flow, **12** (3), 445-458 (1986).

McCabe, W.L. and Smith, J.C., Unit Opertaions of Chemical Engineering, McGraw-Hill Book Co., Montreal, 1976.

Michelson, M. L. and Ostergaard, K., "The Use of Residence Data for Estimation of Parameters in the Axial Dispersion Model", Chem. Eng. Sci., **25**, 583-592 (1970).

Monceaux, L., Azzi, M., Molodtsof, Y., and Large, J. F., "Overall and Local Characterisation of Flow Regimes in a CFB's, in Circulating Fluidized Bed Technology, P. Basu, Ed., 185-191, Pergamon Press, Toronto (1986).

Nakamura, K. and Capes, C. E., "Verical Pneumatic Conveying: A Theoretical Study of Unifom and Annular Particle Flow Models", Can. J. Chem. Eng., **51**, 39-46 (1973).

Ozkan, U. and Schrader, G. L., "$NiMoO_4$ Selective Oxidation Catalyst Containing Excess MoO_3 for the Conversion of C_4 Hydrocarbons to Maleic Anhydride: 1. Preparation and Characterization", J. of Catalysis, **95**, 120-136 (1985a).

Ozkan, U. and Schrader, G. L., "2. Selective Oxidation of 1-butene",

J. of Catalysis, **95**, 137-146 (1985b).

Ozkan, U. and Schrader, G. L., "3. Selective Oxidation of 1,3 Butadiene and Furan", J. of Catalysis, **95**, 147-154 (1985c).

Patankar, S. V., Numerical Heat Transfer and Fluid Flow, McGraw-Hill Book Company, Montreal (1980).

Patience, G. S., and Chaouki, J., "Vertical Voidage Profiles in CFB Rectors", Chem. Eng. Res. Des., **68**, Part A, 301 (1990).

Patience, G. S., Chaouki, J., and Grandjean, B.P.A., "Solids Flow Metering From Pressure Drop Measurement in Circulating Fluidized Beds", Powder Technol., **61** (1), 95-99 (1990).

Pepera, M. A., Callahan, J. L., Desmond, M. J., Milberger, E. C., Blum, P. R., and Brewer, N. J., "Fundamental Study of the Oxidation of Butane over Vanadyl Pyrophosphate", J. Am. Chem. Soc., **107**, 4883-4892 (1985).

Porter, P. E., Deal, C. H., and Stross, F. H., "The Determination of Partition Coefficients from Gas-Liquid Partition Chromatography", J. Am. Chem. Soc., **78**, 2999-3006 (1956).

Press, W. H., Flannery, B. P., Teukolsky, S. A., and Vetterling, W.

T., Numerical Recipes, Cambridge University Press (1986)

Reh, L., "The Circulating Fluid Bed Reactor - a Key to Efficient Gas/Solid Processing", in Circulating Fluidized Bed Technology, P. Basu, Ed., 105-118, Pergamon Press, Toronto (1986).

Rhodes, M. J., Laussmann, P., Villain, F., and Geldart, G., "Measurement of Radial and Axial Solids Flux Variations in the Riser of a Circulating Fluidized Bed", in Circulating Fluidized Bed Technology II, P. Basu and J. F. Large, Eds., 20-25, Pergamon Press, Toronto (1988).

Rhodes, M. J. and Geldart, D., "The Upward Flow of Gas/Solid Suspensions, Part I: A Model for the Circulating Fluidized Bed Incorporating Dual Level Gas Entry Into the Riser", Chem. Eng. Res. Des., **67**, 20-29 (1989).

Rhodes, M. J., and Geldart, D., "The Hydrodynamics of Recirculating Fluidized Beds", in Circulating Fluidized Bed Technology , P. Basu, Ed., 193-200, Pergamon Press, Toronto (1986).

Rhodes, M. J. "Modelling the Flow Structure of Upward-Flowing Gas-Solids Suspensions", Powder Technol., **60**, 27-38 (1990).

Rose, H. E. and Duckworth, R. A., "Transport of Solid Particles in

Liquids and Gases", The Engineer, **227** (5903) 392-396; **227** (5904) 430-433; **227** (5905) 478-483 (1969).

Rowe, P. N., "Experimental Properties of Bubbles", Fluidization, J. F. Davidson and D. Harrison, Eds., 121-191, Academic Press Inc., London (1971).

Ruzicka, J. and Hansen, E., "The First Decade of Flow Injection Analysis: From Serial Assay to Diagnostic Tool", Anal. Chem. Acta, **179**, 1-58 (1986).

Sater, V. E. and Levenspiel, O., "Two-Phase Flow in Packed Beds: Evaluation of Axial Dispersion and Holdup by Moment Analysis", I&EC Fund., **5** (1), 86-92 (1966).

Schneider, P., Emig, G., and Hofmann, H., "Systematic Approach to Development of Catalysts for Oxidation Reactions", Ger. Chem. Eng., **9**, 337-345 (1986).

Schneider, P., "Katalysatorentwicklung and Kinetishe Untersuchung am Beispiel der Maleinsaurean hydrid -Herstellung ans n-butan", Ph.D. Thesis, Uni. Erlangen-Nurnberg, W. Germany (1985).

Schnitzlein, M. G. and Weinstein, H., "Design Parameters Determining Solid Hold-Up in Fast Fluidized Bed Systems", in Circulating Fluidized Bed Tchnology II, P. Basu and J. F. Large, Eds., 205-212, Pergamon Press, Toronto (1988).

Schnitzlein, M. G., and Weinstein, H., "Flow Characterization in High Velocity Fluidized Beds Using Pressure Fluctuations", Chem. Eng. Sci., **47** (10), 2605-2614 (1988).

Smith, J. M., Chemical Engineering Kinetics, McGraw-Hill Book Company, Toronto (1981).

Soo, S. L., Handbook of Multiphase Systems, G. Hestroni, Ed., 7-3, McGraw-Hill, New York (1982).

Squires, A. M., "The Story of Fluid Catalytic Cracking: The First Circulating Fluid Bed", in Circulating Fluidized Bed Technology, P. Basu, Ed., 1-19, Pergamon Press, New York (1986).

Stemerding, S., "The Pneumatic Transport of Cracking Catalyst in Vertical Risers", Chem. Eng. Sci., **17**, 599-608 (1962).

Sternberg, J. C., "Extracolumn Contributions to Chromatographic Band Broadening", Advanc. Chromatogr., 2, 205-270 (1966).

Taylor, Sir Geoffrey, "Dispersion of Soluble Matter in Solvent Flowing Slowly Through a Tube", Proc. Roy. Soc. London, **A219**, 186-203

(1953).

Taylor, Sir Geoffrey, "The Dispersion of Matter in Turbulent Flow Through a Pipe", Proc. Roy. Soc. London, **A223**, 446-468 (1954a).

Taylor, Sir Geoffrey, "Conditions under which Dispersion of a Solute in a Stream of Solvent Can Be Used to Measure Molecular Diffusion", Proc. Roy. Soc. London, **A225**, 473-477 (1954b).

Trimm, D. L., Design of Industrial Catalysts, Elsevier Scientific Publishing Company, New York (1980).

Van der Laan, E. T., "Notes on the Diffusion-Type Model for the Longitudinal Mixing in Flow", Chem. Eng. Sci., **7**, 187-191 (1958).

Vanderslice, J. T., Stewart, K. K., Rosenfeld, A. G., and Higgs, D. J., "Laminar Dispersion in Flow-Injection Analysis", Talanta, **28**, 11-18 (1981).

Websters Third New International Dictionary, William Benton, Publisher, Encyclopaedia Britannica Inc., London (1966).

Wehner, J. F. and Wilhelm, R. H., "Boundary Conditions of Flow Reactor", Chem. Eng. Sci., **6**, 89-93 (1956).

Weinstein, H., Shao, M., and Schnitzlein, M., "Radial Variation in Solid Density in High Velocity Fluidization", in Circulating Fluidized Bed Technology, P. Basu, Ed., 201-206, Pergamon Press, Toronto (1986).

Wen, C.-Y. and Simmons, H. P., "Flow Characteristics in Horizontal Fluidized Solids Transport", AIChE J., **5** (2), 263-267 (1959).

Wen, C.-Y. and Chen, L. H., "Fluidized Bed Freeboard Phenomena: Entrainment and Elutriation", AIChE J., **28** (1), 117-128 (1982).

Westerterp, K. R., Van Swaaij, W. P. M., and Beenackers, A. A. C. M., Chemical Reactor Design and Operation, John Wiley & Sons, Toronto (1984).

Wirth, K. E., "Axial Pressure Profile in Circulating Fluidized Beds", Chem. Eng. Technol., **11**, 11-17 (1988).

Wohlfahrt, K. and Hofmann, H., Chem. Ing. Tech., **52**, 52 (1980).

Yang, G., Huang, Z., and Zhao, L., "Radial Gas Dispersion in a Fast Fluidized Bed", in Fluidization, D. Kunii and R. Toei, Eds., 145-152, Engineering Foundation, New York (1983).

Yerushalmi, J. and Avidan, A., "High Velocity Fluidization", in

Fluidization, J.F. Davidson, R. Clift, and D. Harrison, Eds., 225-291, Academic Press, Montreal (1985).

Yerushalmi, J., Cankurt, M., Geldart, D., and Liss, B., "Flow Regimes in Vertical Gas-Solid Contact Systems", AIChE Symp. Ser., **74** (76), 1-13 (1978).

Yoon, S. M. and Kunii, D., "Gas Flow and Pressure Drop Through Moving Beds", Ind. Eng. Chem. Process Des. Develop., **9** (4), 559-565 (1970).

Youchou, L. and Kwauk, M., "The Dynamics of Fast Fluidization", in Fluidization, J. R. Grace and J. Matsen, Eds., Plenum Press, New York, (1980).

Zenz, F. A., "Two-Phase Fluid-Solid Flow", Ind. Eng. Chem., **41**, 2801-2806 (1949).

Zenz, F. A., "Visualizing Gas-Solid Dynamics in Catalytic Processes", Pet. Refiner, **32**, 123-128 (1953).

Zhang, J.-Y., Rudolph, V., and Leung, L. S., "Non-Fluidized Flow of Gas-Solids in Standpipes Under Negative Pressure Gradient", Fluidization VI, 153-160.

APPENDIX A

Computer listing for the simulation of the selective oxidation of butane to maleic anhydride

```
/SYS REG=1024
/FILE FT03F001 NAME(H300:MAN.F21) NEW(REPL)
/FILE FT04F001 NAME(H300:MAN.F22) NEW(REPL)
/FILE FT08F001 NAME(H300:MAN.F23) NEW(REPL)
/PARM NOXUFLOW
/LOAD VSFORT
      IMPLICIT REAL*8 (A-H,O-Z)
      DIMENSION RESO(10,200),XO(2000),DC(10),DUMMY(10)
      DIMENSION X(2000)
      COMMON/BK1/ A(20000)
      COMMON/BK2/ VOL,VOL1(200),AX,AX1(200),DIA,DIA1(200),PI,DZ
      COMMON/BK3/ BK(200),VOID1(200),VOID2(200),PHI(200)
      COMMON/BK4/ TEMP,PT,RC,UZ(200),DISP,RHOP,DT,INZ,IP,ITN
      COMMON/BK5/ C(10,200),CO(10,200),CE(10)
      COMMON/BK6/ AK1,AK2,AK3,CK1,CK2,A1,A2,A3,A4
      COMMON/RHS/ D(2000)
      COMMON/EQUAT/ N,M
C
C          PHYSICAL CONSTANTS
C
      IP=10
      INZ=20
      DIST=3.89
      DIA=0.0828
      VG=1.0
      PT=1.0
      TEMP=573.0
      Q=0.021538
      GS=100.0
      RHOP=2630000.
      BKO=0.0001
      DISP=0.0
      TIME=100.0
      ITN=1
      DT=TIME/DFLOAT(ITN)
C
C          UNIVERSAL CONSTANTS
C
      G=9.80665
      RC=0.082056
      AA=1.0
      PI=4.0*DTAN(AA)
C
C          KINETICS
C
      AK1=0.000000336
      AK2=0.0000002
      AK3=0.000000044
      CK1=2616.0
      A1=0.230
      A2=0.230
      A3=0.635
      A4=1.15
C
C          INLET CONDITIONS
C
      CE(1)=0.006192
      CE(2)=0.001
```

```
      CE(3)=0.081764
      DO 30 I=4,10
      CE(I)=0.001
   30 CONTINUE
      CE(6)=CE(1)
      CE(7)=CE(2)
      CE(8)=CE(3)
C
C          MISCELLANEOUS CONSTANTS
C
      IMAX=10
      M=2*IP-1
      N=IP*INZ
      IGB=N*(2*M+1)-M*M-M
      EP=0.000000000001
      IFRST=0
C
      EPSO=0.68
      EPSE=1.
C
C           GRID BLOCK VOLUMES
C
      DZ=DIST/DFLOAT(INZ)
      VOL=PI*DIA*DIA*DZ/4.0
      AX=PI*DIA*DIA/4.0
      COEFF=0.9
      DO 31 I=1,INZ
      VOL1(I)=VOL*COEFF**2
      PHI(I)=VOL1(I)/VOL
      DIA1(I)=DIA*COEFF
      AX1(I)=AX*COEFF**2
      VOID1(I)=0.59
      VOID2(I)=0.99
      BK(I)=BKO
      UZ(I)=VG/(AX1(I)*VOID1(I))
   31 CONTINUE
C
      WRITE(3,200)
      WRITE(4,200)
      WRITE(8,200)
C
      DO 33 J=1,INZ
            DO 32 I=1,IP
            C(I,J)=CE(I)
            DC(I)=0.00001
   32       CONTINUE
      C(3,J)=0.08
   33 CONTINUE
C
C          TIME DO LOOP
C
      DO 34 IT=1,ITN
C
            DO 36 J=1,INZ
                  DO 35 I=1,IP
                  CO(I,J)=C(I,J)
   35             CONTINUE
   36       CONTINUE
       WRITE(6,*)ICOUNT,C(1,INZ)
C
```

```
C          SETTING-UP ITERATION SCHEME
C
      ICOUNT=0
C
  401       IJ=0
            DO 41 I=1,INZ
                  DO 40 J=1,IP
                  IJ=IJ+1
                  DUMMY(J)=RES(J,I,IT)
                  RESO(J,I)=DUMMY(J)
                  D(IJ)=-DUMMY(J)
   40             CONTINUE
   41       CONTINUE
C
            DO 50 II=1,IGB
            A(II)=0.0
   50       CONTINUE
C
C          EVALUATION OF THE PARTIAL DIFFERENTIALS
C
            IBB=0
            DO 45 I=1,INZ
                DO 44 IC1=1,IP
                IBB=IBB+IP-IC1
                IF(I.LE.2)IBB=IBB-IP+IC1
                    DO 43 JJ=1,3
                    J=JJ-1
                    IF((I.EQ.1).AND.(J.EQ.0))GO TO 43
                    IF((I.EQ.INZ).AND.(J.EQ.2))GO TO 402
                    IA=I+J-1
                        DO 42 IC2=1,IP
                        IBB=IBB+1
                        C(IC2,IA)=C(IC2,IA)+DC(IC2)
                        A(IBB)=(RES(IC1,I,IT)-RESO(IC1,I))/DC(IC2)
                        C(IC2,IA)=C(IC2,IA)-DC(IC2)
   42                   CONTINUE
   43               CONTINUE
  402           IBB=IBB+IC1-1
                IF(I.GE.(INZ-1))IBB=IBB-IC1+1
   44           CONTINUE
   45       CONTINUE
C
C          MATRIX CALCULATION & UPDATE OF PRIMARY VARIABLES
C
      CALL GBAND(X,EP,IERR,IFRST)
C
            DO 46 IC1=1,IP
            C(IC1,1)=C(IC1,1)+X(IC1)
            AA=C(IC1,1)
            IF((AA.LT.0.).OR.(AA.GT.1.0))C(IC1,1)=CE(IC1)
   46       CONTINUE
C
            IK=IP
            DO 48 IJ=2,INZ
                  DO 47 IC1=1,IP
                  IK=IK+1
                  C(IC1,IJ)=C(IC1,IJ)+X(IK)
                  AA=C(IC1,IJ)
                  IF((AA.LT.0.).OR.(AA.GT.1.0))C(IC1,IJ)=C(IC1,IJ-1)
   47             CONTINUE
```

```
      COMMON/BK4/ TEMP,PT,RC,UZ(200),DISP,RHOP,DT,INZ,IP,ITN
      COMMON/BK5/ C(10,200),CO(10,200),CE(10)
      COMMON/BK6/ AK1,AK2,AK3,CK1,CK2,A1,A2,A3,A4
      RHOG=PT/(RC*TEMP)
      IF(IV.GT.5)GO TO 600
      CA=C(1,I)
      CB=C(2,I)
      CC=C(3,I)
      DUMT=PHI(I)*VOID1(I)*(C(IV,I)-CO(IV,I))/DT
      IF(ITN.EQ.1)DUMT=0.0
      DUM6=4.0*BK(I)*(C(IV,I)-C(IV+5,I))/DIA1(I)
      DUM1A=UZ(I)*C(IV,I)
      IF(I.NE.1)GO TO 500
      DUM1B=UZ(1)*CE(IV)
      DUM2=2.*(DUM1A-DUM1B)/DZ
      GO TO 501
  500 DUM1B=UZ(I-1)*C(IV,I-1)
      DUM2=(DUM1A-DUM1B)/DZ
  501 IF(IV.EQ.2)GO TO 502
      IF(IV.EQ.3)GO TO 503
      IF(IV.EQ.4)GO TO 504
      IF(IV.EQ.5)GO TO 505
C
C         LEAN CORE REGION CALCULATIONS
C         -----------------------------
C
C         BUTANE RESIDUAL
C
      DUM3=AK1*CK1*CA*CC**A1/(1.+CK1*CA)
      DUM4=AK2*CC**A2
      DUM7=DUM3+DUM4
      RES=DUMT+DUM2+RHOP*(1.-VOID1(I))*PHI(I)*DUM7+DUM6
      RETURN
C
C         MALEIC ANHYDRIDE RESIDUAL
C
  502 DUM3=AK1*CK1*CA*CC**A1/(1.0+CK1*CA)
      DUM5=AK3*CB*CC**A3/CA**A4
      DUM7=DUM3-DUM5
      RES=DUMT+DUM2-RHOP*(1-VOID1(I))*PHI(I)*DUM7+DUM6
      RETURN
C
C         O2 RESIDUAL
C
  503 DUM3=AK1*CK1*CA*CC**A1/(1.0+CK1*CA)
      DUM4=AK2*CC**A2
      DUM5=AK3*CB*CC**A3/CA**A4
      DUM7=3.5*DUM3+6.5*DUM4+3.0*DUM5
      RES=DUMT+DUM2+RHOP*(1.-VOID1(I))*PHI(I)*DUM7+DUM6
      RETURN
C
C         H2O RESIDUAL
C
  504 DUM3=AK1*CK1*CA*CC**A1/(1.0+CK1*CA)
      DUM4=AK2*CC**A2
      DUM5=AK3*CB*CC**A3/CA**A4
      DUM7=4.0*DUM3+5.0*DUM4+DUM5
      RES=DUMT+DUM2-RHOP*(1.-VOID1(I))*PHI(I)*DUM7+DUM6
      RETURN
C
```

```
   48       CONTINUE
C
      ICOUNT=ICOUNT+1
      IF(ICOUNT.GT.IMAX)GO TO 1000
C
      IK=0
            DO 53 IJ=1,INZ
                  DO 49 IC1=1,IP
                  IK=IK+1
                  ZP=DABS(X(IK)/C(IC1,IJ))
                  IF(ZP.GE.0.0001)WRITE(6,*)IJ,IC1,X(IK)
                  IF(DABS(X(IK)/C(IC1,IJ)).GE.0.0001)GO TO 401
   49             CONTINUE
   53       CONTINUE
   34 CONTINUE
C
C          OUTPUT DATA
C
      WRITE(3,201)
      WRITE(4,204)
      WRITE(8,201)
      DO 52 I=1,INZ
      CONV=(1.0-C(1,I)/CE(1))*100.
      SEL=4.*C(2,I)/C(5,I)
      YIELD=C(2,I)/CE(1)
      WRITE(3,203)I,C(1,I),C(2,I),C(3,I)
      WRITE(4,203)I,CONV,SEL,YIELD
      WRITE(8,203)I,C(6,I),C(7,I),C(8,I)
   52 CONTINUE
C
C          END OF MAIN PROGRAM
C
      GO TO 1001
 1000 WRITE(3,202)IMAX
      WRITE(3,201)
      IJ=1
      DO 60 I=1,INZ
      CONV=(1.0-C(1,I)/CE(1))*100.
      SEL=4.*C(2,I)/C(5,I)
      YIELD=C(2,I)/CE(1)
      WRITE(3,203)I,C(1,I),C(2,I),C(3,I)
      WRITE(4,203)I,CONV,SEL,YIELD
      WRITE(8,203)I,C(6,I),C(7,I),C(8,I)
      WRITE(3,203)I,X(IJ),X(IJ+1),X(IJ+2)
      IJ=IJ+IP
   60 CONTINUE
  200 FORMAT(1H ,5X,'SIMULATION OF THE PARTIAL OXIADATION OF BUTANE')
  201 FORMAT(1H ,//,14X,'BUTANE',6X,'  MAN  ',7X,'   O2  ')
  202 FORMAT(5X,'CONVERGENCE NOT NET AT  ',I3,'TIME STEPS')
  203 FORMAT(1H ,2X,I3,4X,G12.5,2X,G12.5,2X,G12.5)
  204 FORMAT(1H ,//,14X,'CONVERSION',3X,'SELECIVITY',7X,'YIELD')
  001 STOP
      END

           SUBROUTINES AND SUBFUNCTIONS

      FUNCTION RES(IV,I,IT)
      IMPLICIT REAL*8 (A-H,O-Z)
      COMMON/BK2/ VOL,VOL1(200),AX,AX1(200),DIA,DIA1(200),PI,DZ
      COMMON/BK3/ BK(200),VOID1(200),VOID2(200),PHI(200)
```

```
C          CO2 RESIDUAL
C
  505 DUM4=AK2*CC**A2
      DUM5=AK3*CB*CC**A3/CA**A4
      DUM7=4.0*DUM4+4.0*DUM5
      RES=DUMT+DUM2-RHOP*(1.-VOID1(I))*PHI(I)*DUM7+DUM6
      RETURN
C
C          DENSE ANNULAR REGION CALCUALTIONS
C          ---------------------------------
C
  600 CA=C(6,I)
      CB=C(7,I)
      CC=C(8,I)
      DUM6=4.0*BK(I)*DIA1(I)*(C(IV-5,I)-C(IV,I))/(DIA**2-DIA1(I)**2)
      DUMT=(1.-PHI(I))*VOID2(I)*(C(IV,I)-CO(IV,I))/DT
      IF(ITN.EQ.1)DUMT=0.0
      IF(IV.EQ.7)GO TO 601
      IF(IV.EQ.8)GO TO 602
      IF(IV.EQ.9)GO TO 603
      IF(IV.EQ.10)GO TO 604
C
C          BUTANE RESIDUAL
C
      DUM3=AK1*CK1*CA*CC**A1/(1.0+CK1*CA)
      DUM4=AK2*CC**A2
      DUM7=DUM3+DUM5
      RES=DUMT+RHOP*(1.-VOID2(I))*(1.-PHI(I))*DUM7-DUM6
      RETURN
C
C          MALEIC ANHYDRIDE RESIDUAL
C
  601 DUM3=AK1*CK1*CA*CC**A1/(1.0+CK1*CA)
      DUM5=AK3*CB*CC**A3/CA**A4
      DUM7=DUM3-DUM5
      RES=DUMT-RHOP*(1.-VOID2(I))*(1.-PHI(I))*DUM7-DUM6
      RETURN
C
C          O2 RESIDUAL
C
  602 DUM3=AK1*CK1*CA*CC**A1/(1.0+CK1*CA)
      DUM4=AK2*CC**A2
      DUM5=AK3*CB*CC**A3/CA**A4
      DUM7=3.5*DUM3+6.5*DUM4+3.0*DUM5
      RES=DUMT+RHOP*(1-VOID2(I))*(1.-PHI(I))*DUM7-DUM6
      RETURN
C
C          H2O RESIDUAL
C
  603 DUM3=AK1*CK1*CA*CC**A1/(1.0+CK1*CA)
      DUM4=AK2*CC**A2
      DUM5=AK3*CB*CC**A3/CA**A4
      DUM7=4.0*DUM3+5.0*DUM4+DUM5
      RES=DUMT-RHOP*(1.-VOID2(I))*(1.-PHI(I))*DUM7-DUM6
      RETURN
C
C          CO2 RESIDUAL
C
  604 DUM4=AK2*CC**A2
      DUM5=AK3*CB*CC**A3/CA**A4
```

```
      DUM7=4.0*DUM4+4.0*DUM5
      RES=DUMT-RHOP*(1.-VOID2(I))*(1.-PHI(I))*DUM7-DUM6
      RETURN
      END
```

GBAND

```
      SUBROUTINE GBAND(X,EPS,IERR,IFRST)
      IMPLICIT REAL*8 (A-H,O-Z)
      DIMENSION X(2000)
      COMMON/BK1/ A(20000)
      COMMON/EQUAT/ N,M
      COMMON/RHS/ D(2000)
      IERR=0
      J=1
      DO 10 I=1,N
      IE=M
      IF(I+M-N)21,21,22
   22 IE=N-I
   21 IEAUX=M
      IF(I-M)23,23,24
   23 IEAUX=I
   24 IE1=IE+IEAUX
      MBIG=IE
      J1=J+IE1
      J2=J1
      IF(IFRST.GT.0)GO TO 27
      IF(DABS(A(J))-EPS)25,25,27
   25 IERR=IERR+1
   27 IF(MBIG)10,10,26
   26 DO 20 JO=1,MBIG
      S=A(J1)/A(J)
      IF(IFRST.GT.0)GO TO 35
      DO 30 K=1,MBIG
      J1K=J1+K
      JK=J+K
   30 A(J1K)=A(J1K)-A(JK)*S
   35 CONTINUE
      IAUX=JO+I
      D(IAUX)=D(IAUX)-D(I)*S
      IE=M
      IF(IAUX+M-N)31,31,32
   32 IE=N-IAUX
   31 IEAUX=M
      IF(IAUX-M)33,33,34
   33 IEAUX=IAUX
   34 IE1=IE+IEAUX
   20 J1=J1+IE1
   10 J=J2+1
      J=J-M-1
      NP1=N+1
      DO 40 IINV=1,N
      I=NP1-IINV
      IE=M
      IF(I+M-N)41,41,42
   42 IE=N-I
   41 MBIG=IE
      X(I)=D(I)
      IF(MBIG)44,44,43
   43       DO 50 K=1,MBIG
```

```
         IK=I+K
         JK=J+K
50       X(I)=X(I)-X(IK)*A(JK)
44 X(I)=X(I)/A(J)
   IE=M
   IF(I+M-NP1)51,51,52
52 IE=NP1-I
51 IEAUX=M
   IF(I-1-M)53,53,54
53 IEAUX=I-1
54 IE1=IE+IEAUX
   J=J-IE1-1
40 CONTINUE
   RETURN
   END
```

APPENDIX B

Parameter estimation analysis

A simple two zone core-annular model was used to characterize the hydrodynamics in the riser for both the gas and solids phase. The parameters of the model were fit by inspection. Each of the parameters was varied individually until a reasonable match to the experimental data was obtained. The experimental results presented in Figure 5.13 (U_g=8.2 m/s, G_s=140 kg/m^3) are used to demonstrate the procedure employed to obtain the parameters. The following parameters are considered:

(1) dispersion coefficient, D

(2) cross-flow coefficient, k

(3) break-up coefficient, k_1,

(4) φ, $(r_c/R)^2$

(5) initial tracer fraction entering the core

(6) number of grid blocks, N_z

(7) number of time steps, N_t

The optimized parameters were:

(1) D = 0.3 m^2/s

(2) k = 0.01 m/s

(3) k_1 = 1 m/s

(4) φ = 0.85

(5) initial tracer fraction in core - 0.2

(6) N_z = 400

(7) N_t = 1000

I Dispersion coefficient, D

In Figure A.1, predictions for three different values of the dispersion coefficient are compared with the experimental results. A high dispersion coefficient (D=0.6 m^2/s) decreases the height of the predicted peaks, whereas too low a value exaggerates the peak heights.

II Cross-flow coefficient, k

The trends reported when varying the dispersion coefficient are the similar to that observed for the cross-flow coefficient. As shown in Figure A.2, low values of k exaggerate the peak heights and high values tend to smear the two peaks into one.

III Break-up coefficient, k_1

The solids are injected perpendicular to the riser column. The annular velocity was assumed to be 0.8 m/s. Upon entering the column some of the solids are immediately accelerated in the core region. A larger fraction descends along the wall and gradually moves to the core region. The second smaller peak is interpreted as the mass of particles that descends a certain distance before eventually entering the core en masse. The coefficient, k_1, accounts for the high transfer rate between the core and annular region and is referred to

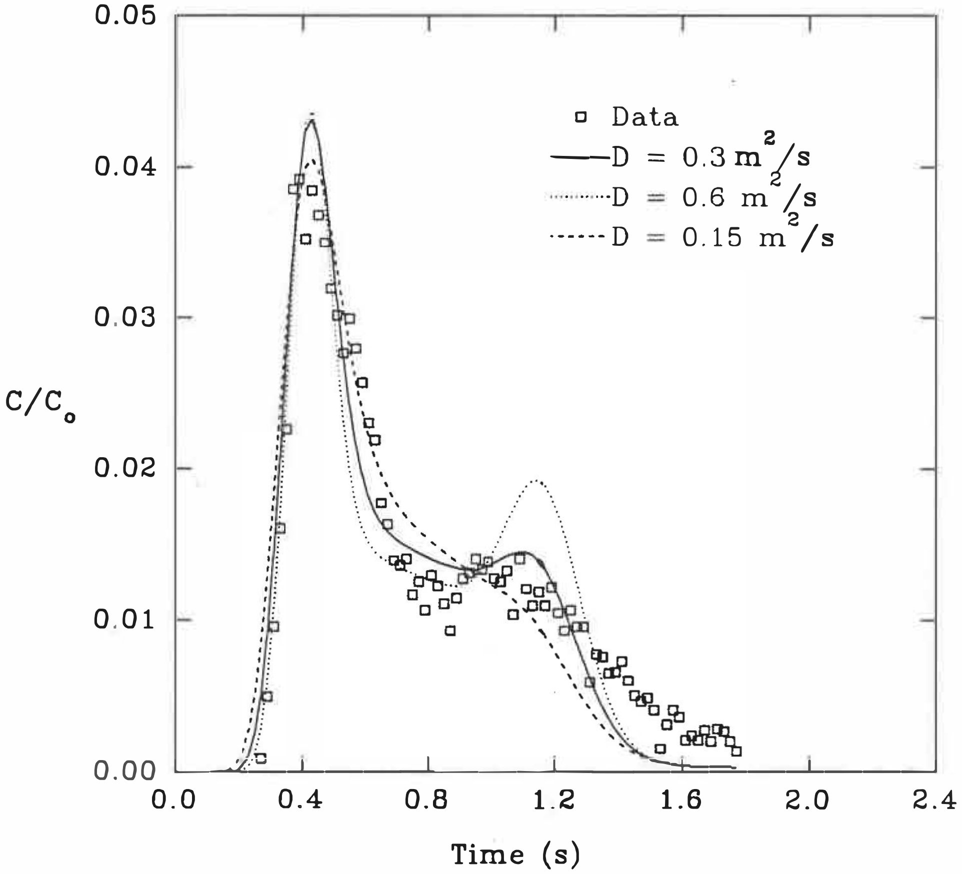

Figure A.1: Model predictions for different values of the dispersion coefficient

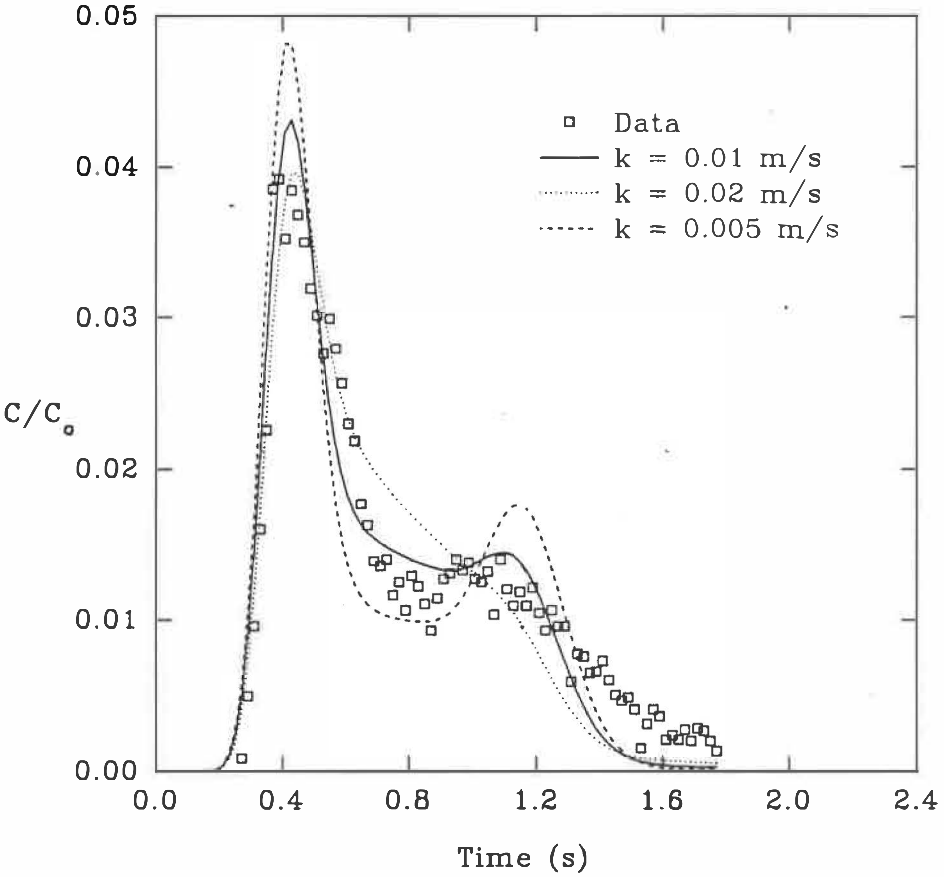

Figure A.2: Model predictions for different values of the cross–flow coefficient

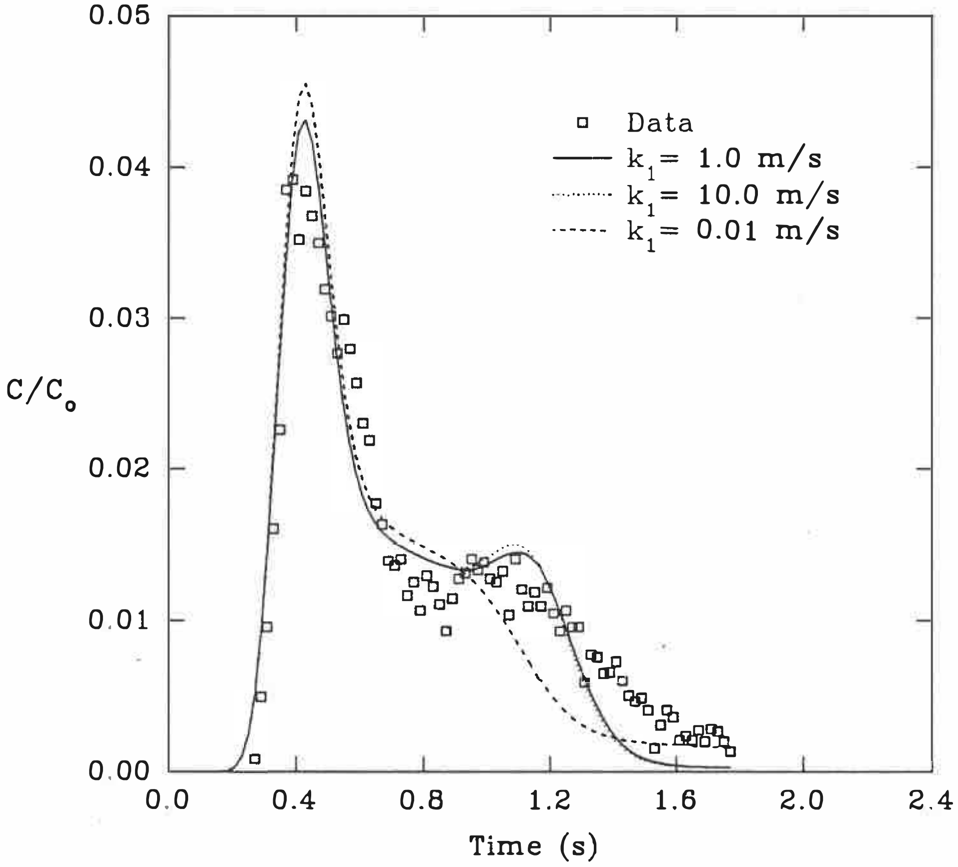

Figure A.3: Model predictions for different values of the break–up coefficient as a break-up coefficient. k_1=0.01 corresponds to the value used over the entire column length. These low transfer rates between the zones results in a long tail, as illustrated in Figure A.4. Values of k_1 greater than 1 m/s give essentially the same result.

IV φ

The slip velocity in the core is assumed equal to the particle terminal velocity. Hence, the larger the core radius the lower the gas and solids core velocity. In Fire A.4, the predictions of three different values of φ are compared. Large values of φ result in large core radii and low solids velocity. Hence, the peaks are shorter and spread out. The value of φ used in all particle RTD simulations were obtained from the gas phase studies.

V Initial core fraction of tracer:

The heights of the two predicted peaks in the RTD curve vary considerably with the assumed fraction of solids entering the core region upon injection, as shown in Figure A.5. The greater the fraction entering the core at injection the shorter the second peak will be. Few tracer particles enter the core region immediately when the tracer is injected at the base of the column (less than 4%). At low solids circulation rates as much as 40% of the solids entered the core upon injection.

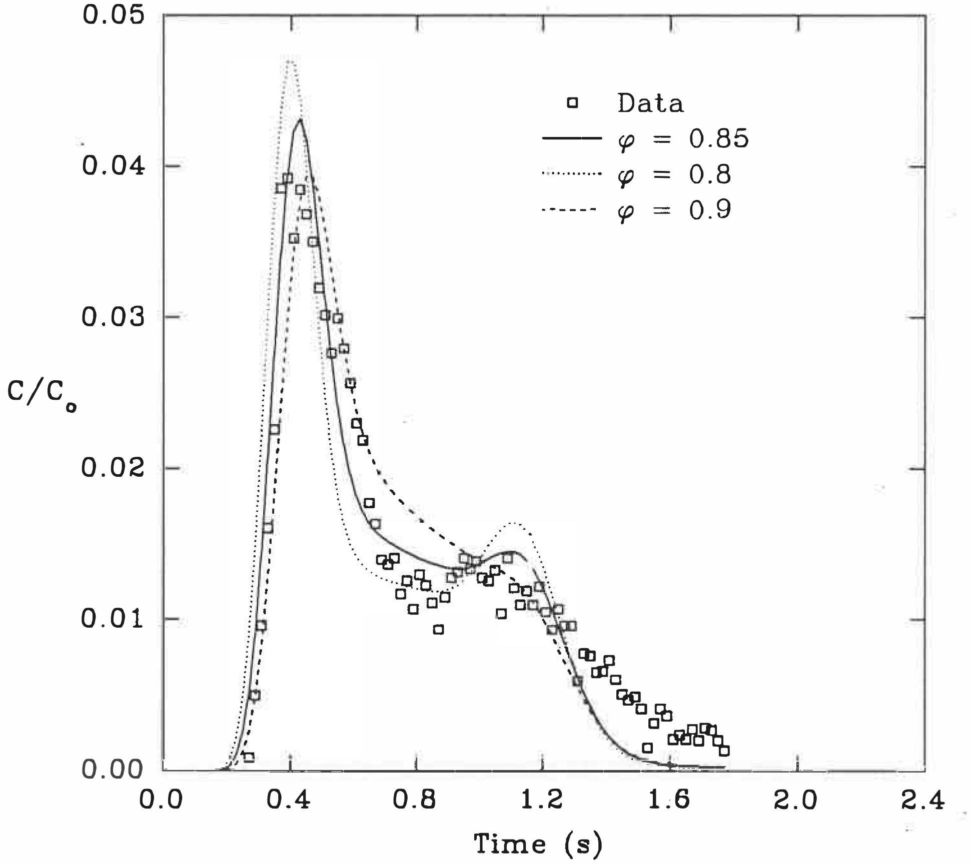

Figure A.4: Model predictions for different values of φ

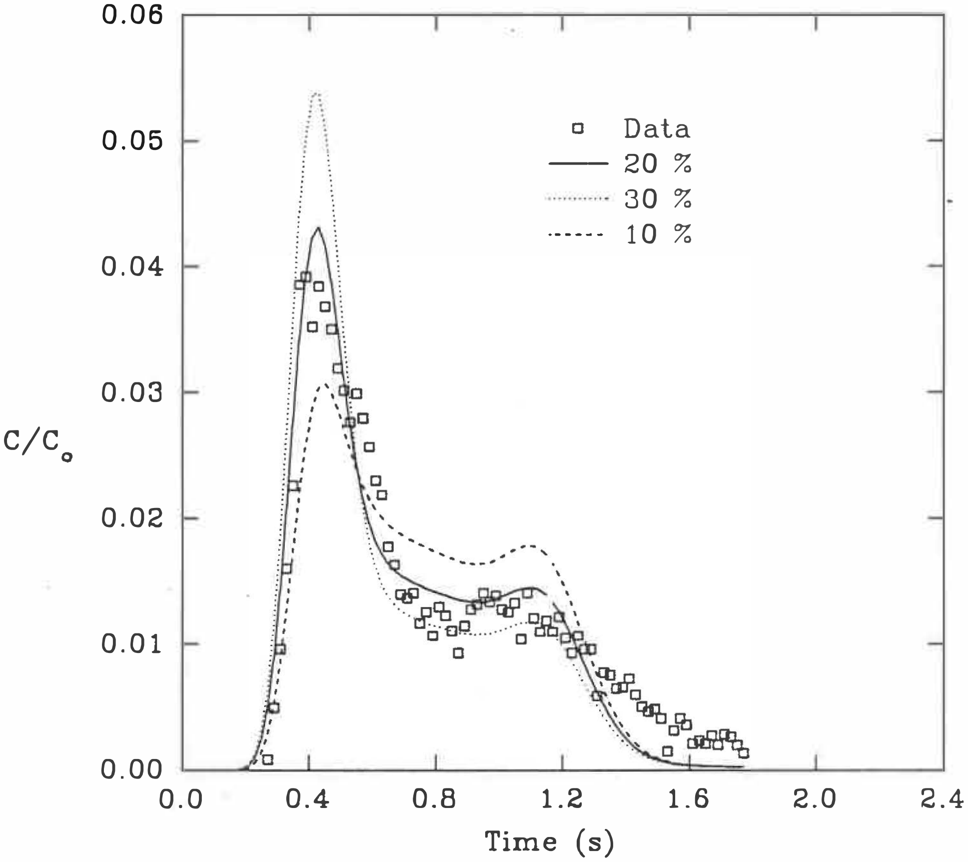

Figure A.5: Model predictions for different initial fractions of tracer in the core

VI Number of grid blocks, N_z

In Figure A.6 the effect of reducing the number of grid blocks from 400 to 200 is demonstrated. The reduction exaggerates the height of the second peak, whereas the first peak is larger. The limitation in the number of grid blocks used was cost. More is better.

VII Number of time steps, N_t

The effect of using 500 time steps instead of 1000 is illustrated in Figure A.6. Fewer time steps exaggerates both peak heights and gives a narrower peak.

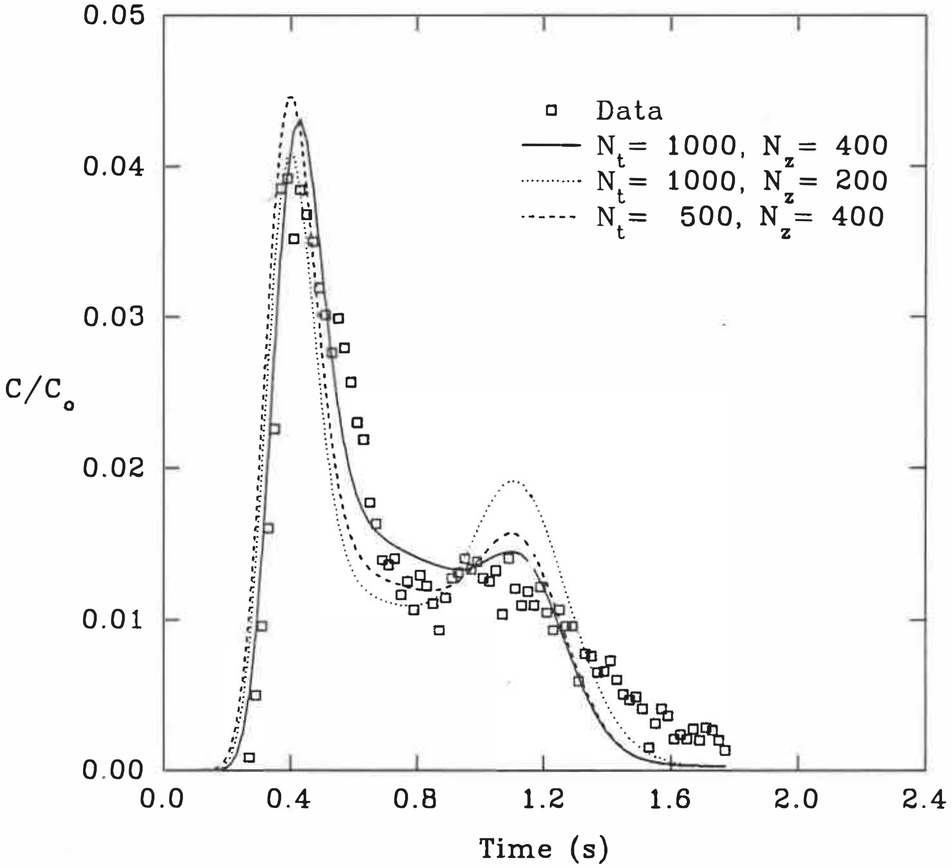

Figure A.6: Model predictions: variation with the number of time steps, N_t and grid blocks, N_z